國 立 交 通 大 學

電信工程研究所

博 士 論 文

波束掃瞄天線及平面反射天線創新研究

New Beam-steering Antennas and Planar Reflector Antennas

研 究 生：譚怡陽

指導教授：鍾世忠

中 華 民 國 九十七 年 三 月

國 立 交 通 大 學

電信工程研究所

博 士 論 文

波束掃瞄天線及平面反射天線創新研究

New Beam-steering Antennas and Planar Reflector Antennas

研 究 生：譚怡陽

指導教授：鍾世忠

中 華 民 國 九十七 年 三 月

波束掃瞄天線及平面反射天線創新研究

New Beam-steering Antennas and Planar Reflector Antennas

研 究 生：譚怡陽　　Student：I-Young Tarn

指導教授：鍾世忠博士　　Advisor：Dr. Shyh-Jong Chung

國 立 交 通 大 學

電信工程研究所

博 士 論 文

A Dissertation
Submitted to the College of Electrical Engineering and
Computer Science, National Chiao Tung University
in Conformation with the Requirements for the Degree of
Doctor of Philosophy

Accepted by the Department of Communication Engineering
March 2008
Hsinchu, Taiwan, Republic of China

中 華 民 國 九十七 年 三 月

中文摘要

本論文以新的天線波束掃瞄技術和平面式反射天線為主軸，深入探討五個題目。首先是一個具波束掃描功能之波導饋入微帶天線陣列，藉由小幅度改變波導管厚度造成傳播常數變化，控制饋送到每個天線元之間的相位差，因而使得天線陣列的波束方向偏轉。

第二個是雷達和通訊雙模的平面摺疊式反射陣列天線，由於次反射面的作用，此天線操作在雷達模態時電磁波會經由主反射面聚焦，產生可切換方向的窄波束，而通訊模態則呈現寬波束的輻射場型，兩種模態的場型各有其適合的應用。

此外，本文也對毫米波圓極化選擇性表面加以研究，在用印刷電路技術實現第一種形式的圓極化選擇性表面後，發現連通電路板兩面的垂直方向金屬孔在製作時會衍生一些非預期效應，進而影響到圓極化選擇的特性，因此發展出另一種設完全沒有垂直方向導體的三層純平面式圓極化選擇性表面，第二種設計以電磁耦合取代導體直接相連，可省去製作大量金屬連通孔的困擾，更適用於印刷電路的製程。

最後，研究出使用最少數量微波開關元件即可控制大範圍頻率選擇性表面的方法，並與角反射天線的概念結合，完成一個創新的輻射場型分集天線，此天線在不同的開關狀態組合情況下各有相對應的波束方向和輻射場型。

本論文中所有的研究，都是先建構好工作原理，然後經由計算和模擬找出最佳化設計，成品的實際量測數據和模擬結果皆相當吻合。各項成果已達預期效果，未來可以繼續個別的研究增強性能，更可進一步相互搭配結合，創造出更多樣的功能及應用。

Abstract

This dissertation deals with novel beam steering techniques and planar reflector antennas. A beam-steering waveguide-fed microstrip antenna array, a dual-mode millimeter-wave folded microstrip reflectarray antenna, a millimeter-wave right-hand circular polarization selective surface, a millimeter-wave three-layered left-hand circular polarization selective surface without any vertical conductive segment and a pattern diversity reflector antenna with minimum number of switching devices have been investigated, designed, built and tested. The theoretical approaches and practical developments of the above five researches are comprehensively discussed. All the simulated results are verified experimentally, and exhibit good consistency with the measured data. The individual subjects are worth further efforts for improvements in the future. Moreover, it is advisable to deploying new applications by combining some of the researches presented in this dissertation.

致謝

原本一直以為我的學生生涯已經結束，從沒想到過八年前竟然還能得到機會，進入博士班研讀，為此，我滿懷珍惜與自勉，迎向這個挑戰和磨練。而今終於邁向尾聲，整個過程，遠比我想像中的漫長許多許多。上課、考試、資格考、想題目、設計、製作、量測、投稿、一再修稿……每每以為克服這關，下關就容易了，現在知道其實不然，沒有一件事可以輕鬆得了的。就在即將完成畢業論文的此刻，卻忽然發現連誌謝也不好寫，想了很久，才慢慢理出一點思緒。

在博士班求學的過程中，首先感激我的指導老師鍾世忠教授，能夠容忍我這麼個不專業的學生。由於在職的緣故，我沒有像實驗室其他人一樣和老師有頻繁的互動，大多是等達成一定程度的進展後才敢找老師報告，而老師總能和顏悅色地瞭解後，很快掌握住核心，然後提出可能的問題，建議繼續進行的方向，每次討論結束後都夠我又忙好一陣子。老師的指導除了讓我做論文時獲益良多，條理清晰的思考方式和研究精神才更值得效法。

剛入學時，幾乎每天掛念著課業和資格考，日子過得很緊張，幸有同為在職的博士班同學饒瑞榮能夠一起討論，給了我許多幫助。實驗室歷屆的學弟學妹們，尤其是尤寶樺、梅家豪、李彥璋、陳星銘、林融聖、邱建評、羅文信、柯智祥、王侑信、凌菁偉、何丹雄、饒佩宗、林靖凱等幾位，在我做論文時也給我很大的影響。有時在實驗室留到很晚，不管是探討研究相關的議題或單純只是閒聊，離開時即使已經相當疲憊，心情卻充實又愉悅，偶爾甚至有點振奮的感覺，這種在職場上難有的體會，格外令人回味。祝福大家各自擁有錦繡前程，更期待將來有機會可以彼此相互拉拔扶持。

是學習、更像是磨練，追求知識長進雖有些許成績，然而這次的進修同時也讓劣根性逐一顯露，變得越來越不懂寬容和體諒，忘了樂觀，忘了應有的關懷，更忘了什麼叫珍惜。我的摯友，讓我有了希望和夢想，不斷鼓舞著我，在我低落

時總會使我再度產生勇氣，給我心靈最穩定的力量。我的家人，默默地支持我，任何時候都會做我最溫暖而堅強的後盾。感到挫折或不滿時，每念及此，就會覺得自己何其有幸，不該有太多的埋怨。但願我能記取教訓，有所領悟，今後能常提醒自己鍛鍊得更加勇敢、沉穩、智慧、和為人著想。雅彩、雅梅、伯父、伯母，想了很久還是發現，無論怎樣都難以完整表達我的感激，但所有一切我將永遠銘記在心。Data 和 Teng，謝謝你們不時的關心，而且為了幫我修論文竟然連幾天熬夜，實在過意不去。宜珮，謝謝你的付出和擔待，以及你們一家人對我的包含和照顧。爸、媽，別再偷偷為我操煩了。眾人的高情厚誼，是最豐盛又無可取代的寶藏，我也期許自己在各方面繼續努力，有一天讓大家感到欣慰和榮耀。

Contents

List of Figures and Tables

1 Introduction

Generally, a microstrip reflectarray antenna consists of a flat array of patches or dipoles printed on a thin dielectric substrate. It works in a similar concept to a conventional reflector antenna, but without the bulky configuration and mechanical complexity. As compared to a phased array, the fields from the feed antenna are spatially fed to the individual elements on the array, and thus without suffering from high propagation losses in the intricate feeding network. Therefore, the reflectarray antenna combines the advantages of the reflector antenna and the phased array antenna.

For a folded reflectarray, the required depth is only half of that of a reflectarray antenna. This further reduces the antenna volume. In addition, unlike the conventional dual-reflectors antennas, the folded reflectarray antennas are free from the blocking effect of the sub-reflectors. The radiation beam can be steered by mechanically tilting the main reflector, or shifting the position of the feed antenna. By virtue of compactness, low loss, high gain, superior design flexibility, and the ease of manufacture, folded reflectarrays could be extensively used in wireless LAN, fixed wireless access, local to multi-points distribution service, satellite communications, short-haul personal communication networks, radar applications, and wireless intelligent transport systems.

In this dissertation, we proposed a new folded microstrip reflectarray antenna which can simultaneous operated in two modes. In the radar mode, the antenna demonstrates high gain and narrow beamwidth characteristics. The beam steering is performed by electrically switching the feed antennas. In the communication mode, the beamwidth is much broader and thus provides communications over a wide

angular range.

Currently, most folded reflectarrays are dedicated to linear polarization applications. With the emergency of excellent circular polarization selective surfaces, which can pass one sense of circularly polarized waves while reflecting the other, folded reflectarray could be extended to circular polarization applications. Therefore, we proposed a milli-meter wave circular polarization selective surface. It was realized by using printed circuit technology. Metal traces were created on both sides of a laminate, and connected by vertical conductive vias. This design performs well, yet implementing numerous, dense and thin vias accurately and stably is still hard to achieve at high frequencies.

To avoid the problems associated with the vertical conductive segments and increase flexibility in design motivated the drive to invent a new type of circular polarization selective surfaces that is composed of only transverse elements but no vias. The second circular polarization selective surface is a thoroughly stratified configuration with transverse planar elements implemented on different layers, and thus is well suited for multi-layered printed circuit board manufacturing process. This design has revolutionized the way in which the function of discriminating different circularly polarized waves is established. Connections between the elements on the top and bottom layers, which are built through the couplings caused by the intermediate part in the middle layer, make the blocking effect for different circularly polarized illuminations diverse.

Planar reflectors could be applied to radiation pattern diversity antennas as well. We designed and developed novel switchable frequency selective surfaces and used them to construct a corner reflector antenna. By configuring the states of the frequency selective surfaces, various beam patterns can be formed and steered in the

azimuth plane.

In addition, another beam steering antenna is presented in this dissertation. It is a waveguide-fed antenna, composed of series-fed microstrip patch arrays that are distributed along a straight line with fixed separations. The phase difference between two adjacent sub-arrays varies with the propagation constant, which can be controlled by changing the width of the feeding waveguide, and thus leads to a steerable beam.

In this dissertation, chapter 2 is concerned with a 38 GHz waveguide-fed microstrip antenna array using a novel beam-steering technique. Chapter 3 is devoted to a dual-mode folded microstrip reflectarray antenna. Chapter 4 deals with a 60 GHz right-hand circular polarization selective surface. The study of a 30 GHz left-hand circular-polarization selective surface, which is a three layered structure without vertical conductive segments, is followed by chapter 5. A novel pattern diversity reflector antenna that requires a minimum number of switching devices is described in chapter 6.

2 A Beam-Steering Waveguide-Fed Microstrip Antenna Array

2.1 Introduction

Beam steering techniques have attracted much attention in recent years. They have many applications in wireless communications, for example, automobile collision avoidance system, smart antennas, radar systems, satellite communications, surveillance systems, etc. Many beam steering techniques have been developed without the use of conventional ferrite or solid-state phase shifters, including a movable grating film fed by dielectric image line, a microstrip antenna array fed by a dielectric image line [1]-[2] controlled by a reflector plate, and a multi-microstrip line fed Vivaldi antenna array controlled by piezoelectric transducers. In this chapter, a novel beam steering technique using microstrip patch antenna arrays fed by a rectangular waveguide is presented. As shown in Figure 2.1, 15 microstrip antenna sub-arrays are put on top of the waveguide. The incident power in the waveguide is coupled to each sub-array by an aperture on the waveguide's top wall. When the width of the waveguide is changed, the propagation constant is also varied. Thus, for fixed aperture spacing, the phase difference between two adjacent sub-arrays is changed, leading to a steerable antenna beam.

2.2 Theory

The spacing (d) between two adjacent apertures is fixed and designed to be one guided wavelength λ_g for a waveguide with width a. The propagation constant β of the waveguide is:

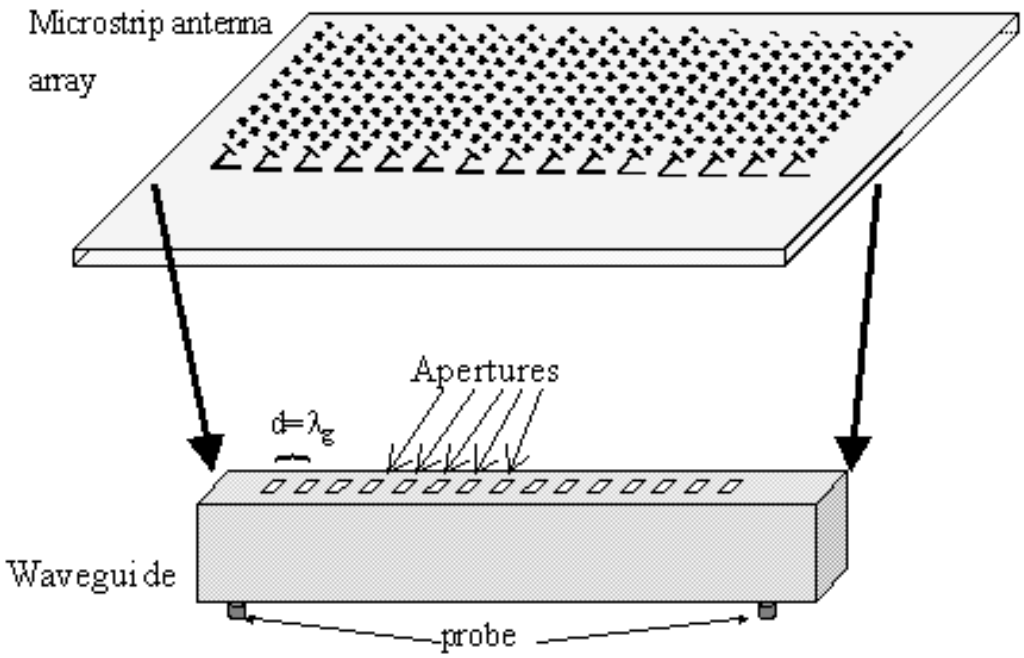

Figure 2.1 Schematic diagram of a waveguide-fed microstrip antenna array.

$$\beta = \sqrt{\omega^2 \mu_0 \varepsilon_0 - (\frac{\pi}{a})^2} \tag{2.1}$$

The derivative of the propagation constant with respect to *a* gives:

$$\frac{\partial \beta}{\partial a} = \frac{\pi^2}{a^3} \frac{1}{\sqrt{\omega^2 \mu_0 \varepsilon_0 - (\frac{\pi}{a})^2}} \tag{2.2}$$

If there is a variation Δa in waveguide width, the propagation constant will change an amount $\Delta \beta$, and the phase shift between apertures becomes:

$$\Delta \phi = \Delta \beta \cdot d = \frac{\partial \beta}{\partial a} \cdot \Delta a \cdot d = (\frac{\partial \beta}{\partial a} \cdot \lambda_g) \Delta a \tag{2.3}$$

It is seen that the phase shift can be controlled by varying the waveguide width. This phase shift, in turn, would change the direction of the array's radiation beam.

2.3 Design

Figure 2.2 shows the top view of the finished antenna array. The microstrip antennas were fabricated on a Duroid 5880 substrate, whose ε_r =2.2 and height=0.508 *mm*. Fifteen sub-arrays were formed in the array. The array was put on a WR-28 waveguide of sizes 7.11×3.56 mm^2 with apertures on the top wall. The power in the waveguide is first coupled, through an aperture, to an open-ended microstrip line, and then fed to one antenna sub-array. The excitation power of each sub-array is controlled by varying the dimension of the coupling aperture and the length of open microstrip stub [1]-[4]. Two transitions from coaxial line to waveguide were designed and placed at the input and output of the waveguide [5]. The antenna sub-array was designed and simulated by the commercial method-of-moment simulator IE3D, and the coupling from waveguide to microstrip line was designed by using the commercial full-wave finite-element software HFSS. The designs are described in the following sections.

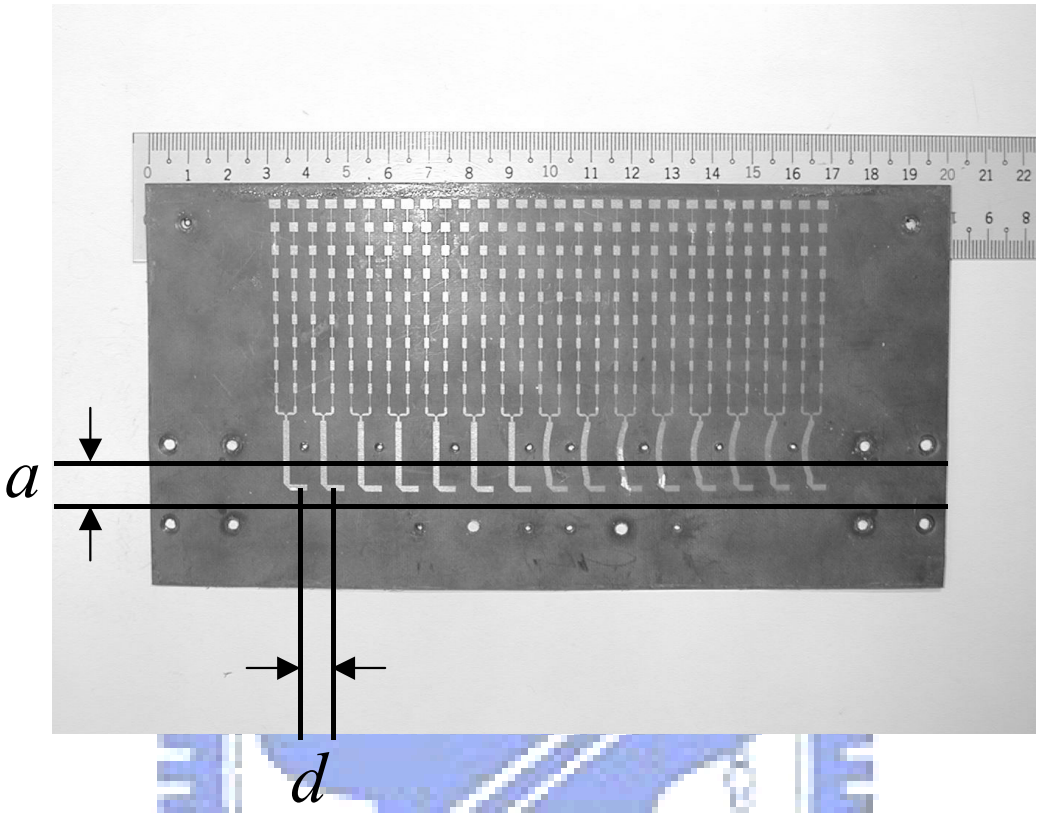

Figure 2.2 Photograph of the microstrip antenna array.

2.3.1 Series-Fed Microstrip Antenna Sub-Array

Figure 2.3 shows the photo of one antenna sub-array, which contains a power divider and two series-fed microstrip antenna arrays. Each series-fed array is composed of 9 microstrip antennas with different widths. An array with series feed is easy to construct and requires little feed network hardware [6]. The power is attenuated as the wave travels down the transmission line because of the radiation from the elements. The loss must be accounted for when determining the element excitations. For a broadside array, all elements should be in phase. Therefore, the length s of the interconnecting microstrip lines should be around half wavelength.

The equivalent circuit of a series fed microstrip array is shown in Figure 2.4, where y_i (= g_i) is the conductance of the ith element at resonance, P_{ri} is the radiation power of the ith element, P_i is the power delivered to the load from the left side of the ith element, and P_i^+ is the output power from the right side of the ith element.

Let α be the attenuation constant of the interconnecting line. The attenuation factor q can thus be expressed as $q = e^{-\alpha s}$. The powers have the following relationships:

$$
\begin{aligned}
&P_1^+ = P_1 - P_{r1} \\
&P_2^+ = qP_1^+ - P_{r2} = q(P_1 - P_{r1} - P_{r2}q^{-1}) \\
&P_3^+ = qP_2^+ - P_{r2} = q^2(P_1 - P_{r1} - P_{r2}q^{-1} - P_{r3}q^{-2}) \\
&\cdots\cdots \\
&P_N^+ = q^{N-1}(P_1 - \sum_{j=1}^{N} P_{rj}q^{-j+1})
\end{aligned}
\tag{2.4}
$$

The antenna efficiency η and conductance g_i can be calculated as:

$$
\eta = \frac{P_r}{P_1} = \frac{\sum_{i=1}^{N} P_{ri}}{P_1} \tag{2.5}
$$

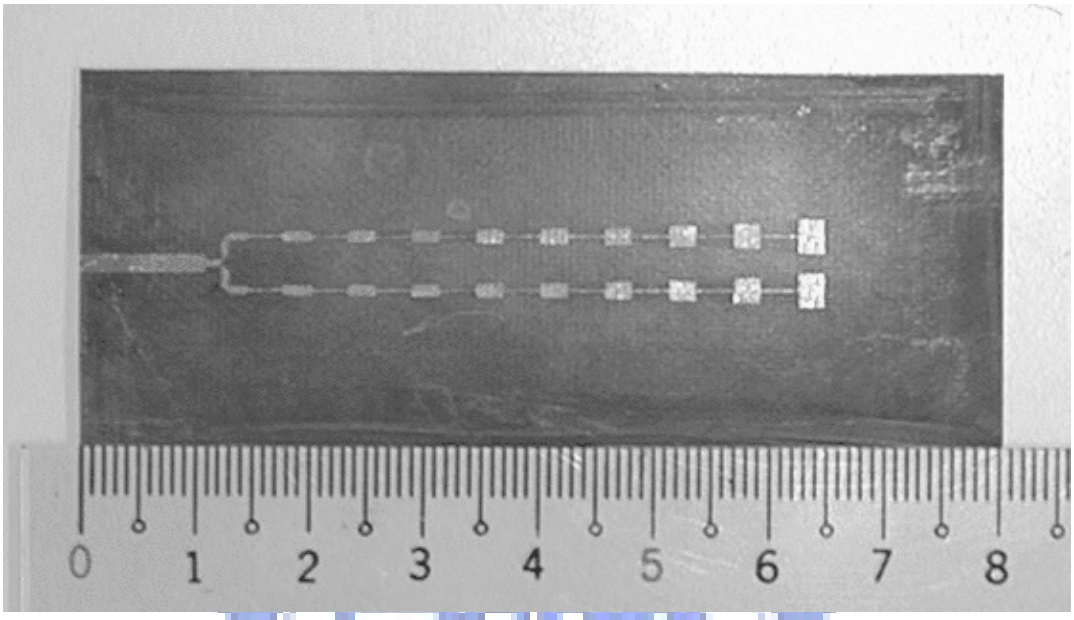

Figure 2.3 The photograph of the finished series-fed sub-array.

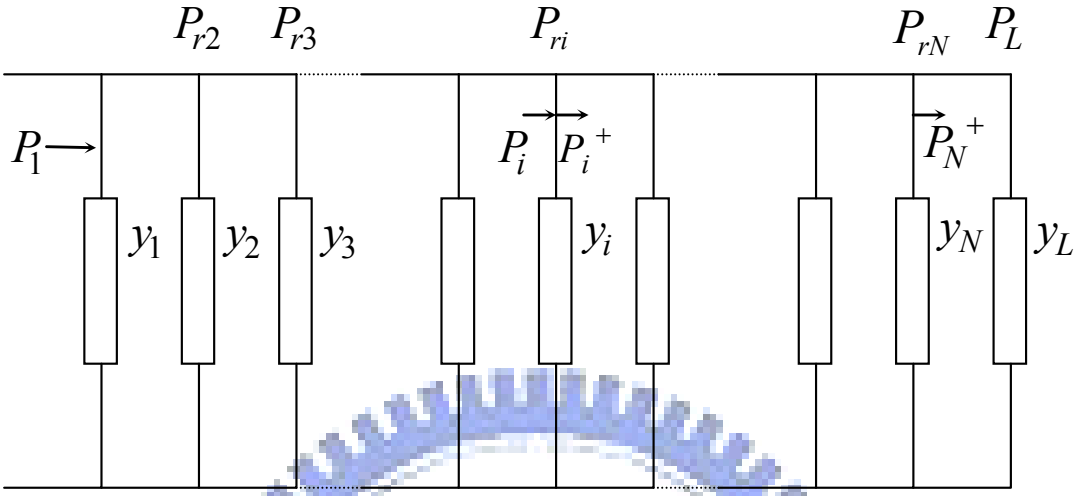

Figure 2.4 The equivalent circuit of a series fed microstrip array.

$$g_i = \frac{P_{ri} q^{-i+1}}{\frac{1}{\eta}\sum_{i=1}^{N} P_{ri} - \sum_{j=1}^{i} P_{rj} q^{-j+1}} = \frac{V^2 q^{-i+1}}{\frac{1}{\eta}\sum_{i=1}^{N} V_i^2 - \sum_{j=1}^{i} V_j^2 q^{-j+1}} \tag{2.6}$$

where V_i is the radiation intensity, which can be adjusted by varying the width of the patch.

2.3.2 Coupling from Rectangular Waveguide to Microstrip Line

The purpose of designing the coupling structure is to couple the desired amount of energy from the rectangular waveguide to the microstrip line. The operating frequency is 38.5 GHz. The width of the microstrip line and the width (W) of the aperture are fixed at 1.56 *mm* and 0.6 *mm* respectively. At resonance, the level of coupling is maximum if the length of the open stub is $\lambda_m/4$ (where $\lambda_m = C_0 \cdot f_0^{-1} \cdot \varepsilon_{reff}^{-1/2}$). Figure 2.5 shows the variations of the measured and calculated coupling coefficient for various lengths of the open stubs. The open-stub length was selected to be 3 *mm*. Although not shown here, the influence of the aperture length (L) on the coupling coefficient was also investigated. The results showed that the coupling increases with the increase of the aperture length. When the length reaches the range of 2.5 *mm* to 2.7 *mm*, the coupling reaches a maximum of –8.78 dB. Further increase of the length would cause a slight decrease of the coupling. Therefore, the length of the waveguide aperture was selected to be 2.5 *mm*.

2.3.3 Waveguide-fed Antenna Array

The coupling coefficients required for sub-arrays can be calculated with the same equations that used in series-fed antenna array design. It is noticed that the coupling apertures also exhibit different phases due to different dimensions. The phases can be compensated by properly adjust the feed line lengths of sub-arrays.

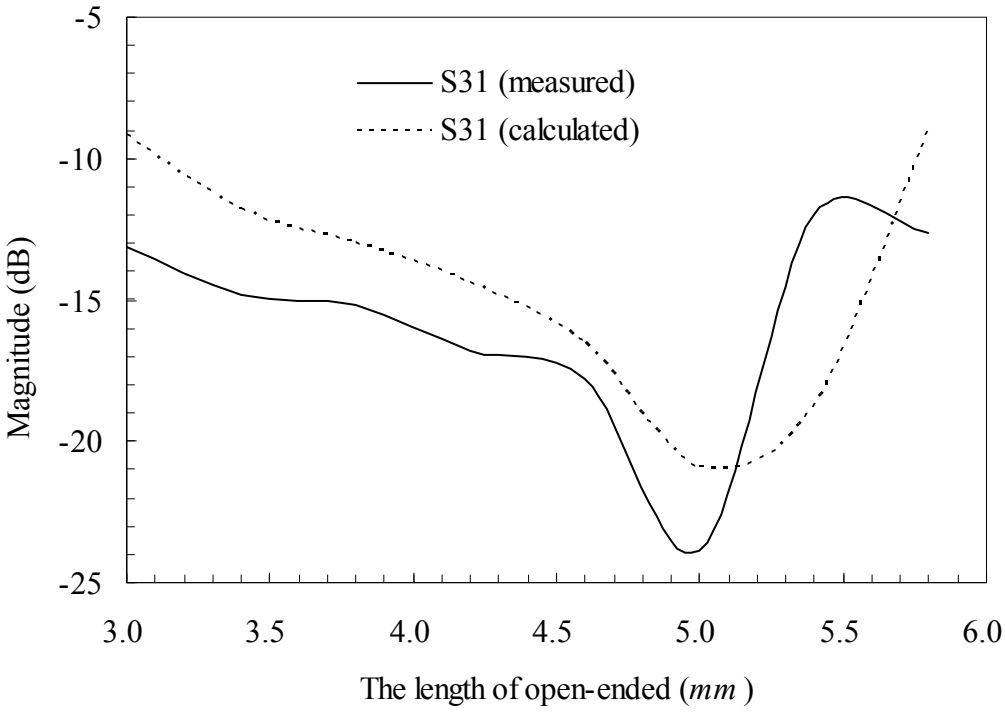

Figure 2.5 The measured and calculated coupling coefficients as functions of the length of microstrip open-end.

The power fed to each sub-array is designed to be the same (uniform power distribution). According to the measured data, the transmission loss in the waveguide is 0.115 dB/*cm*. Thus, for the waveguide section between two adjacent apertures, the attenuation factor (q) was calculated to be 0.9739. The coupling powers and phases from apertures to 50 Ω microstrip lines, simulated by HFSS, for broadside case, are listed in TABLE I. It is noted that for the scanning angle of $\pm 7^{o}$, the variation in waveguide width (Δa) is only 1 *mm*.

TABLE I The calculated coupling power and phase for each aperture in the waveguide-fed array, and the associated aperture dimensions and open stub length.

No.	Radiation Efficiency	Input Power from the Right Side of the Aperture	Aperture Dimension (*mm*)	Power Coupled to the Microstrip Line		Open Stub Length (*mm*)
				Magnitude	Phase	
1	0.57	15	W= 0.2, L= 2.5	-14.202	-51.1066	1.1
2	0.57	14.0534	W= 0.2, L= 2.5	-13.919	-51.1066	1.1
3	0.57	13.1315	W= 0.2, L= 2.5	-13.624	-51.1066	1.1
4	0.57	12.2336	W= 0.2, L= 2.5	-13.317	-47.9482	0.9625
5	0.57	11.3592	W= 0.6, L= 2.5	-12.995	-49.8695	0.825
6	0.57	10.5076	W= 0.5, L= 2.5	-12.656	-49.6251	0.825
7	0.57	9.6782	W= 0.5, L= 2.5	-12.299	-49.6251	0.825
8	0.57	8.8705	W= 0.2, L= 2.5	-11.921	-34.8314	0.55
9	0.57	8.0839	W=0.3, L=2.5	-11.517	-40.5607	0.55
10	0.57	7.3178	W= 0.2, L= 2.5	-11.085	-28.6421	0.4125
11	0.57	6.5717	W= 0.3, L= 2.5	-10.618	-32.8387	0.4125

12	0.57	5.8451	W= 0.2, L= 2.5	-10.109	-16.6067	0.275
13	0.57	5.1374	W= 0.5, L= 2.5	-9.549	-28.5607	0.275
14	0.57	4.4482	W= 0.6, L= 2.5	-8.923	-20.6199	0.1375
15	0.57	3.777	W= 0.5, L= 2.5	-8.213	-18.0592	0.1375

2.4 Measurement Results

In this study, the dimension of the waveguide is changed by attaching metal plates with different thicknesses to one side wall of the waveguide. The length of the waveguide was designed to be $l = 20\ cm$. At 38.5 GHz, the propagation constant in the waveguide is 0.6745 rad/s, and the guided wavelength $l_g = 0.9316\ mm$.

The measured gain of a single series-fed microstrip sub-array is 14.47 dBi, and the side lobe level is –9 dB. For the fabricated waveguide-fed antenna array, the measured return loss is shown in Figure 2.6. It is seen that the return loss is nearly –20 dB from 36.5 GHz to 39.5 GHz. The 10-dB bandwidth of the antenna is about 22%. The H-plane patterns with and without a metal plate inserted are shown in Figure 2.7. When there is no metal plate inside the waveguide, the gain is 21.7 dBi, the beamwidth is about 4^o, the sidelobe level is –9.67dB, and the mean beam is at 1.8^o. When a metal plate with the thickness of 0.7 mm is inserted on the sidewall of the waveguide, the gain is 17.95 dBi, the beamwidth is 4^o, the sidelobe level is –7.07dB, and the mean beam is at 7.2^o. The main beam scanning angle is 5.4^o.

2.5 Conclusions

Antennas operating at millimeter wave frequencies usually suffer considerable feed line losses. Applying waveguide-fed method will result in a much less loss.

In this study, we design a waveguide-fed microstrip antenna array, and introduce a novel beam steering technique. Slightly altering the dimension of the waveguide will lead to an evident variation of propagation constant. Consequently, this is a distinctive and advanced technique of beam steering. According to the measured data, the gain of the array is near 22 dBi, the beamwidth is about 4^{o} and the return loss is below –20 dB. The main beam scanning angle in H-plane is 5.4^{o}, which shows good consistence with the theoretical value.

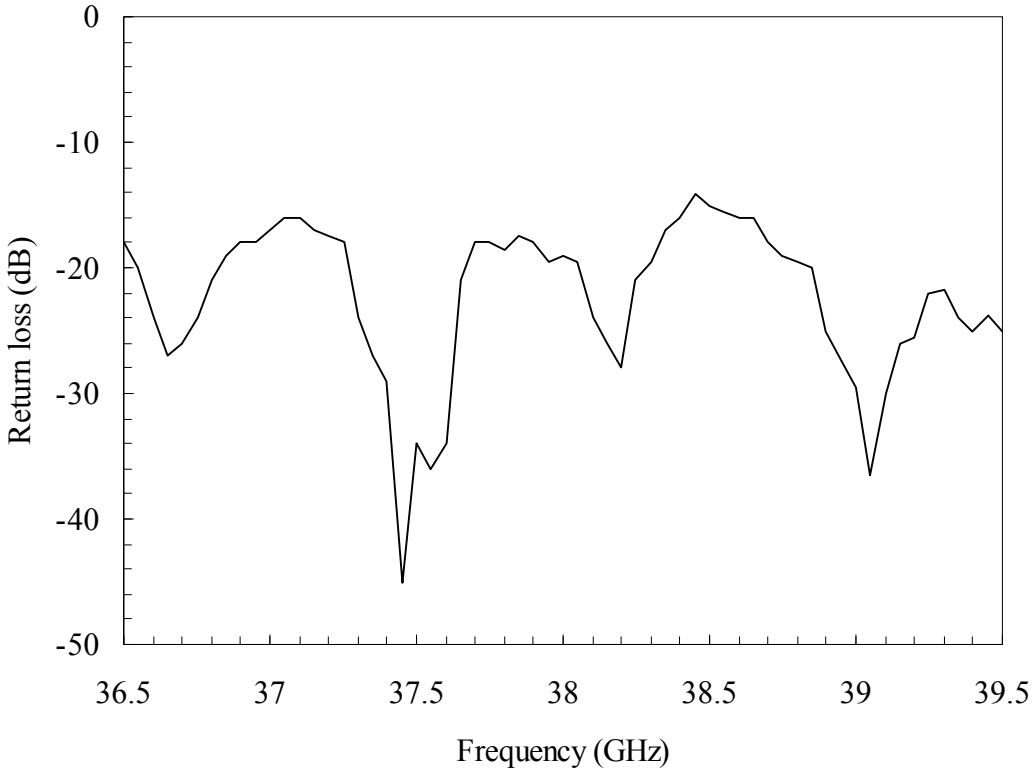

Figure 2.6 Return loss of the waveguide-fed microstrip antenna array.

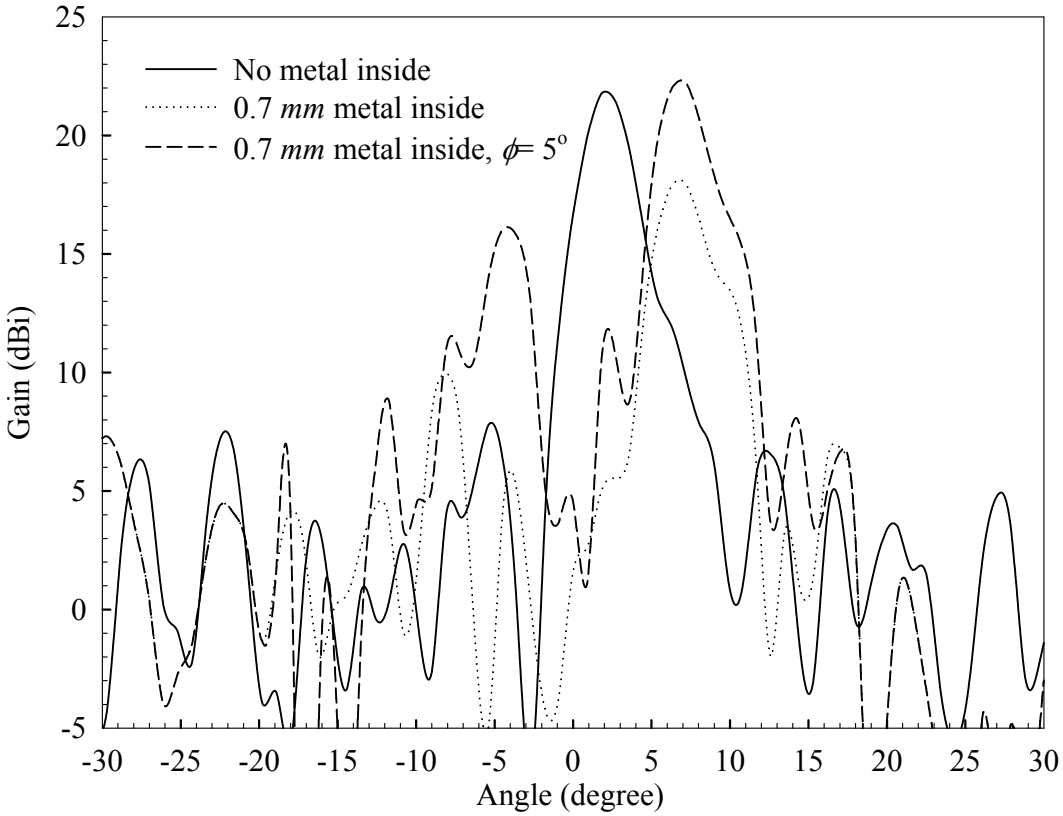

Figure 2.7 Comparison of the H-plane patterns of the waveguide-fed microstrip antenna array at 37.8 GHz.

References

1. M-Y Li, K Chang, “New tunable phase shifters using perturbed dielectric image lines,” *IEEE Trans. Micro. Theo. and Tech.*, vol. 46, no. 10, September 1988.
2. M-Y Li, K Chang, “Novel low-cost beam-steering techniques using microstrip patch antenna arrays fed by dielectric image lines,” *IEEE Trans. Antennas Propagat.*, vol. 47, iss. 3, pp. 453-457, March 1999.
3. S. R. Rengarajan, “Slot couplers for feeding branch waveguides of a planar slot array,” *IEEE AP-S Int. Symp.Digest*, vol. 2, pp. 682 - 685, June 1989.
4. A. Datta, A. M. Rajeek, A Charabarty, and B. N. Das, “S matrix of a broad wall coupler between dissimilar rectangular waveguides,” I*EEE Trans. Micro. Theo. and Tech.*, vol. 43, no. 1, January 1995.
5. J. S. Izadian, and S. M. Izadian, *Microwave transition design*, Artech House, 1988.
6. T. Galia, G. Mazzarella, and G. Montisci, “A new approach to the design of linear series-fed printed arrays,” *Proc. IEEE Int. Symp. Antennas Propagat*, vol. 4, pp. 2736-2739, 1999.

3 A Dual-Mode Millimeter-Wave Folded Microstrip Reflectarray Antenna

3.1 Introduction

The folded reflectarray antenna [1]-[10] presented in this chapter can be simultaneous operated in two modes, namely, the radar mode and the communication mode. In the radar mode, the antenna demonstrates high gain and narrow beamwidth characteristics with beam switching capability. It is suitable for radar applications, such as automotive sensors in wireless Intelligent Transport Systems (ITS). While in the communication mode, the beamwidth is much broader and thus provides communications over a wide angular range.

The radar is a key technology in ITS, which opens up new perspectives of comfort and safety features in future automobiles. The automotive radar can be used for target identification, road condition detection, vehicle collision warning and avoidance, obstacle warning, stop-and-go traffic support and cruise control. In addition, accurate radar images about the ambient traffic situation could be applied for multiple targets classification and scenario interpretation. For a forward looking vehicle radar, a coverage of about ±10 degree, deduced from the demand of operation in urban area or narrow road curvature, is acceptable. The required field of view can be achieved using a multi-beam or steerable beam high-resolution antenna. In general, a narrower beamwidth antenna is required to obtain higher resolution, and higher gains contribute considerably to the sensitivity.

Besides, there is an increasing trend in having a combined use of the inter-vehicle communications as well as the radar sensing. The inter-vehicle

communications play an essential role in an advanced ITS for it enables each vehicle to communicate with other vehicles (not only directly, but also indirectly via roadside communication units), so as to get the information that are difficult or impossible to measure by the vehicle alone. The vehicular collision avoidance capability can be enhanced by incorporating inter-vehicle communications technology through wireless ad hoc networks.

The design of each constituting part of the proposed antenna is presented in this chapter. Some formulas have been derived for analysis and design. Measurement results of the antenna pattern, antenna gain, aperture efficiency, and beam switching property show good agreement with the simulated ones

3.2 Principle

The proposed dual-mode folded reflectarray antenna is illustrated in Figure 3.1. The distance H from the main reflector to the sub-reflector is 23 *mm*. The main reflector is a reflectarray that consists of hundreds of square patch antennas distributed over a circular region with diameter D; each square patch has two open microstrip stubs for field twisting and phase compensation. The sub-reflector is composed of high-density printed metal lines, which is transparent to one polarization but would reflect the other. The feed antennas are probe-fed rectangular patch antennas located on the main reflector.

For the radar mode, the fields radiated from the feed antennas are polarized in the direction parallel to the metal grid lines on the sub-reflector. The fields confront the sub-reflector are reflected. Due to the path differences, the fields received by every square patch antenna on the main reflector have different phases and amplitudes. Each square patch has two open stubs to provide the required 90^{o} polarization twisting

and phase compensation. The fields re-radiated from the square patch array are in uniform phase and tapered amplitude distribution, with polarization perpendicular to the grid lines. Thus, the re-radiated fields could penetrate through the sub-reflector and generate a narrow radiation beam.

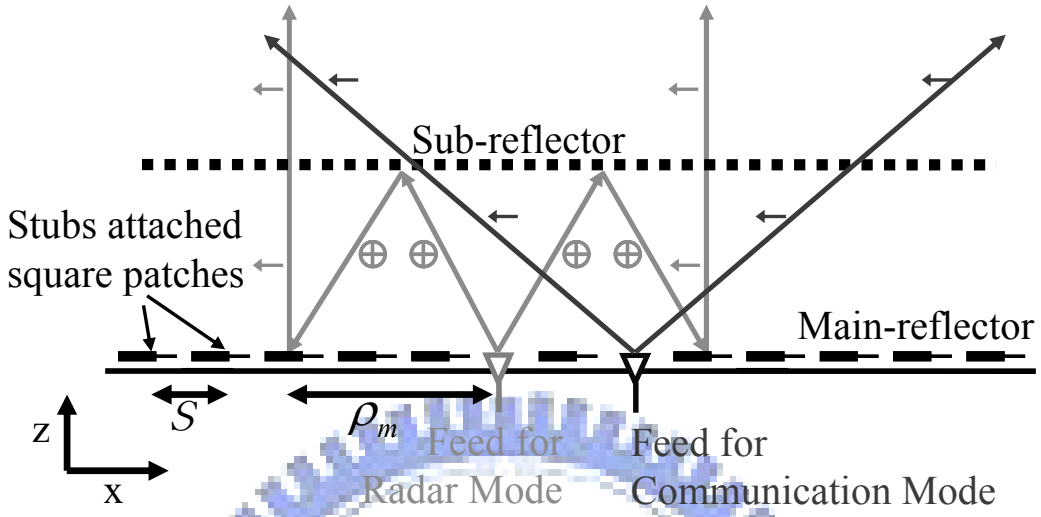

Figure 3.1 The schematic diagram of the proposed folded reflectarray antenna.

The beam direction will vary with the position of the feed. Different from the single mode horn-fed multiple-beam reflectarray antennas which have already been extensively discussed [11]-[12], three feed patches were designed and implemented in the vicinity of the center of the main reflector for radar mode beam switching in this work.

On the other hand, the feed for the communication mode is designed to have a polarization perpendicular to the grid lines on the sub-reflector. Therefore, the fields radiated from this feed will transmit through the sub-reflector directly, the gain pattern is in principle that of the feed antenna, and the position of the feed antenna is not restricted to areas in the vicinity of the center of the main reflector.

Refer to Figure 3.2. The input power fed to the feed antenna is denoted as P_i. G_f and G_{sq} are the maximum gains of the feed antenna and the square patch antenna, respectively. The antenna gains at the direction of (θ, ϕ) are thus correspondingly equal to $G_f \cdot g_f(\theta, \phi)$ and $G_{sq} \cdot g_{sq}(\theta, \phi)$, with $g_f(\theta, \phi)$ and $g_{sq}(\theta, \phi)$ being the normalized power pattern of the feed antenna and the square patch antenna respectively. It is noted that, the typical pattern $g_f(\theta, \phi)$ of the designed feed antenna and the measured G_f of realized antenna was used in the simulations.

The power P_m received by the mth square patch can be calculated from the Friis's formula and written as:

$$P_m = P_i G_f G_{sq} C_m \tag{3.1}$$

(a)

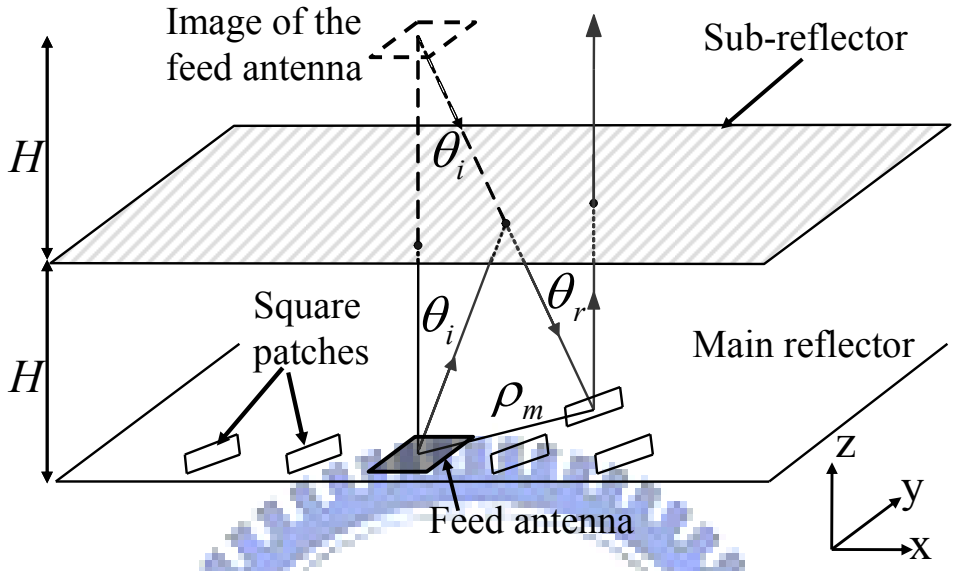

(b)

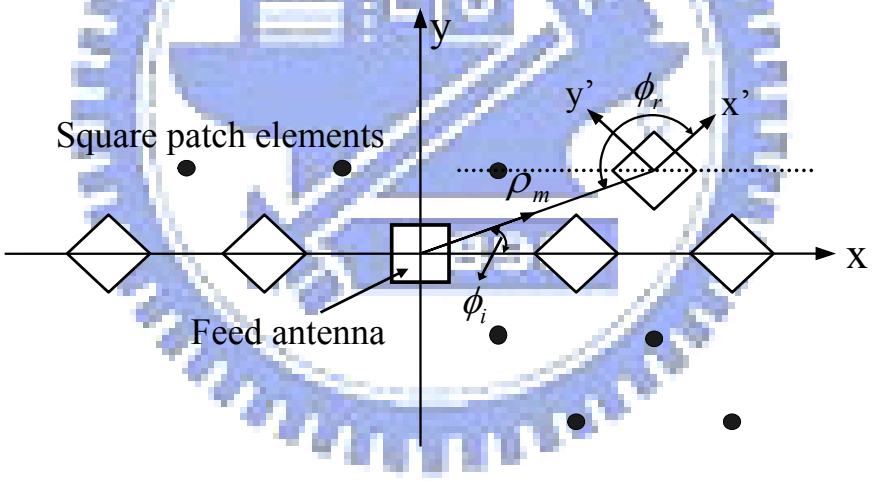

Figure 3.2 Coordinates for the analysis of the folded reflectarray antenna.

with C_m defined as:

$$C_m = \frac{g_f(\theta_i, \phi_i) \cdot g_{sq}(\theta_i, \phi_i + 3\pi/4)\lambda^2}{(4\pi r_m)^2} \tag{3.2}$$

here r_m (= $\rho_m^2+4H^2)^{1/2}$ is the path length from the mth square patch to the feed antenna, with ρ_m being the distance between the square patch and the feed antenna. For an illuminating angle of (θ_i, ϕ_i) from the feed antenna, the receiving angle for the mth square patch is (θ_i, $\phi_i+3\pi/4$).

The received power by each square patch antenna will re-radiate from the same antenna. The total radiation power P_{rad} at an angle of (θ, ϕ) from the in-phase excited array is:

$$P_{rad}(\theta, \phi) = G_{sq} g_{sq}(\theta, \phi) \cdot F^2(\theta, \phi) \tag{3.3}$$

where the array factor $F^2(\theta, \phi)$ is:

$$F^2(\theta, \phi) = \left| \sum_m \sqrt{P_m} \cdot e^{jk_0(x_m \sin\theta\cos\phi + y_m \sin\theta\sin\phi)} \right|^2 \tag{3.4}$$

with (x_m, y_m) being the global coordinates of the mth square patch antenna. Thus, the total antenna gain pattern G_{total} of the folded reflectarray antenna can be derived as:

$$G_{total}(\theta, \phi) = P_{rad} / P_i = G_f \cdot G_{sq}^2 \cdot f^2(\theta, \phi) \tag{3.5}$$

where the normalized array factor is:

$$f^2(\theta, \phi) = g_{sq}(\theta, \phi) \left| \sum_m \sqrt{C_m} \cdot e^{jk_0(x_m \sin\theta\cos\phi + y_m \sin\theta\sin\phi)} \right|^2 \tag{3.6}$$

3.3 Design

In this work, we developed a 38.5 GHz dual-mode folded reflectarray antenna. For radar mode beam switching operation, three fixed-position patch antennas were

created as the feeds for three corresponding spot beams. Whereas, there is another patch for the communication mode. The details for the design of each part are presented in the following subsections.

3.3.1 Feed Antenna

As a low profile folded reflectarray, feed antennas with wider beams are preferred in order to illuminate more square patch antennas. Besides, every feed's area on the main reflector has to be small to enable multiple closely spaced beams [13]. Horn antennas are used as the feeds in general reflectarrays. A horn with sophisticated illumination design [14] would make the reflectarray have optimal aperture efficiency, but it suffers from bulky configuration and mechanical complexity. On the contrary, printed type antennas, which can be directly made on the main reflector, are advantageous to multiple-feed or movable feed design. Also, the transceiver circuits can be easily integrated on the backside of the antenna. Hence the feeds in this work are probe-fed microstrip patch antennas.

The feed patches of the folded reflectarray, having sizes ($L \times W$) of 2.3×2.4 mm^2, were designed on a Duroid 5880 substrate with thickness h of 0.508 mm and $\varepsilon_r = 2.2$. The measured return loss of the fabricated antenna (Figure 3.11) shows a 10-dB bandwidth of 9% (from 36.5 GHz to 39.9 GHz), with a peak value of 24.8 dB. The broadside gain (G_f) is 6.3 dBi, and the measured 3-dB beamwidths in E-plane and H-plane at 38.5 GHz are 74.7° and 88.2° respectively, as shown in Figure 3.3.

Several feed antennas, for both the radar and communication modes, will be jammed into between the dense square patch antennas on the main reflector. The close adjacency of the feed antennas and their neighboring square patch antennas will cause the depolarization effect on the feed antennas. The cross-polarization is lower than the co-polarization by at least 15 dB in simulation, which is ignorable.

However, the worst isolation is only about 5 dB by measurement. Simple treatments around periphery of the designed feed would be required to prevent the couplings, in case that the radiation pattern for communication mode is worsen, as will be discussed in Section 3.4. Whereas, in the radar mode, the narrow beam patterns after focusing will scarcely affected by the variations caused by the couplings as shown in Section 3.3.3.

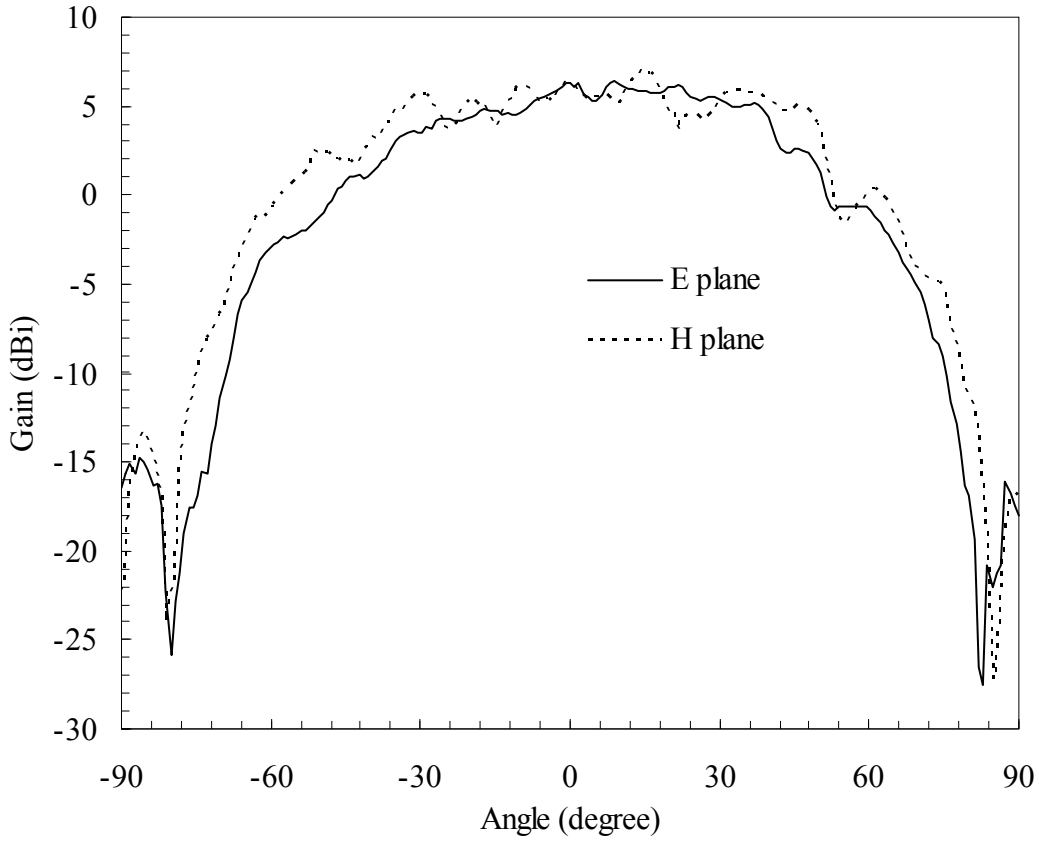

Figure 3.3 The measured radiation patterns of the feed antenna at 38.5 GHz.

3.3.2 Sub-reflector

Though in general, the substrate thickness of about $\lambda/2$ would allow the fields to go through the dielectric slab with minimum insertion losses [14]. The 31-*mil* Duroid 5870 laminate is chosen to fabricate the sub-reflector, with fine parallel metal lines printed on, because it has a low loss tangent and its relative permittivity is close to 1. The insertion loss of a high permittivity substrate is very sensitive to the thickness. On the other hand, for low permittivity material, for example Duroid 5870, $\lambda/2$ at 38.5 GHz is around 100 *mil*. It is unpractical to use such a thick laminate, despite the simulated insertion loss for this case is 0.12 dB. The simulated loss for the 31-*mil* Duroid 5870 substrate at 38.5 GHz is 0.51 dB, which is a quite good value that can be obtained with commonly available laminates.

The width and spacing of the metal lines are designed so that the insertion loss is as low (high) as possible for an incident wave with its polarization perpendicular (parallel) to the metal lines. Three sub-reflectors with different printed lines were tested. The lines' width and spacing for each sub-reflector are kept the same, and are equal to 0.1 *mm*, 0.2 *mm*, and 0.5 *mm* respectively. A horn antenna illuminated EM waves toward another horn antenna at 230 *mm* apart. These two horns were collimated and aligned with each other and were vertically polarized. The sub-reflectors were placed in the middle of the transmitting and receiving horns with metal lines oriented horizontally. The powers received by the receiving horn antenna were then compared to that without sub-reflector inserted. For the 0.1-*mm* sub-reflector, the insertion loss due to the presence of the sub-reflector is only 0.67 dB. Then the sub-reflector was rotated to make the metal lines oriented to vertical direction, the power received with the sub-reflector is 38.49 dB lower than that without the sub-reflector. It is evident that the incident wave parallel to the metal

lines is almost totally blocked and reflected by the sub-reflector.

Note that the nonzero insertion loss represents a certain portion of the incident power will be reflected. Those waves will bounce between the main reflector and the sub-reflector, experience multi-reflection and polarization twisting, and thus would impair the antenna performance.

Although not presented here, the measurement results for the 0.2-*mm* and 0.5-*mm* sub-reflectors show that the blocking effect for the parallel incident fields becomes worse when the line width and spacing increases. Thus, the 0.1-*mm* sub-reflector was adopted for use in the folded reflectarray.

3.3.3 Main Reflector

The efficiency of a reflectarray is usually not that high as compared to a conventional reflector antenna. The reduction in efficiency results from the power losses in the stubs-attached patch elements and the phase and polarization errors due to mutual coupling between non-identical elements. Besides, in a folded type antenna, there are extra losses in the path because the reflected fields by the sub-reflector are no greater than the incident fields, and thus the efficiency would be lower. Although the typical values for reflectarrays range from 10% to 30%, efficiency up to 70 % has been reported [15]. The aperture efficiency (η) is defined as:

$$\eta = \frac{G_{\max}}{(4\pi/\lambda^2)\cdot A_p} = \frac{G_{\max}}{(\pi D/\lambda)^2} \tag{3.7}$$

here A_p (= $\pi D^2/4$) is the area of the main reflector and $G_{\max}$ is the maximum antenna gain.

To get a maximum density of the array elements, the square patches are

arranged to form an equilateral triangular array with spacing S equal to 5 *mm*, or about 0.6λ, within a circular area with diameter D. In general, the aperture efficiency for a small reflectarray, even with reasonable good illumination, is not very good, but gets much better with increasing size and adapted illumination.

Figure 3.4 shows the calculated aperture efficiency of the folded reflectarray antenna as a function of D when illuminated by the same feed patch. As the antenna size increases, the efficiency first increases due to the fast growth of the antenna gain. Then, when D is further increased, the efficiency slightly decreases. This is because that the illumination power decreased as the distance and angle from the feed patch increases; the received power of the square patch antenna decays rapidly as the patch moves far away from the feed antenna, and thus the gain of the whole reflectarray becomes saturated. A maximum calculated efficiency of about 25% could be achieved as D equals 140 *mm*. However, when D becomes larger than 100 *mm*, the efficiency growth by enlarging the array size is quite limited, since the normalized received powers of the square patches located outside the circular region of radius 50 *mm* are below –8.3 dB. Therefore, D is determined to be 100 *mm* in this work.

The same substrate material as that for the feed antenna was used to fabricate the main reflector. The main reflector comprises several hundreds of square patch antennas located inside a circular area of diameter D = 100 *mm*. The square patch antennas are oblique to the feed antenna with 45°. For field twisting and focusing, two microstrip open stubs, each with a $\lambda/4$ impedance transformer, are attached to two adjacent edges of the square patch, as shown in Figure 3.5. The square patch measures 2.3×2.3 mm^2. The widths of the stubs and the transformers are, respectively, 0.17 *mm* and 0.1 *mm*. The field incident on the antenna will be received by the two stubs, reflected at the open end, and then fed back to the antenna

for re-radiation. The difference between the open stubs' lengths is designed to be $\lambda/4$. This will make the re-radiated field orthogonal to the incident field, as will be explained in the next paragraph. Besides, the absolute lengths of the stubs are determined according to the location of each square patch so as to compensate the phase delay due to path differences. Therefore, the antennas on the main reflector are excited with uniform phase and tapered amplitude distribution.

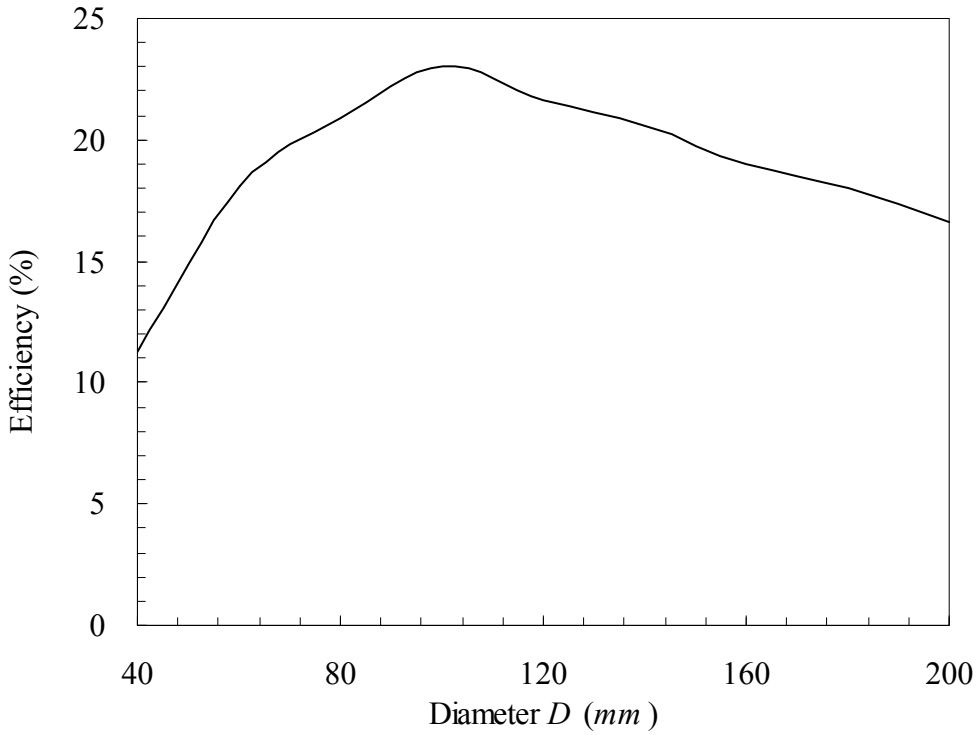

Figure 3.4 Calculated aperture efficiency, as a function of the aperture's diameter *D* of the folded reflectarray antenna.

To see the field twisting effect, let us consider a vertical field (radiated from the feed antenna) incident on the stubs-attached patch. As shown in Figure 3.5(a), the incident field can be decomposed into two orthogonal components, that is, component A and component B. These two equal-amplitude components are separately received by the two orthogonal open stubs on the left and right sides. After reflected at the stubs' open ends, these components are fed back to the antenna. Since the left stub is longer than the right stub by $\lambda/4$, component A experiences 180° more phase delay than component B in the round-trip tour. The resultant total re-radiation field is thus twisted to the horizontal direction, as shown Figure 3.5(b).

For better estimation of the folded reflectarray's performance, scattering parameters of the individual square patch antenna was measured by extending the two open stubs as two ports. Around the design frequency of 38.5 GHz, the return loss (S_{11}) and isolation between ports (S_{21}) are less than –20 dB. Also, the co-polarization and cross-polarization patterns were taken with one port terminated. The broadside gain and the 3-dB beamwidth of the co-polarization component are 5.6 dBi and 88° respectively. By putting the measured patterns of the individual square patch into (5), a co-polarization gain of about 26 dBi and a maximum cross-polarization gain (assumed the cross-polarization fields of the square patches were in-phase) of –4.8 dBi of the folded reflectarray were obtained.

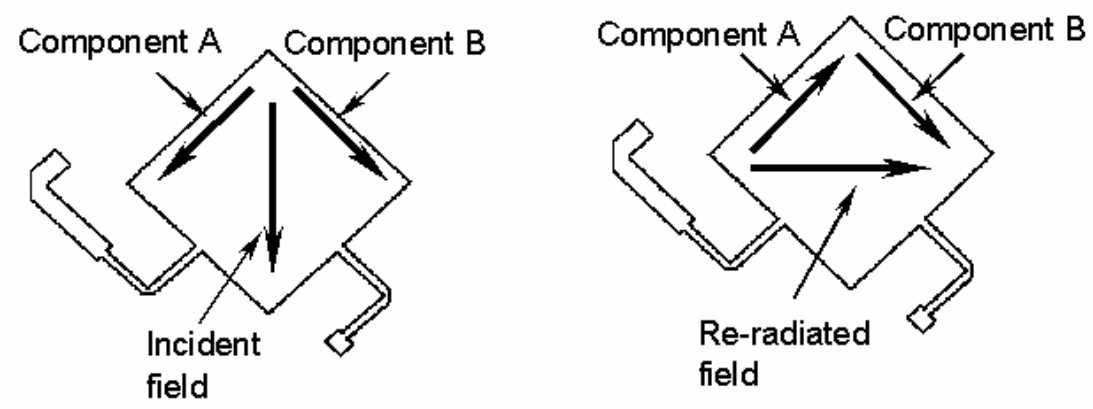

Figure 3.5 The field twisting effect of the 45° tilted square patch antenna with two open stubs.

Furthermore, derived from the full wave simulation result of the single square patch with appropriate periodic boundary conditions applied, the maximum cross-polarization of the folded reflectarray grows up from –4.8 dBi to about –1.5 dBi. It is the mutual coupling effect by the close proximity of the square patches and the stubs. Actually, the cross-polarization component of the array is at least 27.5 (=26–(–1.5)) dB lower than the co-polarization component of the array, which is very small and will be blocked by the sub-reflector.

For more efficient use of the excitation power and suppressing the pattern ripple, the feed antennas for radar mode should be placed as near the center of the array as possible. Square patch antennas overlap the feed antennas are to be detached for the accommodation of the feed antennas. Therefore, since the effective aperture reduces, the main beam gains will decrease and the side lobes will increase. Assume that there are no square patch antennas within the circular area of diameter D_f. The simulated patterns for various D_f are shown in

Figure 3.6. When $D_f = 30$ *mm*, the gain drops about 1.27 dB in comparison to $D_f = 0$ *mm*. In reality, the feeds will occupy an area substantially less than that of the $D_f = 30$ *mm* circle. The pattern will not be significantly affected.

It is also known from the simulations that the scattered fields reflected by the ground plane of the main reflector are relatively weak, in comparison to the fields re-radiated from the square patches. Moreover, the ground scatterings are haphazardly distributed; they do not lead to co-phasal behavior in any direction and thus were ignored in the design.

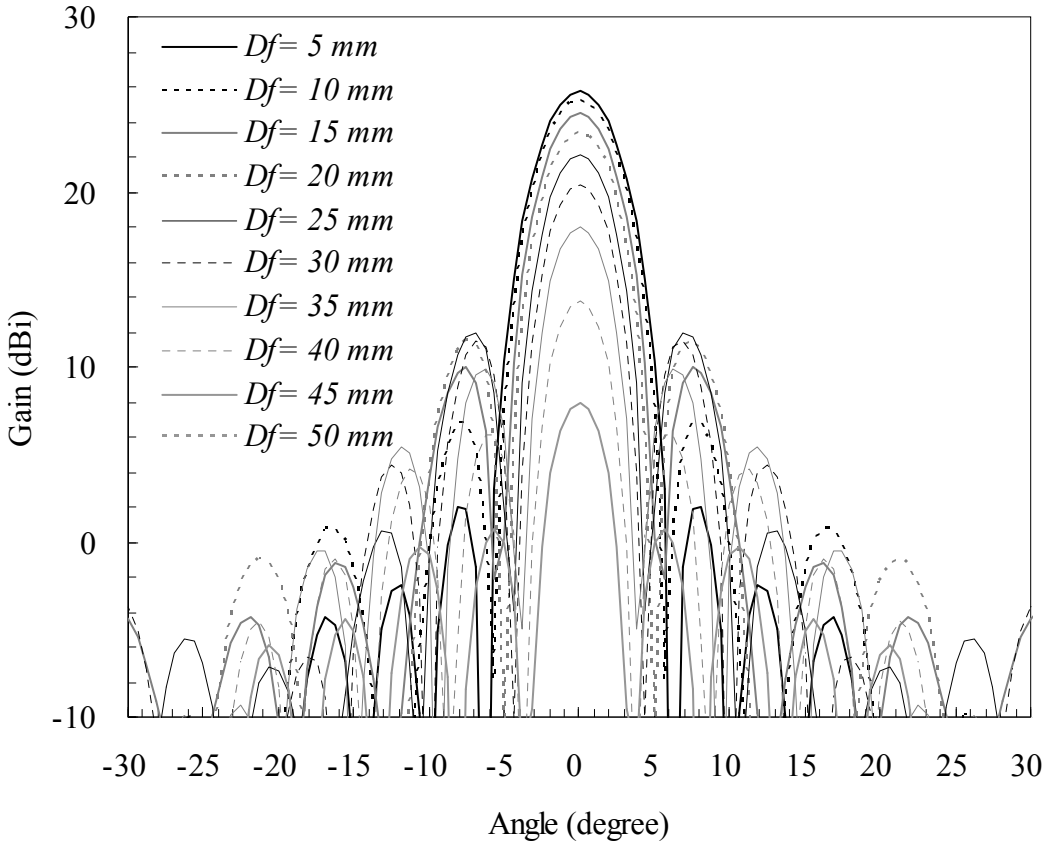

Figure 3.6 Calculated H-plane patterns of the folded reflectarray antenna for various D_f at 38.5 GHz.

3.3.4 Beam Switching Mechanism

As can be seen from Figure 3.2 that, by moving the position of the feed antenna, the path length from the image feed antenna to the *m*th square patch changes from the original value r_m to a new value r_m', and then the new normalized array factor becomes:

$$f^2(\theta,\phi) = g_{sq}(\theta,\phi)\left|\sum_m \sqrt{C_m}\cdot e^{jk_0(x_m\sin\theta\cos\phi + y_m\sin\theta\sin\phi + \Delta r_m)}\right|^2 \tag{3.8}$$

the path length variation for a small feed movement has negligible influence on the received power (P_m), but the shift $k_0\Delta r_m$ ($=k_0(r_m-r_m')$) in the phase term of the antenna gain pattern would result in a beam direction change.

Figure 3.7 shows the calculated H-plane gain patterns for various displacements *d* of the feed position. The feed antenna moves along the x direction from *d* = –15 *mm* to +15 *mm*. When *d* = 0 *mm*, the radiation beam points to the broadside direction, with the antenna gain of 25.73 dBi, 3-dB beamwidth of 4.9°, and side lobe levels of about –25 dB. It is seen that, as *d* changes from –15 *mm* to +15 *mm*, the main beam directs from +14.4° to –14.4°, the corresponding first side lobe moves from the left hand side of the main beam to the right hand side, and the side lobe level rises with the increase of the feed position displacement. The beam steering rate is about 1° per 1 *mm* movement. However, the antenna gain becomes lower as the feed moves farther away from the center position. The maximum gain variation in the range of *d* = –15 *mm* to +15 *mm* is about 1.5 dB.

A sliding track mechanism, as shown in Figure 3.8, which allows controlling the movement of the feed, was fabricated to verify the above analysis. The center region of the main reflector was dug out so that the feed antenna can be placed and moved. The total movable range is 8 *mm* (*d* = –4 *mm* to +4 *mm*). The measured H-plane

patterns of the folded reflectarray antenna for various feed positions (*d*) at 38.5 GHz are illustrated in Figure 3.9. A total steering angle of 7.2° was attained for the 8-*mm* feed position displacement. The beam steering rate is very close to the simulated one.

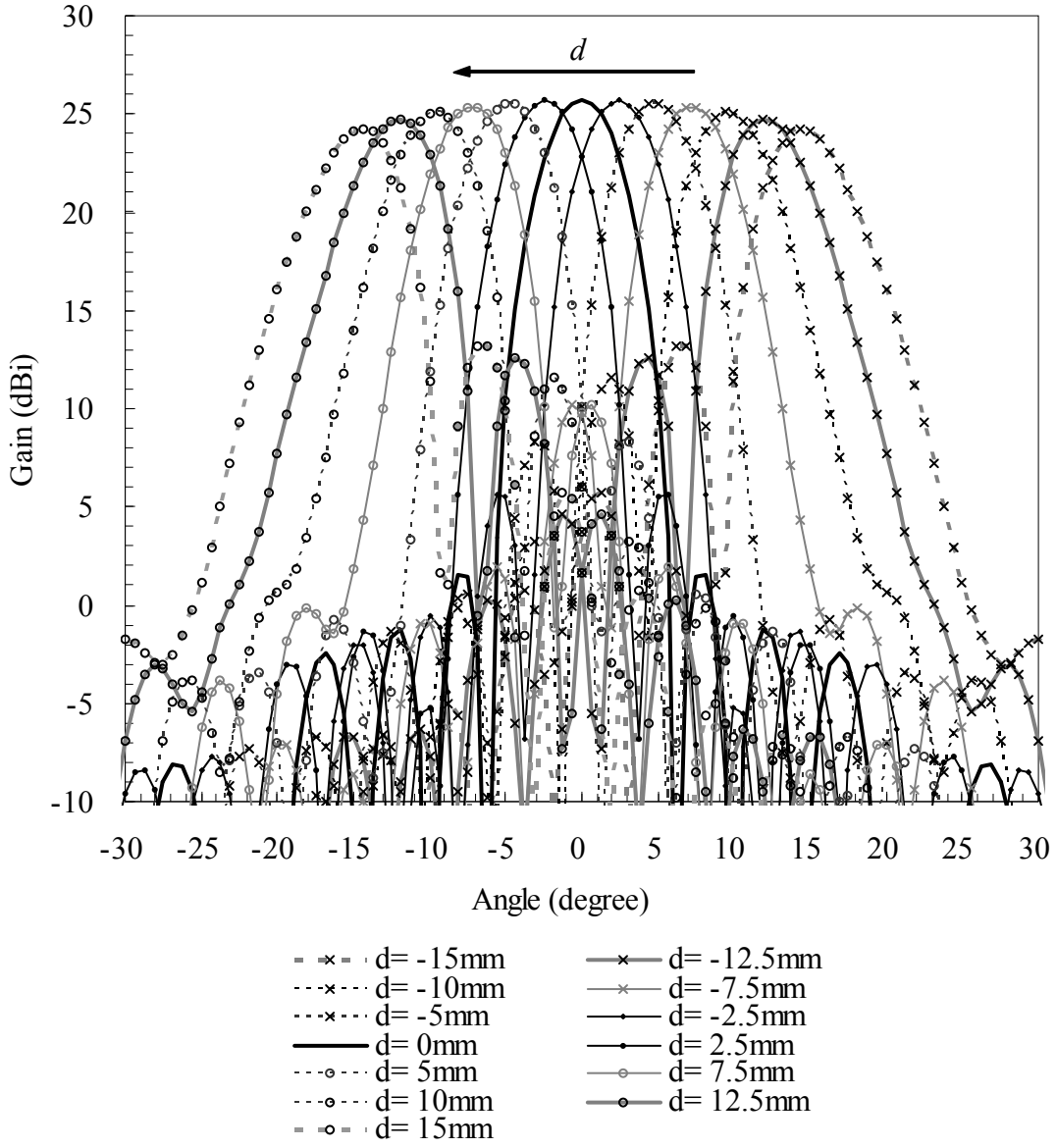

Figure 3.7 Calculated H-plane patterns of the folded reflectarray antenna for various displacements (*d*) of the feed position at 38.5 GHz.

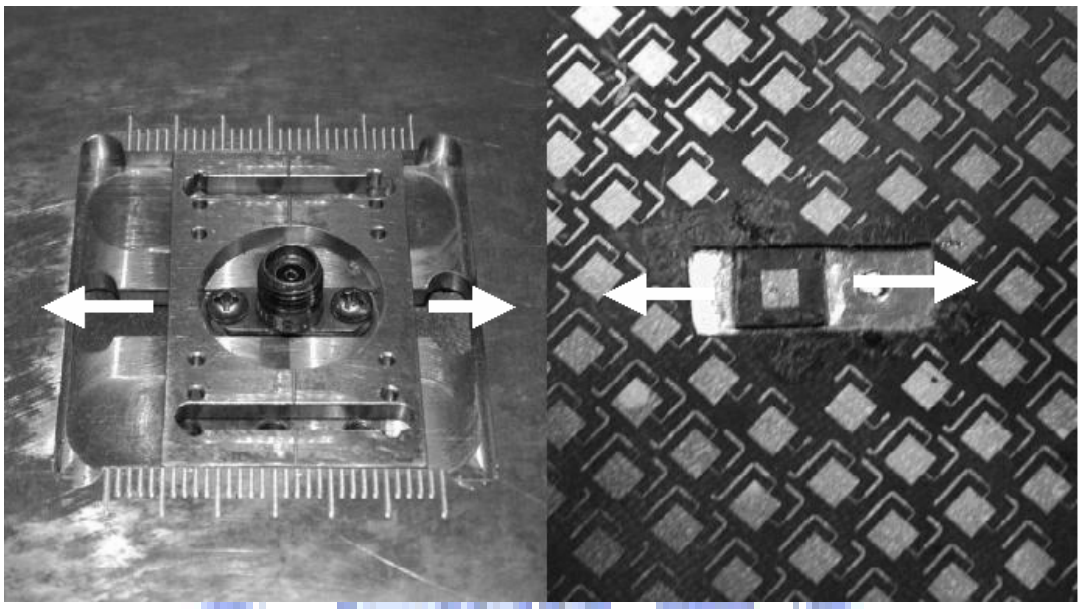

Figure 3.8　Bottom view (left) and top view (right) of the sliding track mechanism, which is mounted with the main reflector.

3.4 Results

Figure 3.10 shows the photo of the finished folded reflectarray antenna with the sub-reflector uncovered. An aluminum ring wall with inner diameter of 128 *mm* and height of 23 *mm* was used as the housing to support and separate the two reflectors. The three feeds for the radar mode are lined up along the x direction, with the intervals being 12.5 *mm*, and located at the center of the main reflector. While the feed for the communication mode is not on the same line as the radar mode feeds and away from the center by about 14.2 *mm*. The measurement results for both modes are presented in the following subsections.

3.4.1 Radar Mode

The measured return loss of the finished folded reflectarray for d = 0 mm feed is shown in Figure 3.11. It is –22.4 dB at 38.5 GHz. Figure 3.12 illustrates the measured H-plane patterns of the folded reflectarray antenna for various feed positions (d) at 38.5 GHz. Simulation results are also shown for comparison. It is seen that, as d changes from –12.5 mm to +12.5 mm, the main beam directs from +14.9° to –14.6°. The beam steering rate is a little larger than 1° per 1 *mm* movement, while the simulated main beam directions are +11.875o and –11.875o for d = –12.5 *mm* and d = +12.5 *mm* respectively. The measured gains of the antenna for d = –12.5 *mm*, d = 0 *mm*, and d = +12.5 *mm* are 22.5 dBi, 27.4 dBi and 22.6 dBi respectively. The maximum aperture efficiency is about 33.9%, which is better than the simulated one of 23.0%. The measured 3-dB beamwidths are 4.9^{o} in the E-plane and 4.4° in the H-plane. Besides, the measured side lobe levels are –15.5 dB in the E-plane and –18.8 dB in the H-plane.

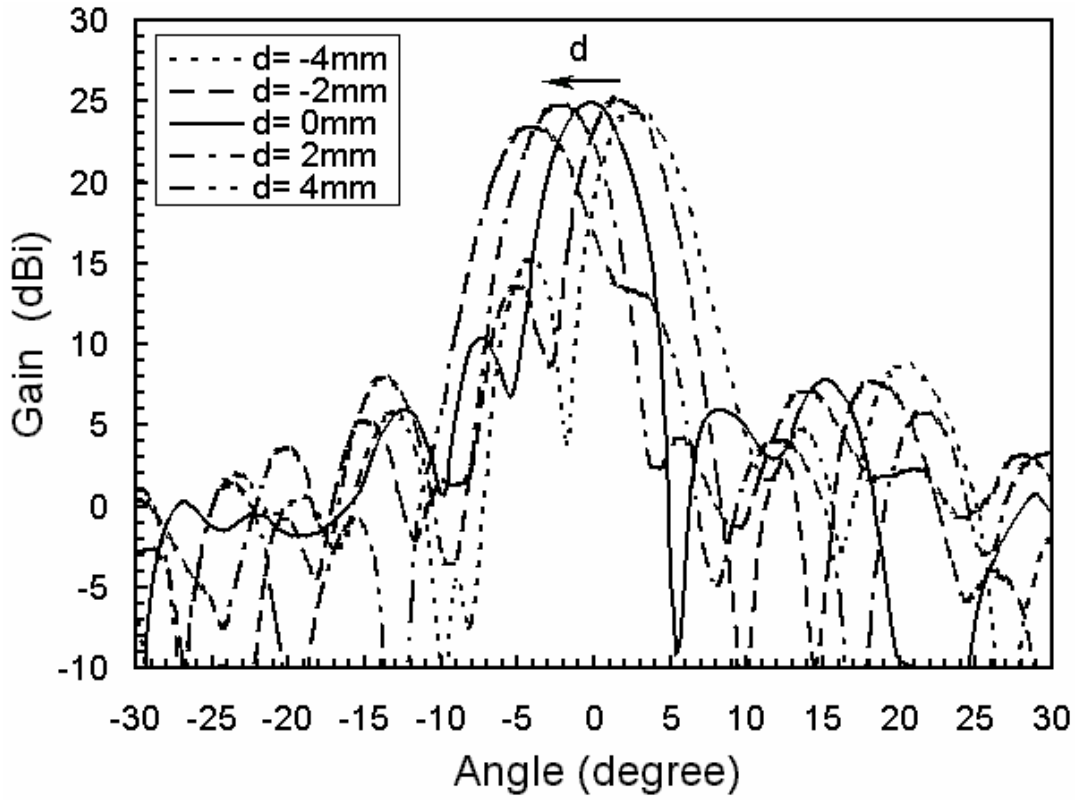

Figure 3.9 The measured H-plane patterns for various feed positions (*d*) at 38.5 GHz.

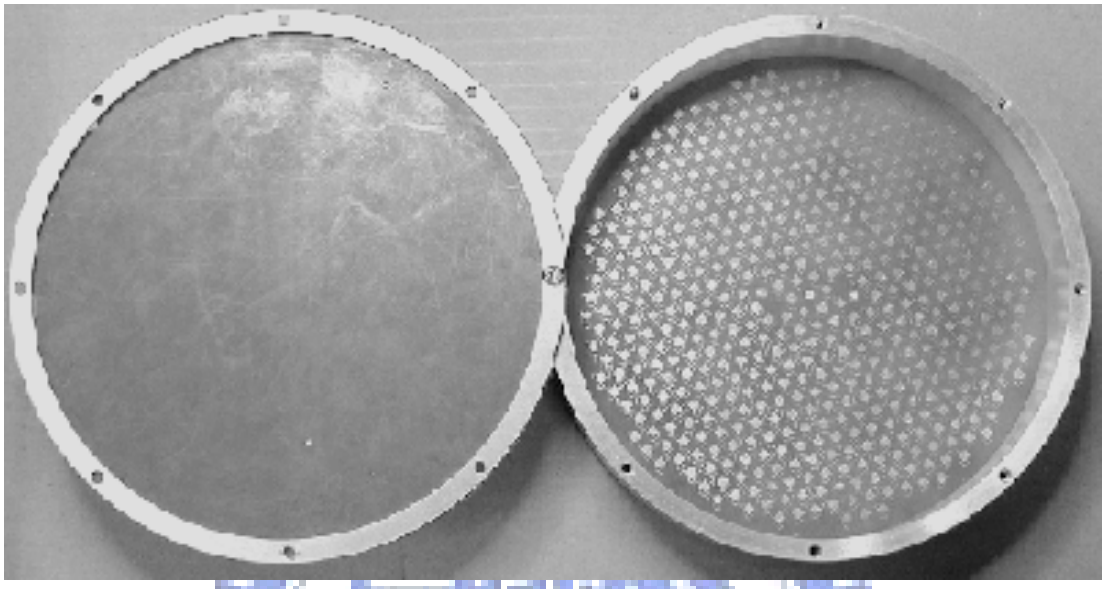

Figure 3.10 Photo of the finished folded reflectarray antenna.

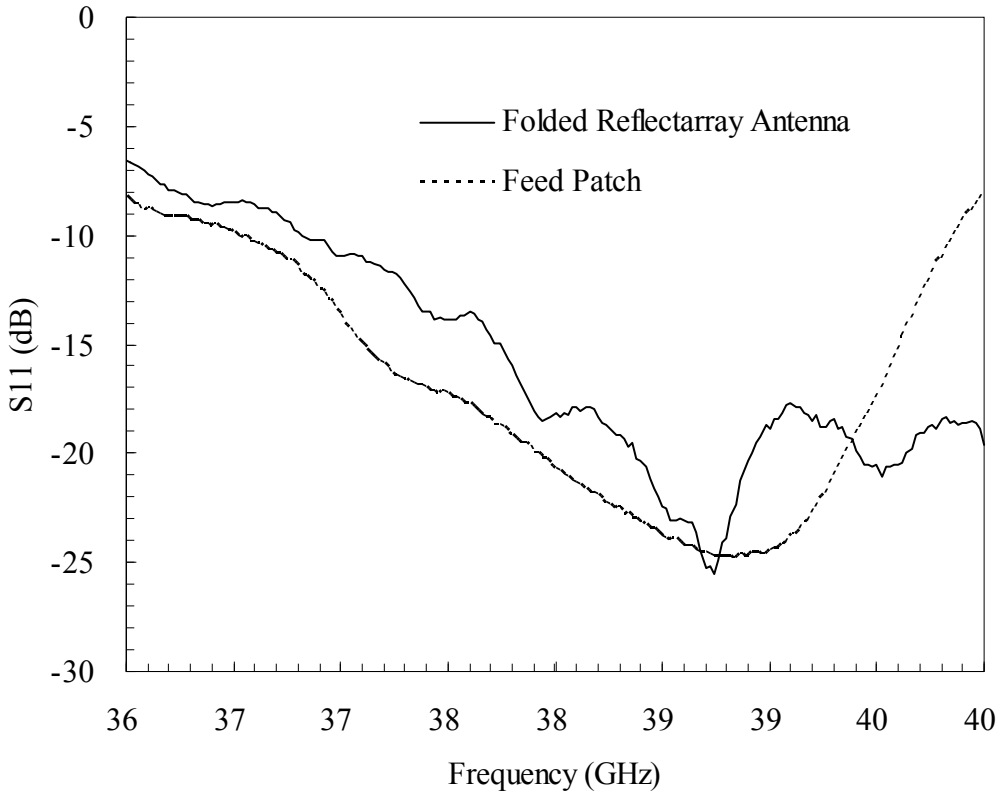

Figure 3.11 The measured return losses of the fabricated folded reflectarray antenna for *d*= 0 *mm* feed in the radar mode, and the single feed patch.

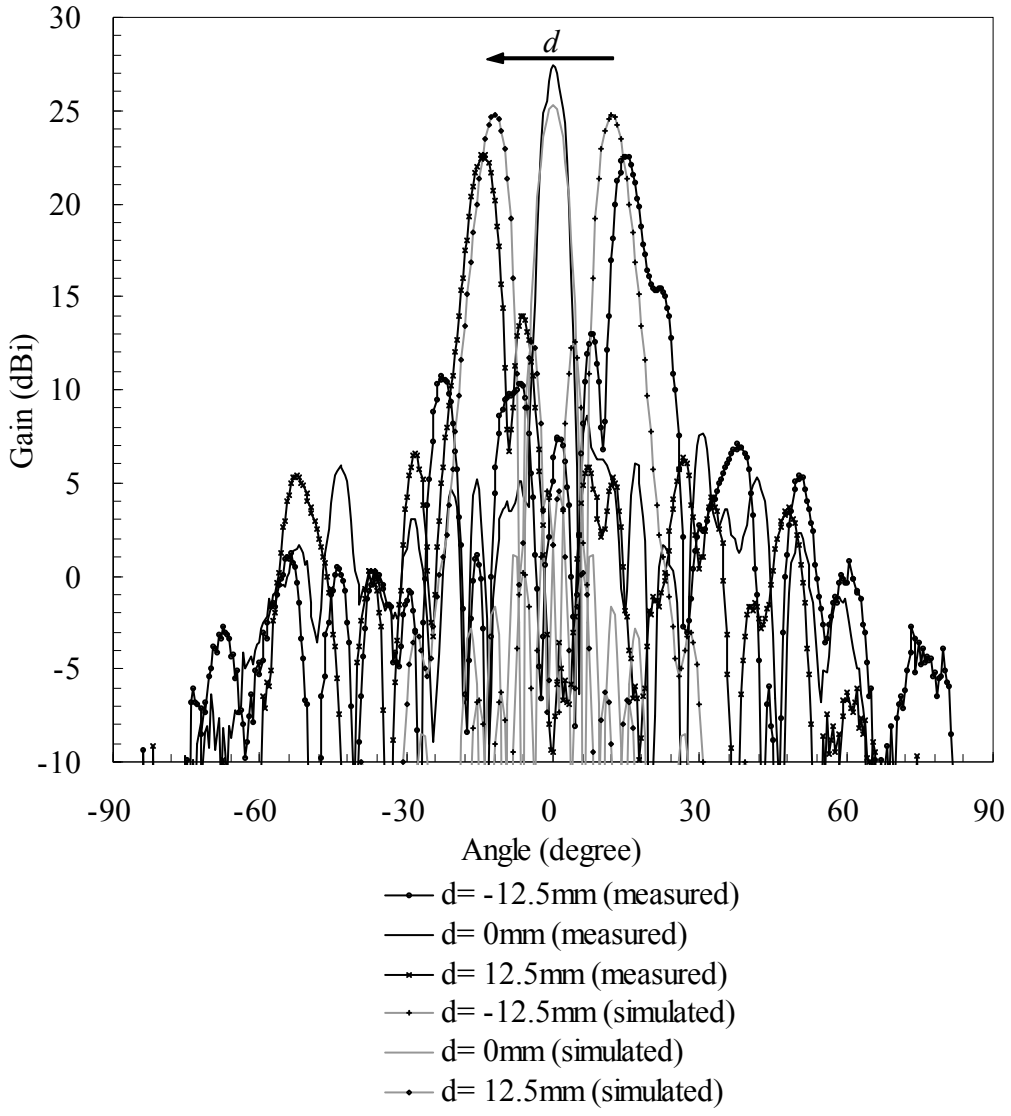

Figure 3.12 The radar mode H-plane patterns of the folded reflectarray antenna at 38.5 GHz for various feed positions (*d*).

The measurement results agree well with the simulations in the main beam region, yet behave worse in the side lobe areas owing to the blockage of the feed antennas and the phase errors caused by mutual couplings between the square patches. Also, parts of the waves reflected at the grid lines are re-reflected at the main reflector and spreading around in the antenna, leading to increased side lobes.

In fact, the beam scanning angle introduced by placing the feed off the focal point decreases with focal length to diameter ratio for a reflector antenna. Nonlinear phase as a function of feed displacement leads to pattern distortion, including beam broadening, rise in side lobe levels, and gain loss. These effects worsen with increasing feed displacement for a reflector antenna with a short focal length like this [16].

3.4.2 Communication Mode

The communication mode is expected to have a pattern resembles that of the feed patch. Unfortunately, the measured pattern exhibits a high ripple level. The major reason would be that, on the main reflector, the square patch elements in the close proximity of the communication mode feed patch would be excited by the couplings from that feed, and the radiations from those excited square patch elements would spoil the pattern. In addition, the cross-polarization component of the communication mode feed operates in the radar mode, which will be reflected by the sub-reflector and then re-radiated from the square patches, so that the pattern will be interfered. The introduction of the sub-reflector would be another influential factor.

In order to ameliorate the ripple level, the sub-reflector was first removed, and then the effects of various treatments on the feed patch for the communication mode were investigated. The feed patch was enclosed by metal traces with different shapes and widths. Some of the most efficient methods are illustrated in Figure 3.13.

It is obvious that, with the metal traces, the patterns have been considerably improved, as shown in Figure 3.14. The case that the feed patch surrounded by a metal square frame (Figure 3.13(d)) was selected and implemented, because its pattern is most similar to that of a typical patch antenna and has the most mitigated fluctuations. The co-polarization pattern becomes smoother and more symmetric, and the gain is slightly increased. This decision is also corroborated by the fact that the measured cross-polarization fields are at least 10 dB lower than that without the metal square frame, as shown in Figure 3.15. The measured return losses of the finished folded reflectarray for various feed antennas presented in Figure 3.13 at 38.5 GHz are shown in Figure 3.16. The return loss at 38.5 GHz for the case with Figure 3.13(d) as the feed is –21.4 dB.

Then, the sub-reflector was re-installed while keeping the square frame enclosed patch (Figure 3.13(d)) as the feed. The measured pattern is shown in Figure 3.17. The pattern of using the original patch as the feed (Figure 3.13(a)), with the sub-reflector installed, is also shown for comparison. It can be seen that the modification made to the feed has alleviated the sharp dips, and raised the averaged gain by about 2dB, especially near the broadside direction (e.g. -30^{o} to $+30^{o}$). Although the ripples are not thoroughly removed, this pattern performs satisfactorily for the inter-vehicle communications, which is an application of short-range wireless technology.

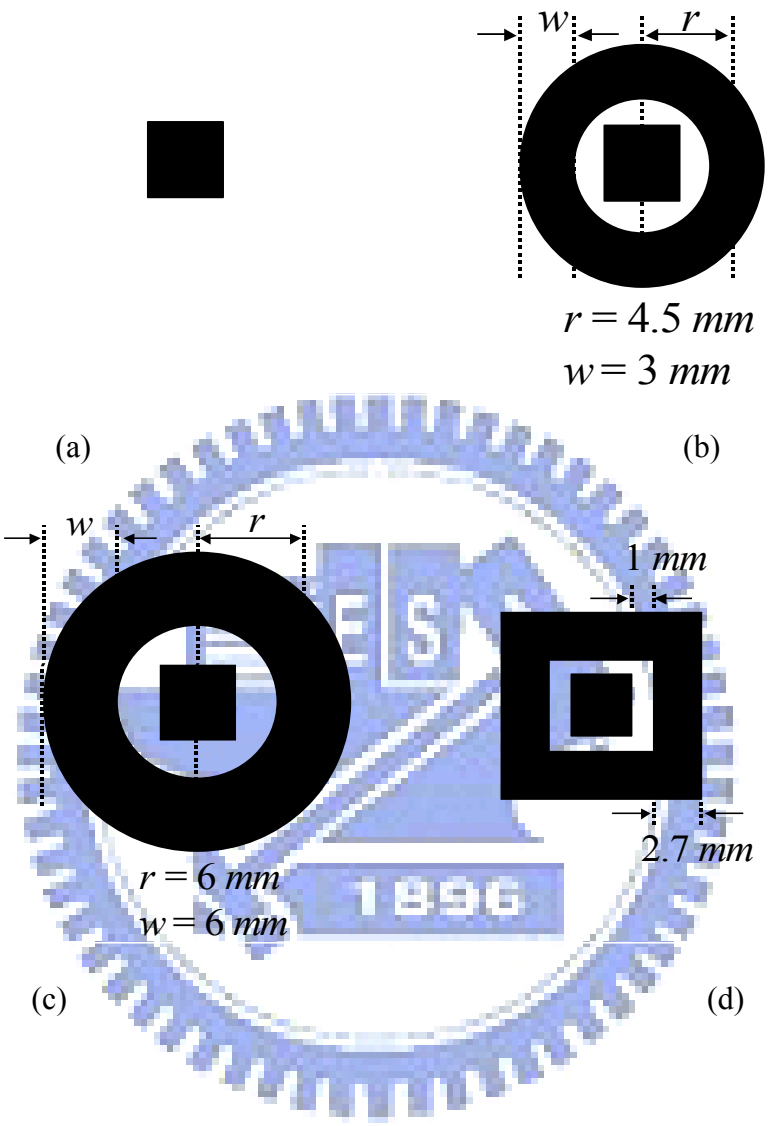

Figure 3.13 Four communication mode feed antennas: (a) The original feed patch described in section 3.3. (b) The original feed patch enclosed with a metal ring trace. The width of the trace (w) is 3 *mm* and the radius of the ring (r) is 4.5 *mm*. (c) The original feed patch enclosed with a larger metal ring trace. Both the width of the trace (w) and the radius of the ring (r) are 6 *mm*. (d) The original feed patch enclosed by a metal square frame, with the trace width being 2.7 *mm* and the gap being 1 *mm*.

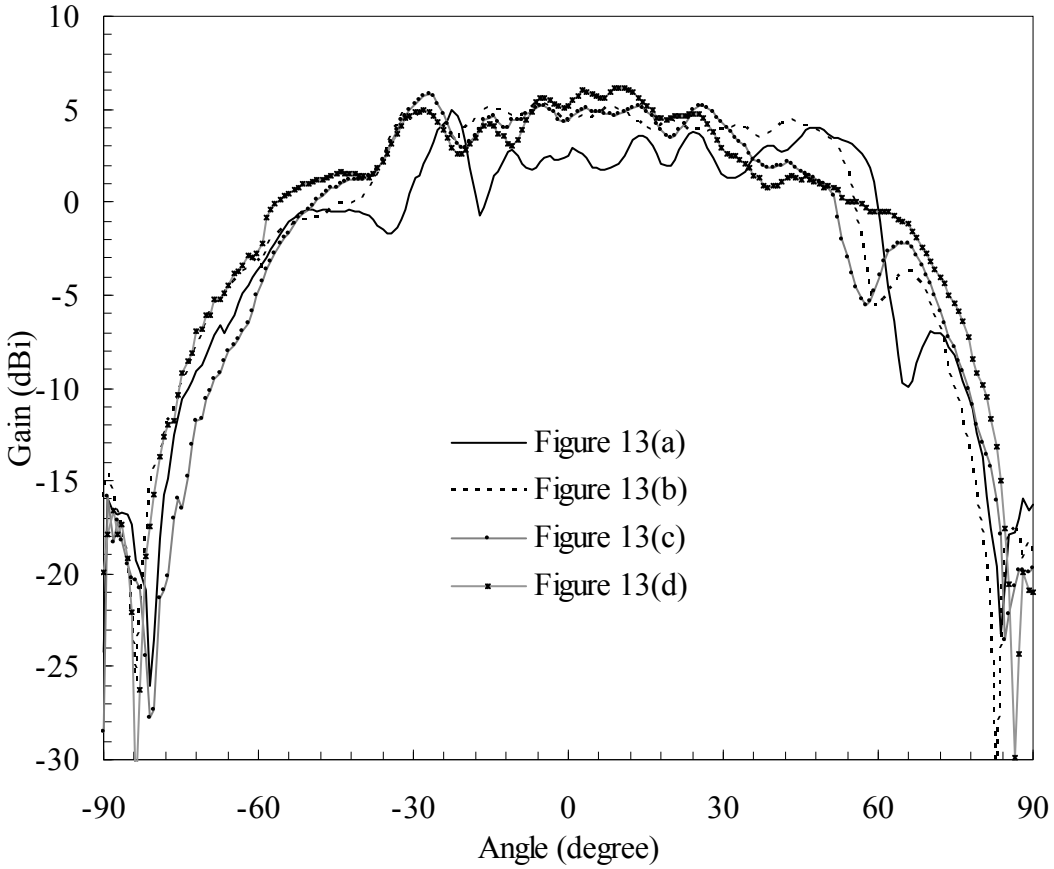

Figure 3.14 The measured patterns for various feed antennas presented in Figure 3.13, with the sub-reflector removed.

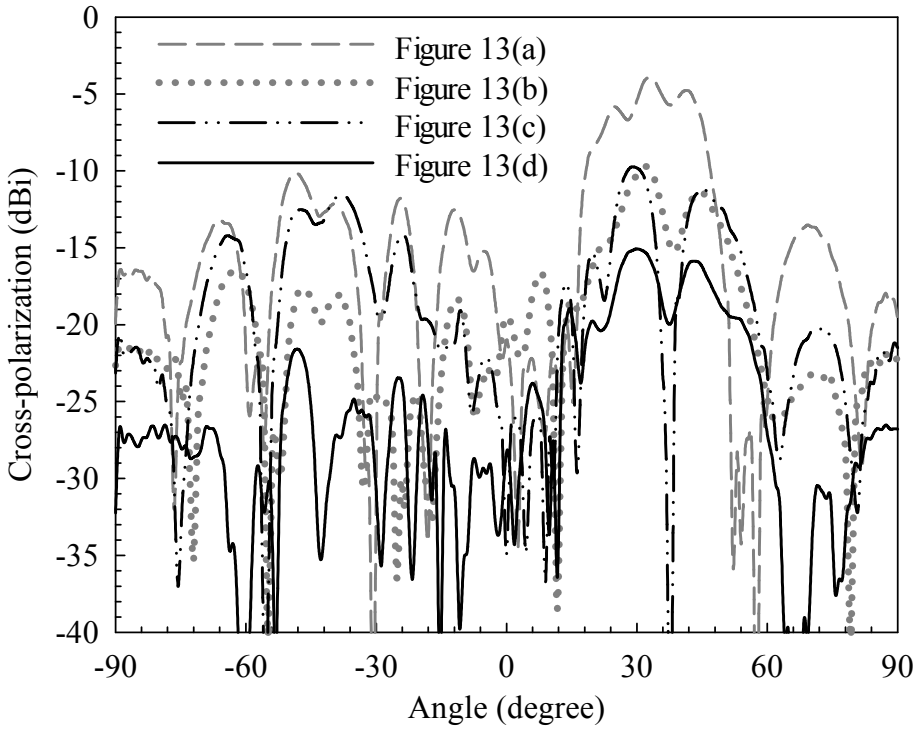

Figure 3.15 The measured cross-polarization patterns for various feed antennas presented in Figure 3.13, with the sub-reflector removed.

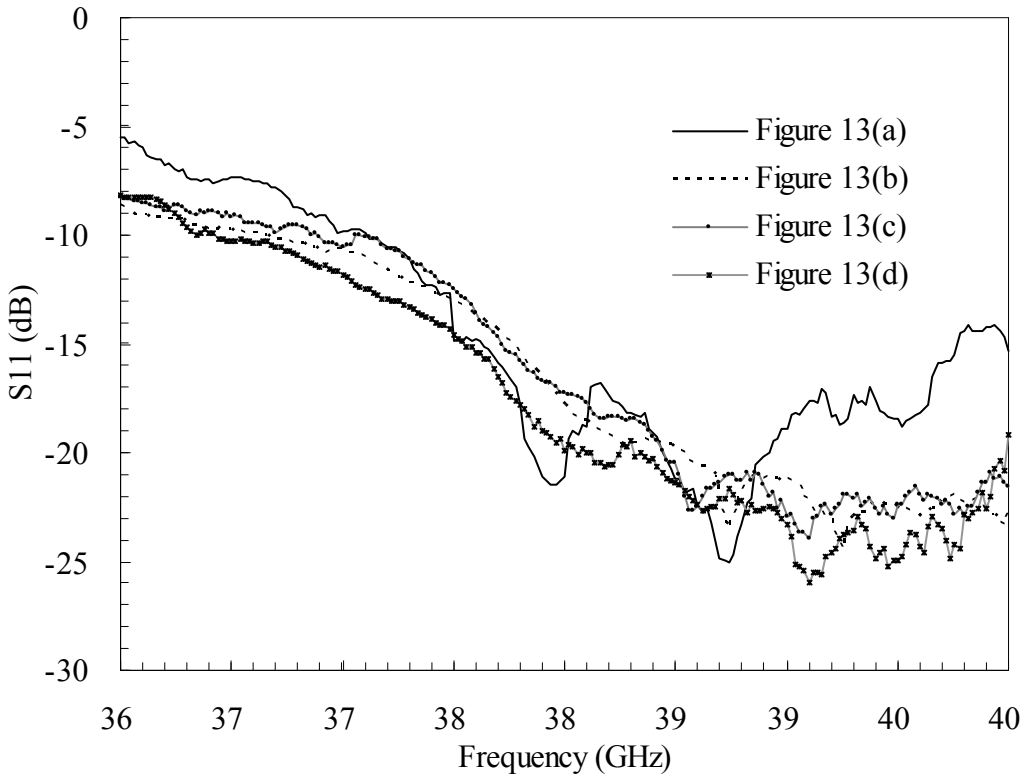

Figure 3.16 The measured communication mode input reflection coefficients of the fabricated folded reflectarray antenna, for various feed antennas presented in Figure 3.13.

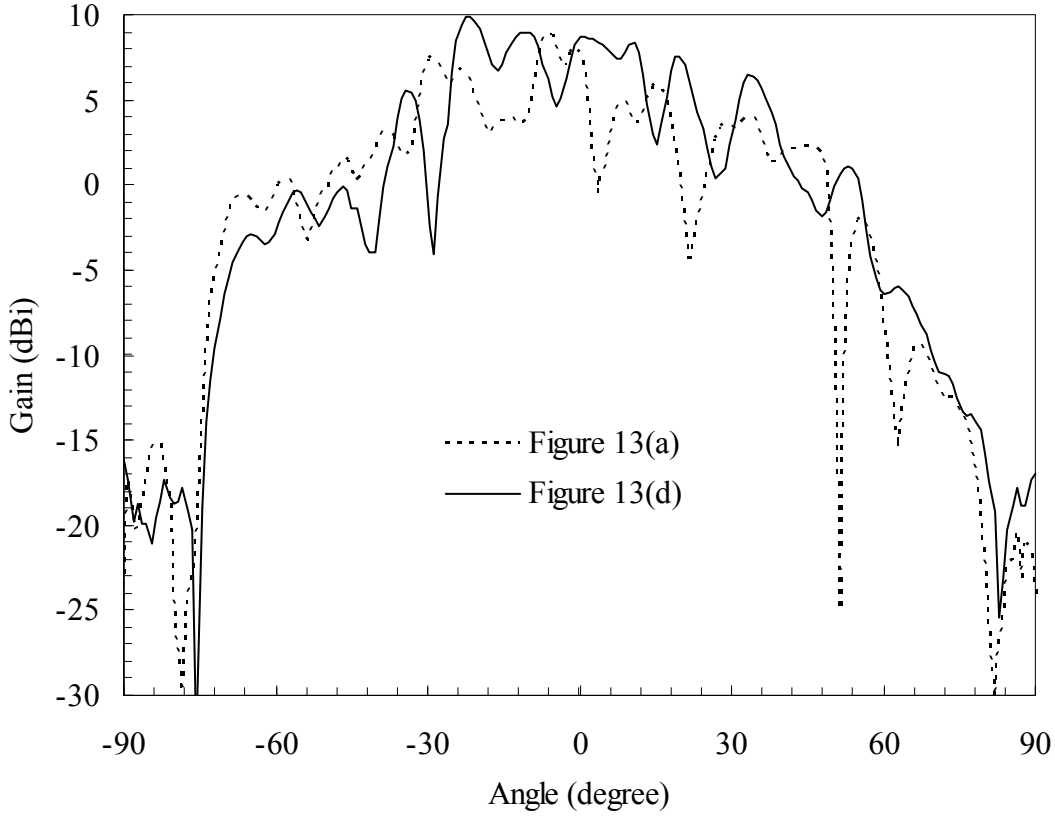

Figure 3.17 The measured patterns at 38.5 GHz, with sub-reflector, for: (a) original feed patch (Figure 3.13(a)), (b) original feed patch enclosed by a metal square frame (Figure 3.13(d)).

As comparing Figure 3.14 with Figure 3.17, it is found that the sub-reflector has some effect on the radiation pattern. The non-uniform phase delays experienced when the transmission fields radiated from the feed passing through the sub-reflector result in side lobes in the pattern because the design of the sub-reflector was done on the basis of normal incidence of a plane wave. The ripple level could be further improved once the transmission phase characteristics of oblique incident waves with various angles from the feed are taken into consideration of the sub-reflector design.

At last, the metal ring wall was removed and several dielectric posts were used instead to support the main reflector and sub-reflector. The patterns were measured and the results show that the influence of the metal wall is insignificant.

3.5 Conclusions

A 38.5 GHz dual-mode folded reflectarray antenna has been proposed and demonstrated. In the radar mode, the radiation beam can be steered by switching between feeds. Three feed patches for the radar mode were implemented at different positions of the main reflector. The total beam switching angle is 29.5^{o}. At the design frequency, the finished folded reflectarray antenna possesses an antenna gain of larger than 20 dBi within the beam switching range. A maximum gain of 27.4 dBi and the corresponding aperture efficiency of 33.9% were achieved. While for the communication mode, the ripple in the pattern was improved by enclosing the feed patch with a square metal frame. The proposed millimeter-wave folded microstrip reflectarray antenna works well for both the radar and communication mode, which is one of the likeliest candidates for an ITS antenna.

References

1. D. G. Barry et al, "The reflectarray antenna," *IEEE Trans. Antennas Propagat.*, vol. AP-11, pp.645–651, Nov, 1963.

2. D. M. Pozar, S. D. Targonski, and H. D. Syrigos, "Design of millimeter wave microstrip reflectarrays" *IEEE Trans. Antennas Propagat.*, vol. 45, no. 2, pp.287–296, Feb. 1997.

3. R. D. Javor, X. D. Wu, and K. Chang, "Design and performance of microstrip reflectarray antenna" *IEEE Trans. Antennas Propagat.*, vol. 43, no. 9, pp.923–939, Sept. 1995.

4. J. Huang, "Microstrip reflectarray," in *Proc. IEEE Int. Symp. Antennas Propagat.*, pp.612-–615, June 1991.

5. J. Huang, "Capabilities of printed reflectarray antennas," *IEEE Symp. Phased Array Systems and Tech.*, Boston, Massachusetts, pp. 131–134, Oct 1996.

6. J. Huang, "Bandwith study of microstrip reflectarray and a novel phased reflectarray concept," *IEEE Trans. Antennas Propagat.*, vol. 45, pp. 287–295, Feb. 1997.

7. K. Y. Sze, and L. Shafai, "Microstrip patches for a reflectarray," in *Proc. IEEE Int. Symp. Antennas Propagat,*, vol. 3, pp. 1666–1669, 1999.

8. D. Pilz, and W. Menzel, "Folded reflectarray antenna," *Electronics Lett.*, vol. 34, no. 9, pp.832–833, Apr. 1998.

9. W. Menzel, D. Pilz, and R. Leberer, "A 77GHz FM/CW radar frontend with a low-profile, low-loss printed antenna," *IEEE MTT-S Digest*, pp. 1485–1488, 1999.

10. J. Huang, "The development of inflatable array antennas," *IEEE Magazine*

Antennas and Propagat., vol. 43, no. 4, pp. 44–50, Aug. 2001.

11. M. Thiel; and W. Menzel, “A multiple-beam sector antenna with a dual planar reflectarray arrangement,” in *Proc. 3rd European Radar Conf.*, Manchester, Sept. 2006, pp.53–56.

12. W. Menzel, M. Al-Tikriti, and R. Leberer, “A 76 GHz multiple-beam planar reflector antenna,” in *Proc. European Microw. Conf.*, Milano, Italy, Sept. 2002, vol. 3, pp. 977–980.

13. W. Menzel, D. Pilz, and M. Al-Tikriti, “MiIlimeter-wave folded reflector antennas with high gain, low loss, and low profile,” *IEEE Magazine Antennas Propagat*, vol. 44, no. 3, pp. 24–29, June 2002.

14. J. A. Zornoza, R. Leberer, J. A. Encinar, and W. Menzel, "Folded multilayer microstrip reflectarray with shaped pattern," *IEEE Trans. Antennas Propagat.*, vol. 54, no. 2, pp. 510–518, Feb. 2006.

15. J. Huang, and R. J. Pogorzelski, “Microstrip reflectarray with elements having variable rotation angles,” in *Proc. IEEE Int. Symp. Antennas Propagat*, vol. 2, pp. 1280–1283, 1997.

16. W. L. Stutzman, and G. A. Thiele, *Antenna Theory and Design*, New York: John Wiley & Sons Inc., 1997, pp. 338–342.

4 A 60 GHz Circular Polarization Selective Surface by Printed Circuit Technology

4.1 Introduction

Linear-polarization selective surfaces in modern reflector antenna design, such as reflectarray antennas [1]-[2], have been known and used for a long time. Many applications, stemmed from linear polarization (LP) selection could be converted to applications based on circular polarization (CP) selection, e.g., satellite communications, navigation systems, wireless LAN, automotive radar, and remote sensing radar applications. On the other hand, CPSS has been rarely used. With the emergency of excellent CPSSs, folded reflectarray could be extended to circular polarization applications.

A lossless and perfect CPSS would pass one sense of CP wave while reflecting the other. Based on the reciprocity theorem, it is easy to derive that the reflected wave for the reflection case, possesses the same polarization sense as the incident wave, and the transmitted wave for the transmission case must be of the same polarization as the incoming wave. Therefore, an ideal left-hand circular polarization selective surface (LHCPSS) would thoroughly reflect a left-hand circularly polarized (LHCP) incident wave, while at the same time be completely transparent to a right-hand circularly polarized (RHCP) incident wave. Likewise, an ideal right-hand circular polarization selective surface (RHCPSS) would be opaque to a RHCP wave and yet transparent to a LHCP wave.

Considering the similarity of LHCPSS and RHCPSS, only the RHCPSS will be covered in this work. Through the method of moments (MoM) associated with the

periodic Green's function, many simulations were performed. From these simulations, the optimal parameters were obtained. Finally, a 60 GHz RHCPSS using printed circuit technology was accordingly designed, constructed and measured.

4.2 Operational Principle

An original CPSS design was proposed in [3], which is formed by a two-dimensional array. Each array element consists of two orthogonal and resonant dipoles separated by $\lambda/4$ in height; with their center feed points connected together by a $\lambda/2$ transmission line, where λ is the wavelength. Material with appropriate dielectric constant is used to make the transmission line appear 180^{o} electrical length in $\lambda/4$ spacing. The two dipoles are meant to receive two orthogonal components of the incident wave respectively. Because of the $\lambda/4$ separation between the two dipoles, the two orthogonal components of a circularly polarized wave would arrive at the respective dipoles either in-phase or 180^{o} out of phase, depending on the polarization state. A circularly polarized wave impinging on the RHCPSS will be reflected when the two corresponding components of the wave reach the respective dipoles in-phase and will be transmitted when the two corresponding components of the wave reach the respective dipoles out of phase.

This design is intuitive, but there exist problems in practice. The main difficulty is that the geometry and the medium of the transmission line must be properly designed to make the separation of the two dipoles $\lambda/4$ and the electrical length to be $\lambda/2$ simultaneously. In addition, considerations must be taken to maintain impedance matching between the dipoles and the transmission line. It is therefore not easy to realize this structure for use at high frequencies. As a result of the complexity, another design was discovered [4]-[5].

A CPSS with an analogous concept but simpler structure was proposed in this work. This design is a bent wire formed from three jointed orthogonal segments, having a total length of about 1λ, as illustrated in Figure 4.1. The transmission line has been replaced with a direct wire segment, maintaining a vertical distance of λ/4, but the electrical length is no longer a consideration. The two transverse straight wires, connected by the upright segment, are approximately 3/8λ and pointed in perpendicular directions. This structure can be fabricated in a laminate by using printed circuit technology: the two transverse wires are created by two metal traces and the vertical segment is accomplished by a conductive via.

At any arbitrary time, the locus of the instantaneous electric field vector tip of a circularly polarized wave traces out a helix. Every quarter wavelength shift along the propagation direction causes a quadrature phase difference, so that the electric field rotates 90^{o} in the transverse plane. For RHCP wave illuminated at normal incidence, the respective induced currents on the two transverse wires are in-phase, the two wires behave like dipoles with sinusoidal- like current distribution on them, and a null appears in the middle of the vertical segment. The entire bent wire thus operates at geometrical resonance, and the dipoles re-radiate waves in both the +z and –z directions. Below the substrate, the scattered wave propagates in the –z direction with the same polarization sense as the incident CP wave. Meanwhile above the substrate, the incident and scattered wave add 180^{o} out of phase, thus producing a null field in that region.

Regarding to LHCP illumination, the currents induced by the rotating electric field of the incident wave add 180o out of phase, and tend to cancel each other out. The current distribution is much lower and no longer sinusoidal-like, and the scattered wave is thus much weaker. The reflected wave in this case is negligible and the

incident wave in the transmission region is scarcely disturbed.

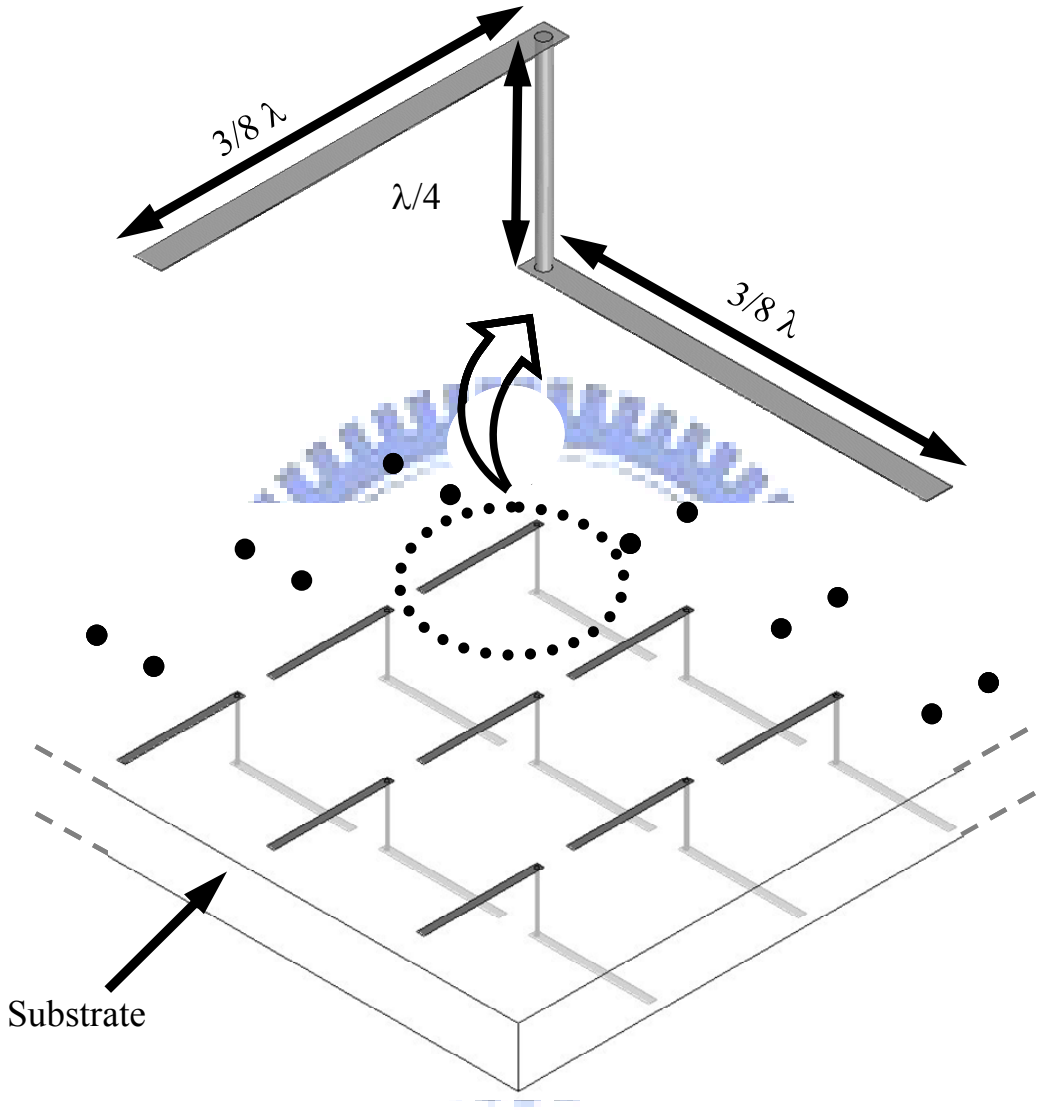

Figure 4.1 Schematic of the CPSS. The constituent structure is a bent wire formed with three jointed orthogonal segments. The total length of the whole wire is about 1λ.

4.3 Analysis Method

The numerical calculations begin with derivation of the Green's function for stratified media. The vector potential $\vec{A}$ due to the presence of a current distribution $\vec{J}$ in the source region is expressed as:

$$\vec{A}(x,y,z) = \iiint_{x',y',z'} \bar{G}(x,y,z,x',y',z') \cdot \vec{J}(x',y',z')dv' \tag{4.1}$$

where the spatial domain Green's function $\widetilde{G}$ are represented by the Sommerfeld integral as:

$$\bar{G}(x,y,z) = \frac{1}{4\pi} \int_{SIP} k_\rho H_0^{(2)}(k_\rho \rho) \widetilde{\bar{G}}(k_\rho) dk_\rho \tag{4.2}$$

with $H_0^{(2)}$ being the Hankel function of the second kind and SIP the Sommerfeld integration path. The spectral domain Green's functions $\widetilde{G}$ for vector potential are derived in closed form in the source layer [6]-[7]. These expressions are then extended to an arbitrary layer through an iterative process individually for TE and TM components of the Green's functions in the source layer. The coefficients appeared in the Green's functions are functions of the generalized reflection coefficients, which can be obtained by applying appropriate boundary conditions for the proposed configuration. The main difficulty lies in the Hankel transform was resolved by employing the saddle point technique in this work, because the Green's functions in the far field region are smoothly varying functions of distance.

For a planar infinite array, the periodic Green's function $\widetilde{G}_p$ is expressed in terms of a sum of the spectral domain Green's functions for layered structure [8]-[9] as:

$$\vec{G}_p = \frac{1}{ab}\sum_m \sum_n \tilde{G}(k_{xm}, k_{yn}) \cdot e^{-jk_{xm}(x-x')} \cdot e^{-jk_{yn}(y-y')} \tag{4.3}$$

where

$$k_{xm} = k_x^i + \frac{2\pi m}{a}, k_{yn} = k_y^i + \frac{2\pi n}{b} \tag{4.4}$$

a and b represent the x- and y- periodicities of the structure. k_x^i and k_y^i are wavenumbers associated with the phase shifted plane wave.

In this work, the commercial software IE3D [10] based on Method of Moments was utilized to calculate the induced current $\vec{J}$. For simplicity of analysis, the unit cell of a CPSS was duplicated to form a 3×3 array, with periodic boundary conditions applied on the four sides (see Figure 4.2). No significant differences in the calculated currents were observed by having any larger array from preliminary simulations.

This product, of the currents extracted from the center unit cell of the 3×3 array and the periodic Green's function, was substituted into (4.1) and integrated over the source region to obtain the vector potential $\vec{A}$. Then the far-field RHCP and LHCP components of the scattered field were derived for each illumination.

4.4 Results

The term "Isolation" in this chapter is defined as the amount of the designated polarization field blocked by the surface. The "Isolation" for a RHCPSS is found by applying a RHCP plane wave illumination, then measuring the difference of the RHCP field intensity received with and without the RHCPSS inserted in front of the receiver. On the other hand, the "Transmission Loss" is found by measuring the difference of the LHCP field received with and without the RHCPSS inserted into a LHCP plane wave illumination.

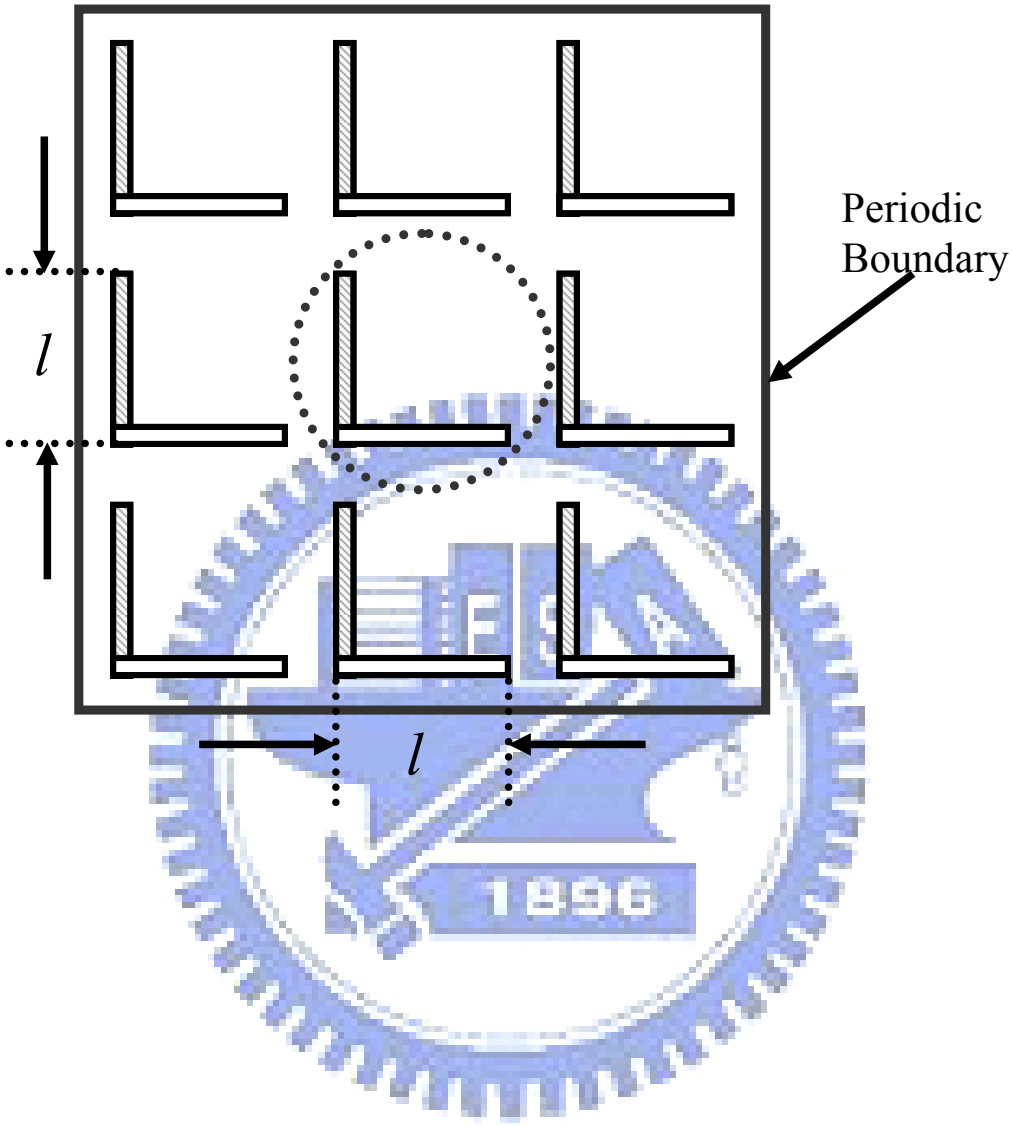

Figure 4.2 The 3×3 array used for analysis. The currents on the center unit cell are extracted for succeeding manipulations.

The dielectric constant and the thickness of the substrate would suggest an appropriate selection of the laminate. There are many commercially available, off-the-shelf products, which are suitable for the development of CPSSs. A laminate with a dielectric constant of 2.33 (Duroid 5870) and 31-*mil* thickness was chosen for this work, because, under such conditions, the distance the wave traveled in the substrate is the closest to $\lambda/4$ at the target frequency of 60 GHz.

According to the fabrication capability provided by PCB manufacturers, both the minimum achievable trace width and spacing are 4 *mils*, and the minimum achievable radius of a via is 2 *mils*. In this work, all trace widths and spacing are set to 0.1 *mm* (≈4 *mils*), and the lengths of both arms are identical. The periodicity of the array has an analogous effect on isolation and transmission loss. It is observed that the larger the periodicity is, the less the isolation and transmission loss appear. The periodicity is set to 2.2 *mm* as it maintains a good isolation.

The optimization process starts from taking $3\lambda/8$ as the initial value of the arm lengths (l). Then the arm lengths for different radii of the via are varied to achieve the optimal design. Figure 4.3 and Figure 4.4 display the simulated isolation and transmission loss against arm lengths at 60 GHz. The solid line and the dashed line respectively present the results obtained when the via radii (r) are 2 *mils* and 4 *mils*. It is seen that the isolation is a fast-varying function of the arm length, while the transmission loss is a slow-varying one. For the 2-*mil* via, the optimal length for largest isolation occurs at 1.5 *mm* with a corresponding isolation of 26.4 dB. At this length, the transmission loss is –0.43 dB. For the 4-mil via, the optimal length for largest isolation occurs at 1.425 *mm* with a corresponding isolation of about 22 dB and the transmission loss is –0.44 dB.

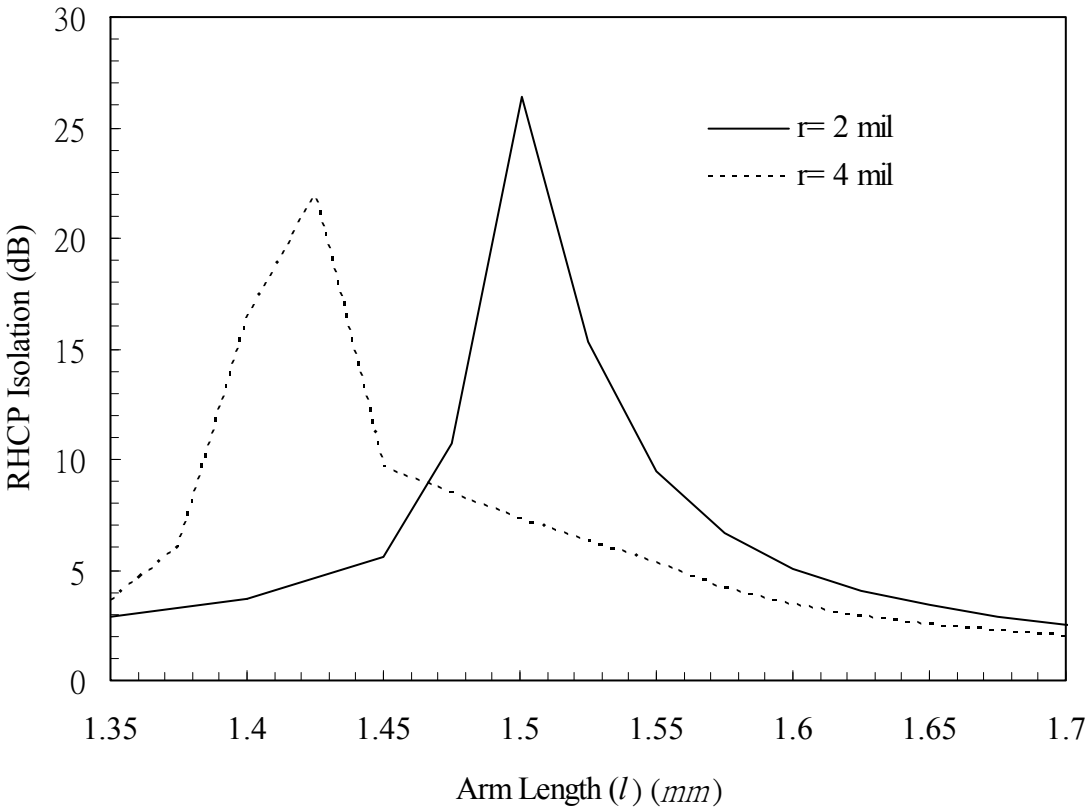

Figure 4.3 The simulated isolation for various lengths of arms. The radii (r) of the vias are 2 *mils* and 4 *mils*, respectively.

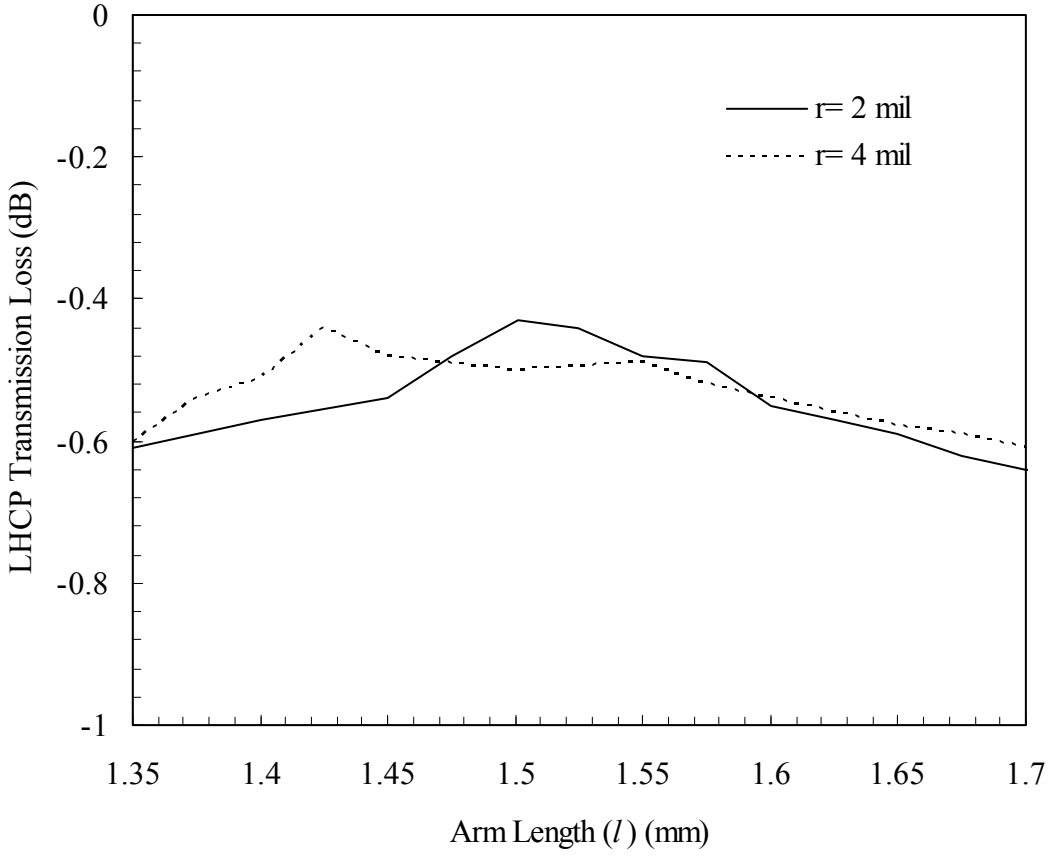

Figure 4.4 The simulated transmission loss for various lengths of arms. The radii (r) of the vias are 2 *mils* and 4 *mils*, respectively.

As Figure 4.3 and Figure 4.4 indicate, the performance of the circular polarization selectivity is extremely sensitive to the lengths of arms. The radius of the via also has significant influence; thinner via will have longer optimum arm lengths and a better performance. Thus, the design with the via radius of 0.05 *mm* and the arm length of 1.5 *mm* was determined for realization.

The finished RHCPSS has 1256 unit elements, made on a disk-shape substrate, with a radius of about 45 *mm*. However, it apparently differed from what had been proposed. The manufacturer, based on its accumulated experience, achieved a via by a hole with copper plating on the walls and two additional annular ring pads encompassing the hole on each side of the substrate in order to prevent the thin metallic traces from peeling off. Figure 4.5 is the photograph of the finished RHCPSS. The schematic diagram of the realized deformed structure observed with a microscope is also sketched. By measuring, the lengths from the center of the ring to the ends of the arms are 1.5 *mm*, and the inner radii of the rings are about 0.075 *mm*. However, the outer radii of the rings are inconsistent, ranging from 0.1 *mm* to 0.2 *mm*. In order to better understand the deviation, simulations that set the models with outer radii of 0.1 *mm*, 0.15 *mm*, and 0.2 *mm* and the unchanged arm length of 1.5 *mm* were performed. Figure 4.6 and Figure 4.7 illustrate the simulated results.

Measurements are performed with an Agilent 8510C VNA equipped with an extra milli-meter wave controller and a milli-meter wave test set. Two LP horns are collimated and aligned with each other. For shielding, a metal plate with a hole having the same radius as the CPSS is placed in between the two horns. The CPSS under test is installed in place of the hole. The distances between the RHCPSS and the two horns must be large enough to ensure the phase of the wave to be uniformly distributed over the aperture of the RHCPSS. It is set to 1 *m* in this work.

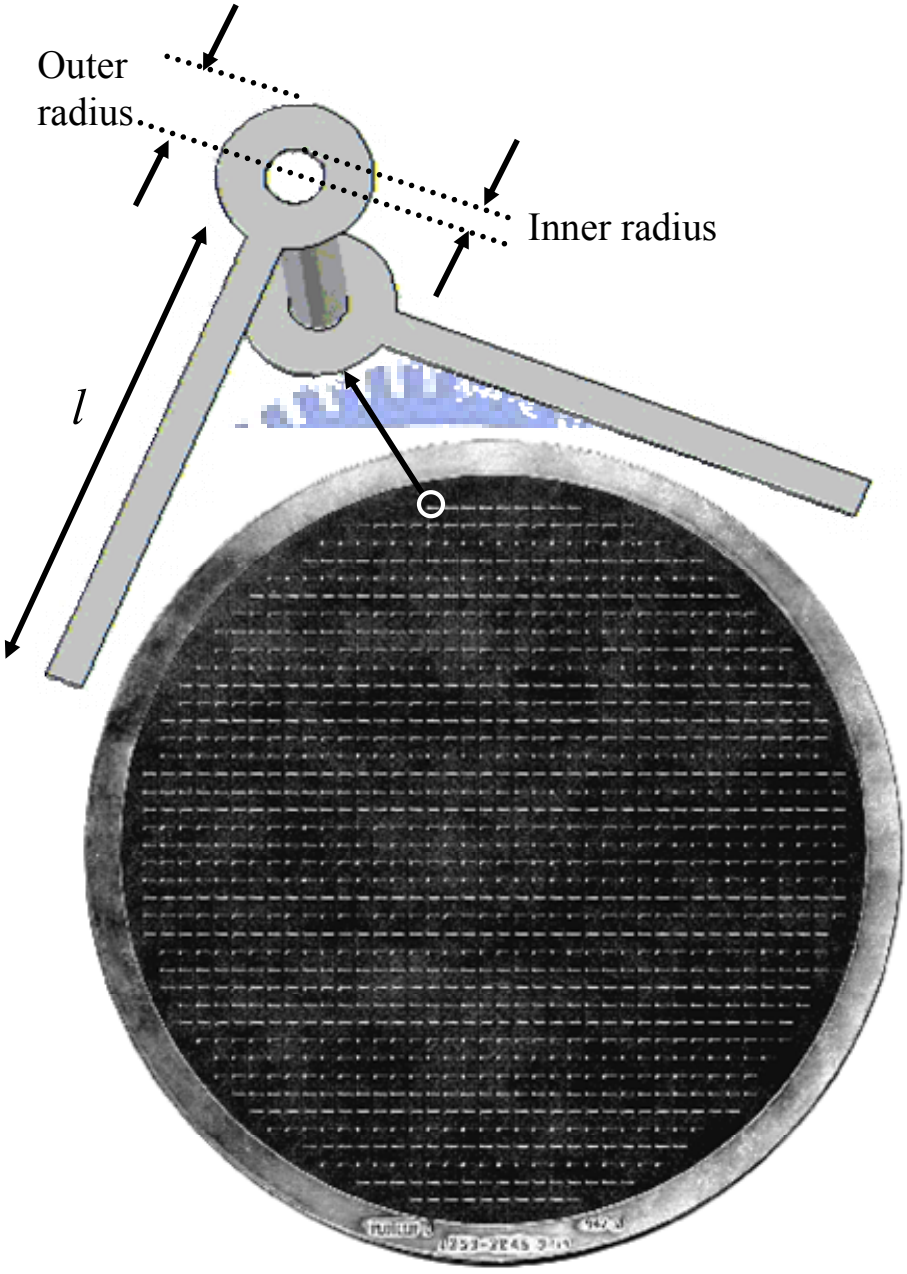

Figure 4.5 Photograph of the finished RHCPSS, which has 1256 elements on a disk-shape substrate. The radius of the disk is about 45 *mm*.

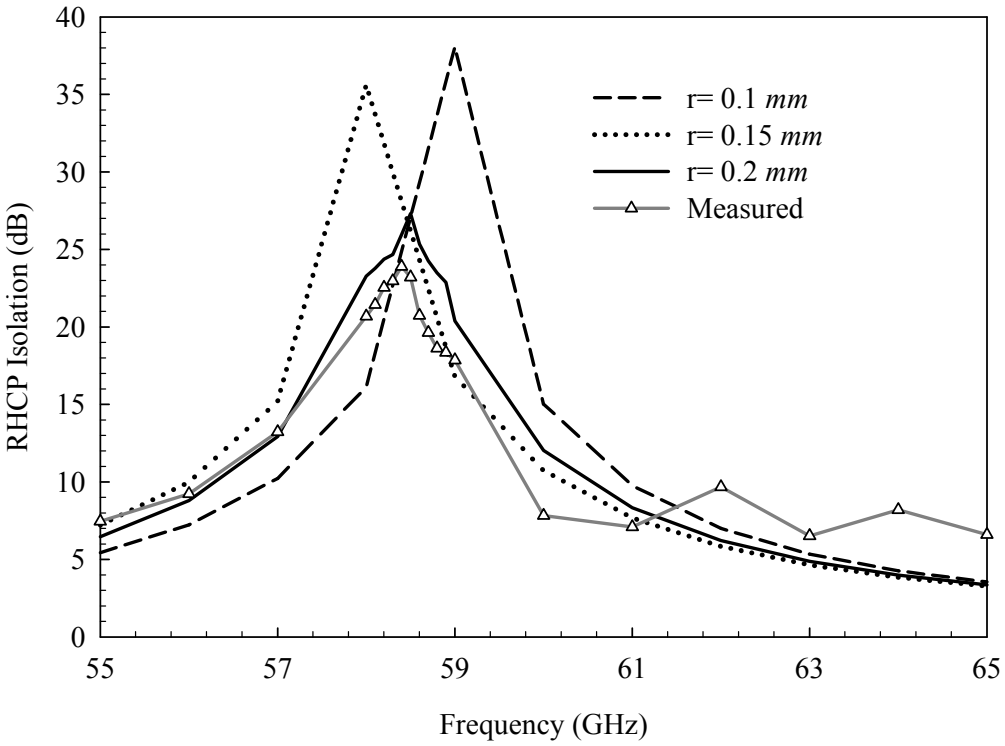

Figure 4.6 The simulated isolations for outer radius (r) of 0.1 *mm*, 0.15 *mm* and 0.2 *mm* (arm length *l*= 1.5 *mm*, inner radius= 0.075 *mm*), and the measured isolation of the finished RHCPSS.

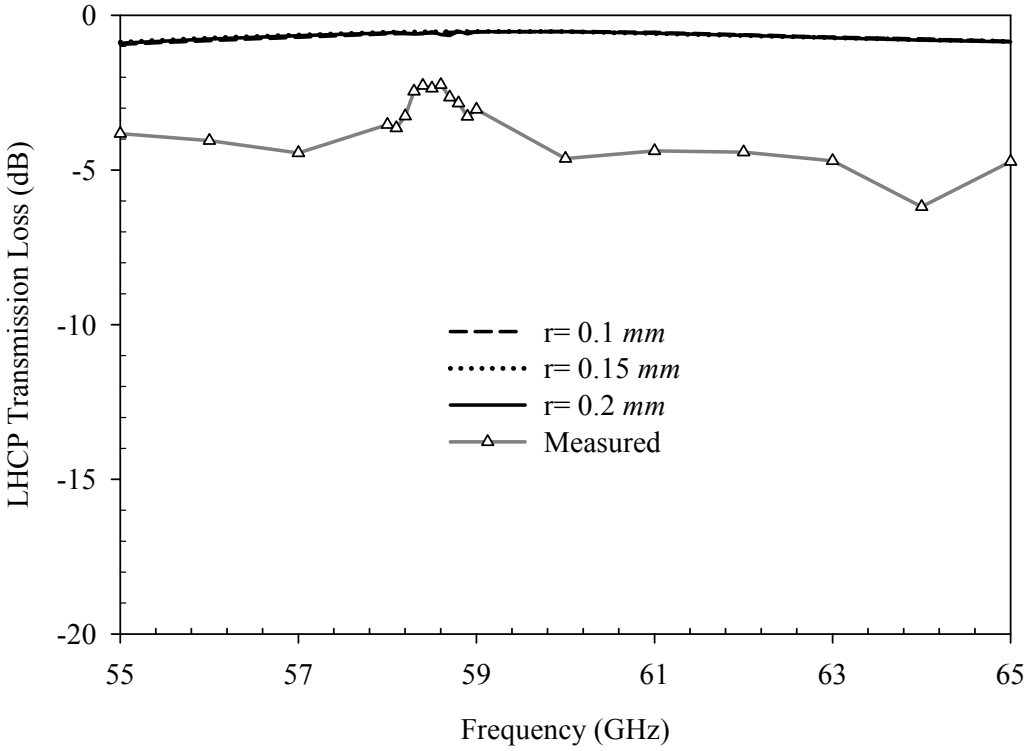

Figure 4.7 The simulated transmission loss for outer radius (r) of 0.1 *mm*, 0.15 *mm* and 0.2 *mm* (arm length *l*= 1.5 *mm*, inner radius= 0.075 *mm*), and the measured data of the finished RHCPSS.

Two LP horns are installed on the two ends of the network analyzer on account of the lack of standard CP horn antenna. The cross-polarization levels of the LP horns are less than –40 dB, whose effects are neglected in the following analysis. LP wave can be considered as a combination of a pure LHCP and a pure RHCP wave, each contributing half the power.

Let E_{Major} and E_{Minor} be the electric field magnitudes in respective major and minor axis of the polarization ellipse of a CP wave:

$$E_{Major} = (E_{L0} + E_{R0})/2 \ , \ E_{Minor} = (E_{L0} - E_{R0})/2 \tag{4.5}$$

where E_{L0} and E_{R0} denote the intensities of left- and right-hand components.

By definition, the axial ratio (AR) of a CP wave is:

$$|AR| = \frac{E_{Major}}{E_{Minor}} = \frac{E_{L0} + E_{R0}}{E_{L0} - E_{R0}} = \frac{1 + (E_{R0}/E_{L0})}{1 - (E_{R0}/E_{L0})} \tag{4.6}$$

Rotate the receiving horn and RHCPSS under test until maximum and minimum S_{21} appear, the axial ratio can be calculated from (4.6) and the ratio of LHCP component to RHCP component can be derived as:

$$\frac{E_{R0}}{E_{L0}} = \frac{|AR| - 1}{|AR| + 1} \tag{4.7}$$

Suppose that the transmission loss of the LHCP component compared to the reduction in the RHCP component, caused by the RHCPSS, is negligible, i.e., $E_{L0} > E_{R0}$ at the receiving side, E_{L0} and E_{R0} can be deduced from the measured maximum and minimum S_{21}.

Remove the RHCPSS, while keeping the shielding plate in place, and then re-perform the S_{21} measurement to figure out the referenced RHCP and LHCP components of the incident wave, so as to obtain the isolation and transmission loss.

Figure 4.6 shows the frequency response of the measured isolation for the realized RHCPSS. The simulation responses for outer radius of 0.1 *mm*, 0.15 *mm* and 0.2 *mm* (arm length *l*= 1.5 *mm*, inner radius= 0.075 *mm*) are also shown for comparison. As the figure indicates, the measured data is quite similar to the simulated result of the case with outer radius of 0.2 *mm*. The maximum measured isolation of 23.89 dB is obtained at 58.4 GHz, while the isolation at 60 GHz is only 7.82 dB. Figure 4.7 illustrates the corresponding transmission losses for measurements and simulations. The minimum transmission loss of about –2.25 dB is measured at 58.4 GHz, while at 60 GHz the transmission loss is –4.65 dB.

It is considered that the deviation between the measured and simulated transmission loss was caused by the variation in loss tangent. In the simulations, the loss tangent of Duroid 5870 was set to 0.0009 in the light of the data provided by the laminate vender. Nevertheless, this value is for 10 GHz, and the loss tangent at 60 GHz must be higher. Another likely reason for this could be the imperfection in workmanship, including the inconsistencies of the thickness of the copper plating for each via and the outer radius of each annular ring pad. Poor conduction of the vias can lead to geometrical resonance phenomenon on the whole structure by undesired CP illumination, causing an increase in the transmission loss.

4.5 Conclusions

This chapter reports theoretical and experimental investigations into a new CPSS. The proposed design is well suited for PCB manufacturing process. The closed-form spectral domain Green's function for this CPSS configuration was first derived and transformed into the periodic Green's function. Then the scattered fields of a planar infinite CPSS were obtained by the induced currents together with the

periodic Green's function. Lastly, with the scattered fields, the isolation and transmission loss can be calculated.

The design of a 60GHz RHCPSS shows good performance, with the respective simulated isolation and transmission loss at 60 GHz being 26.4 dB and –0.43 dB. However, the manufacturer added unprompted pairs of annular ring pads in the fabrication process to avoid any peeling effect. The sizes of the pads are even inconsistent. These variations make the finished RHCPSS disagree with the optimized design.

For the finished RHCPSS, the maximum measured isolation of 23.89 dB and the minimum measured transmission loss of –2.25 dB occur at 58.4 GHz, which is a little lower than the desired frequency. The deformations resulted from fabrication and the defects in workmanship indeed affect the performance. Simulations on various degrees of deformed structures reveal that the isolations are greater than 25 dB while the transmission losses are better than –1 dB. In addition, one of the results quite resembles the measured data. Therefore, as long as the deformations are arranged during the design process, an exceptional outcome can be reached.

With the findings in this chapter, the feasibility of developing a millimeter-wave CPSS with printed circuit technology is confirmed. This study can serve as a foundation for further research, and opens new possibilities for the beneficial application in this field.

References

1. D. G. Berry, R. G. Malech, and W. A. Kennedy, “The reflectarray antenna,” *IEEE Trans. Antennas Propagat.*, vol. 11, pp. 645 - 651, Nov. 1963

2. C-P Chiu; and S-J Chung, “A new millimeter-wave folded microstrip reflectarray antenna with beam steering,” *IEEE AP-S Int. Symp.Digest*, vol. 3, pp. 140 - 143, June 2002

3. W. V. Tilson, T. Tralman, and S. M. Khanna, “A polarization selective surface for circular polarization,” *IEEE AP-S Int. Symp.Digest*, vol. 2, pp. 762 - 765, June 1988.

4. R. Pierrot, “Éléments résonants en polarization circulaire et réflecteur semi-transparent composé de ces éléments,” *French Republic Patent # 89.609*, No. 1.512.598, Dec 30, 1966.

5. G. A. Morin, “A simple circular polarization selective surface,” *IEEE AP-S Int. Symp.Digest*, vol. 1, pp. 100 - 103, May 1990

6. G. Dural, and M. I. Aksun, “Closed-form Green's functions for general sources and stratified media,” *IEEE Trans. Microwave Theory Tech.*, vol. 43, pp. 1545 - 1552, July 1995

7. D. G. Fang, J. J. Yang, and G. Y. Delisle, “Discrete image theory for horizontal electric dipoles in a multilayered medium,” in *Proc. IEE Microwaves Antennas Propagat.*, vol. 135, pp. 297 - 303, Oct. 1988

8. R. M. Shubair, and Y. L. Chow, “A rapidly convergent summation of the periodic Green's function in layered media,” *IEEE AP-S Int. Symp.Digest*, vol. 1, pp. 200 - 203, July 1992

9. M. J. Park, and Sangwook Nam, “Efficient calculation of the Green's function for multilayered planar periodic structures,” *IEEE Trans. Antennas Propagat.*, vol. 46, pp. 1582 - 1583, Oct. 1998

10. http://www.zeland.com/ie3d.html

5 A New Advance in Circular Polarization Selective Surface – A Three Layered CPSS without Vertical Conductive Segments

5.1 Introduction

Linear-polarization selective surfaces in modern reflector antenna design, such as reflectarray antennas [1-4], have been known and used for a long time. Many applications, stemmed from linear polarization (LP) selection could be converted to applications based on circular polarization (CP) selection, e.g., satellite communications, navigation systems, wireless LAN, automotive radar, and remote sensing radar applications. On the other hand, CPSS has been rarely used since no simple electromagnetic surface achieving such a selection is accredited yet.

Conventional circular polarization selective structures comprise transverse metal traces on different layers jointed together with longitudinal conductive filaments. Two typical designs are shown in Figure 5.1. Besides, assemble two or more CP polarizers or LP-CP converters [5] with specified separations and orientations could achieve the same circular polarization selectivity function.

The initial concept was introduced in [6], which proposed a CPSS formed by a two-dimensional array. Each array element consisted of two orthogonal and resonant dipoles, separated by a free-space quarter wavelength in height; with their center feed points connected together by a half-wavelength transmission line, as shown in Figure 5.1(a).

The above design is intuitive, but there exist problems in practice. The main

difficulty is that the geometry and the medium of the transmission line must be properly designed to make the separation of the two dipoles a quarter wavelength and the electrical length a half wavelength simultaneously. In addition, considerations must be taken to maintain impedance matching between the dipoles and the transmission line. Thus realizing this structure for use at high frequencies is not easy. As a result of the complexity, another design with an analogous concept but simpler structure was discovered [7].

The second design is a bent wire formed from three jointed orthogonal segments, having a total length of about one wavelength, as shown in Figure 5.1(b). The transmission line has been replaced with a direct wire segment, maintaining a vertical distance of a quarter wavelength, but the electrical length is no longer a consideration. The two transverse straight wires, connected by the upright segment, are approximately three-eighths wavelength and pointed in perpendicular directions. This structure can be fabricated in a laminate by using printed circuit technology: the two transverse wires are created by two metal traces and the vertical segment is accomplished by a conductive via.

For the CP wave illuminated at normal incidence that makes the respective induced currents on the two transverse wires in-phase, the two wires behave like dipoles with sinusoidal-like current distribution on them, and a null appears at the middle of the vertical segment. The entire bent wire thus operates at geometrical resonance, and the dipoles re-radiate waves in both the +z and –z directions. Below the substrate, the scattered wave propagates in the –z direction, meanwhile above the substrate, the incident and scattered wave add 180o out of phase, thus producing a null field in that region.

(a)

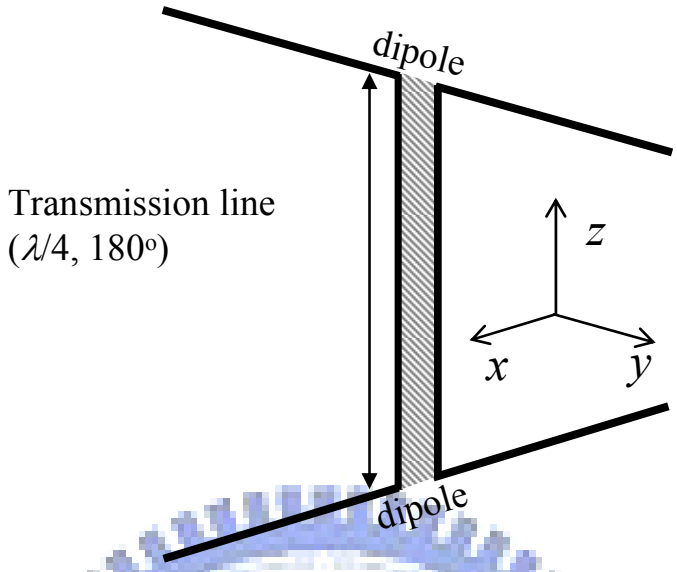

(b)

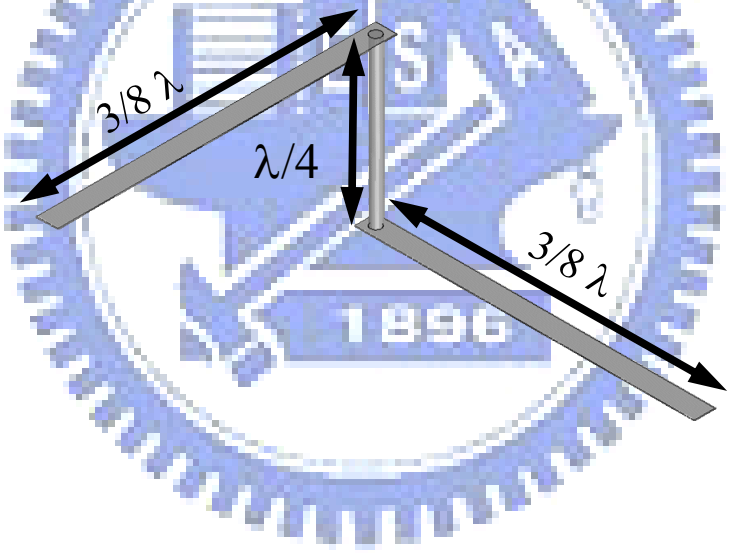

Figure 5.1 (a) The constituent element of the CPSS structure proposed in [6]. (b) The constituent element of the CPSS structure proposed in [7].

For the other CP illumination, the induced currents on the two transverse wires are 180^{o} out of phase, and tend to cancel each other out. The current distribution is much lower and no longer sinusoidal-like, and the scattered wave is thus much weaker. The reflected wave in this case is negligible and the incident wave in the transmission region is scarcely disturbed.

Although the second design is much simpler than the first one, implementing numerous, dense and thin vias on a CPSS accurately and stably is still hard to achieve at high frequencies. In printed circuit fabrication process, a vertical connection between layers is achieved by a via hole with copper plating on the walls and two annular ring pads encompassing the hole on each side of the substrate in order to avoid a peeling effect. The thickness of the copper plating for each via is usually inconsistent and will deteriorate the effectiveness of CP wave selectivity. Furthermore, poor conduction of the vias can lead to geometrical resonance phenomenon on the whole structures by undesired CP illumination, causing an increase in transmission loss.

To avoid the problems associated with the vertical conductive segments and increase flexibility in design motivated the drive to invent a new type of CPSSs that is composed of only transverse elements but no vias. Blocking electromagnetic waves at any designated frequency with two perpendicularly directed, adequately tuned dipoles which are placed a quarter wavelength apart is easy to do, but, if without the vias, both senses of CP wave will cause resonance on the two dipoles. In other words, the blocking effect works equally well for both RHCP and LHCP, and the inherency of CP wave selectivity is nonexistent.

In order to retain the capability of discriminating different CP waves, a substitute which is more suitable to multi-layered PCB process is created in the midst

of the two dipoles to take the place of the via. Connection would then be established through the couplings caused by the intermediate part between the two dipoles, so that each sense of circular polarization gives a different response. We construct the operational principle for this type of CPSSs, as described in Section 5.2.

With the similarity of LHCPSS and RHCPSS, only the LHCPSS will be covered in this work. Many simulations were performed using the commercial software HFSS [8]. From these simulations, the optimal parameters were obtained and a 30 GHz LHCPSS was designed and constructed. Lastly, the calculated and measured results are presented.

5.2 Principle

According to the fabrication capability provided by PCB manufacturers, both the minimum achievable trace width and spacing are 4 *mils*. In this work, all trace widths and spacing are set to 0.1 *mm* (≈4 *mils*).

There are many commercially available, off-the-shelf products, which are suitable for the development of CPSSs. The selection of an appropriate laminate depends on the dielectric constant and the thickness of the substrate. A substrate with a dielectric constant of 2.33 and 62-*mil* thickness was chosen for this work, because it has the lowest error (<5%) at the designated frequency of 30 GHz.

For this chapter, the term “Isolation” is defined as the amount of the designated polarization field blocked by the surface. The “Isolation” for a LHCPSS is found by applying a LHCP plane wave illumination, then measuring the difference of the LHCP field intensity received with and without the LHCPSS inserted in front of the receiver. On the other hand, the “Transmission Loss” is found by measuring the difference of the RHCP field received with and without the LHCPSS inserted, with an input RHCP

plane wave illumination.

The CPSSs presented in this chapter, are arrays composed of identical cells made on dielectric slabs, with appropriate periodicities between cells. HFSS was employed to analyze the reflections and transmissions of the CPSSs. Perfectly matched layers (PMLs) were used to simulate an unbounded radiation environment. Periodic boundary conditions were applied to reduce the problem domain; consequently adopting only one unit cell for simulation is sufficient.

Figure 5.2 illustrates a unit cell of a two-dimensional array, which contains two perpendicular dipoles located respectively on the top and bottom layers of a 62-*mil* Duroid 5870 laminate, with an L-shaped trace between the dipoles. The periodic boundary conditions are applied on the four sidewalls of the cell, and the other two sides are attached with PMLs.

Consider if only the y-directed trace (lower dipole) existed in a unit cell (refer to Figure 5.2), and illuminate the array with a normally incident (+z) y-polarized LP plane waves. The frequency response of isolation varies with the length of the dipole and the periodicity.

(a)

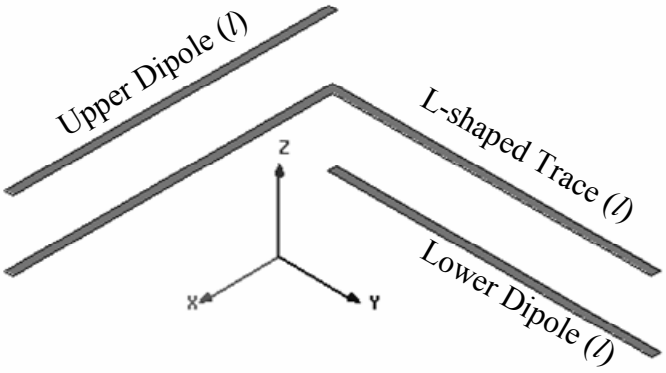

(b)

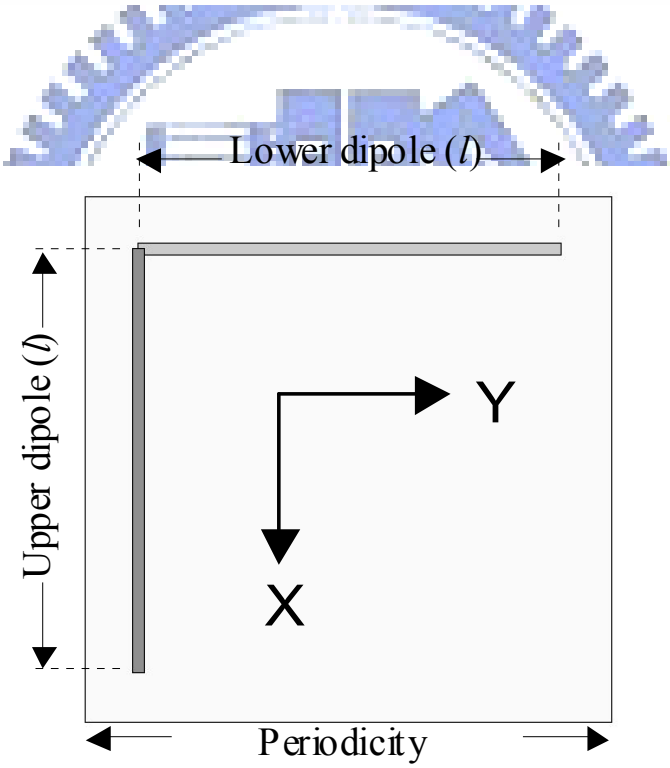

Figure 5.2 (a) The unit cell of a CPSS that contains two perpendicular dipoles on top and bottom layers and an L-shaped trace in the middle. (b) Top view of the unit cell.

A maximum isolation of 20.76 dB at 30 GHz is found when *l*= 3.61 *mm* (about a half wavelength) with periodicity= 4.5 *mm*. The isolations for x-polarized incident plan wave are around 0.75 dB over the frequency range of 25-35 GHz, which can be regarded as the transmission losses in the substrate.

If the unit cell contains both upper and lower dipole, and the dipole lengths and periodicity remain the same, the simulated isolations as a function of frequency for respective LHCP and RHCP incidence are shown in Figure 5.3. It confirms that a configuration with two perpendicularly directed dipoles separate one-quarter wavelength apart has almost the same blocking responses to LHCP and RHCP incidences. Also noted, was that the frequency the maximum isolation (21.5 dB) for a CP incidence occurred at, is a little higher than that for a LP incidence (30 GHz).

As stated in Section 5.1, some coupling elements are needed to relate the upper and the lower dipole in such a way, that the whole structure exhibits CP wave selective property. An L-shaped trace was thus contrived as the coupling element, to be inserted into the middle of the two dipoles (Figure 5.2). The dipole lengths and periodicity were kept unchanged. Each arm of the L-shaped trace has the same length as the dipoles and is parallel to the upper and the lower dipole respectively.

With the addition of the L-shaped trace, the electromagnetic coupling effect generated causes the total effective currents on the upper and lower dipole to be primarily the vector sum of the currents as expressed in the following equations:

$$I_u = I_{uu} + I_{ul} = I_{uu} + CF_{ul} \cdot I_{ll} \tag{5.1}$$

$$I_l = I_{ll} + I_{lu} = I_{ll} + CF_{lu} \cdot I_{uu} \tag{5.2}$$

where I_u is the current on the upper dipole, I_l is the current on the lower dipole, I_{uu} is the current on the upper dipole induced by the x-component of the incident wave, I_{ll} is

the current on the lower dipole induced by the y-component of the incident wave, I_{ul} is the current on the upper dipole coupled from the current on the lower dipole induced by the y-component of the incident wave, I_{lu} is the current on the lower dipole coupled from the current on the upper dipole induced by the x-component of the incident wave, and CF_{ul} and CF_{lu} are the coupling factors.

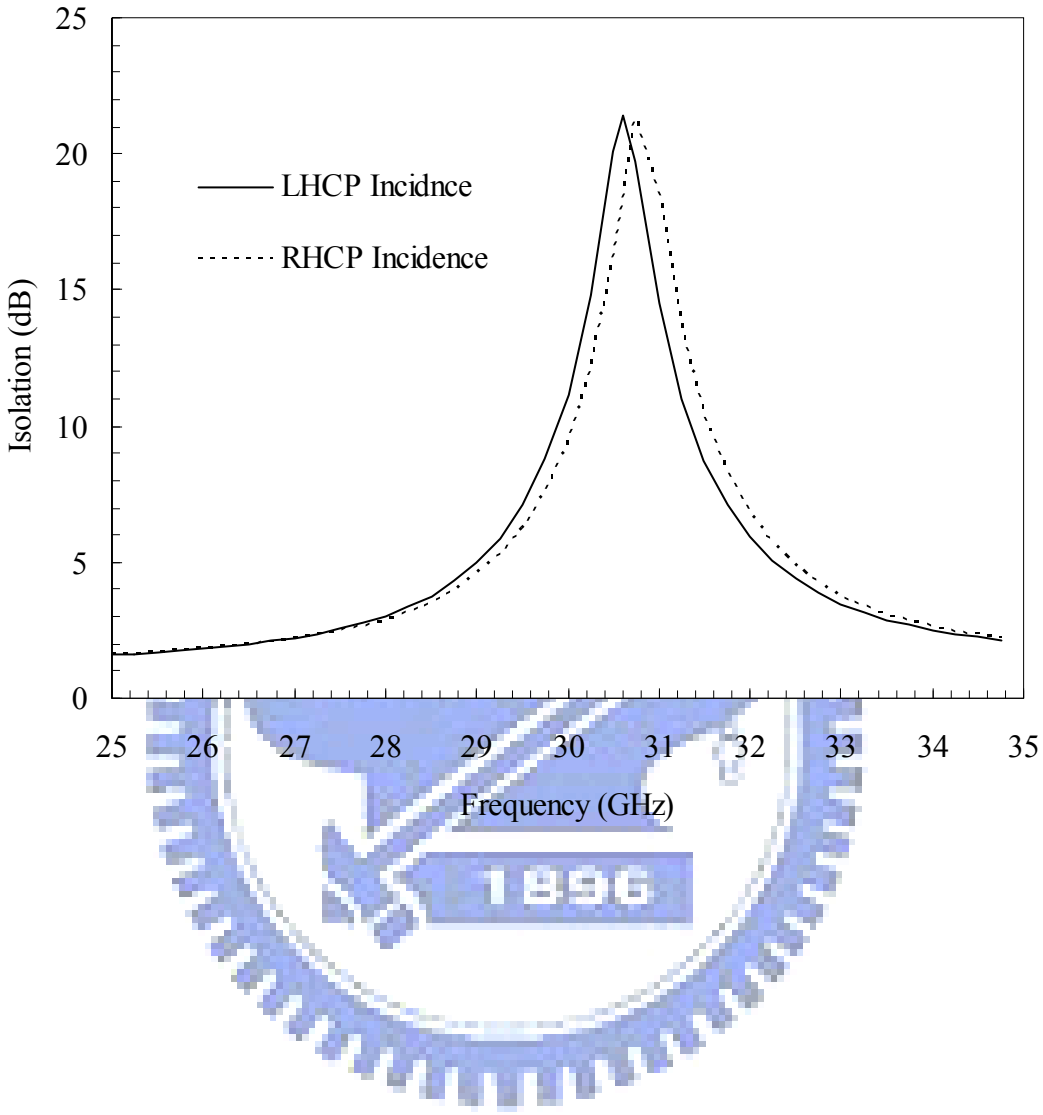

Figure 5.3 Isolations as a function of frequency for a unit cell with two perpendicular dipoles located respectively on top and bottom layer of a 62-*mil* Duroid 5870 laminate (*l*=3.61 *mm*, periodicity= 4.5 *mm*).

CF_{ul} is defined as the ratio of the magnitudes, of the currents on the upper dipole, with respect to the magnitudes of the currents on the lower dipole, when excited by a y-polarized plane wave; whereas CF_{lu} is the ratio of the magnitudes, of the currents on the lower dipole, with respect to the magnitudes of the currents on the upper dipole, when excited by an x-polarized plane wave. The simulated coupling factors for various frequencies are shown in Figure 5.4. It was discovered that CF_{ul} is very close to CF_{lu}, and the maximum coupling factor of about 0.92 occurs at 27 GHz. The directions of the current for the upper and the lower dipoles excited by LHCP and RHCP incidences at this frequency are indicated in Figure 5.5, and the directions of the current on the upper and the lower dipoles excited by x- and y-polarized plane waves respectively are indicated in Figure 5.6.

For a 27 GHz LHCP illumination, I_{ll} and I_{lu} are in the same direction, and I_{uu} and I_{ul} are also in the same direction. Therefore, by (5.1) and (5.2), the currents on both dipoles add constructively. The geometrical resonance remains on the dipoles, so that a LHCP wave is reflected.

On the contrary, for a 27 GHz RHCP illumination, I_{lu} and I_{ll} are approximative in magnitude but opposite in direction, as are I_{ul} and I_{uu}. The mutual interactions make the currents on the dipoles nearly cancelled out, allowing the incident RHCP wave to pass through this type of CPSSs with only a slight influence as a result of the much-reduced scattered fields ascribed to the L-shaped trace.

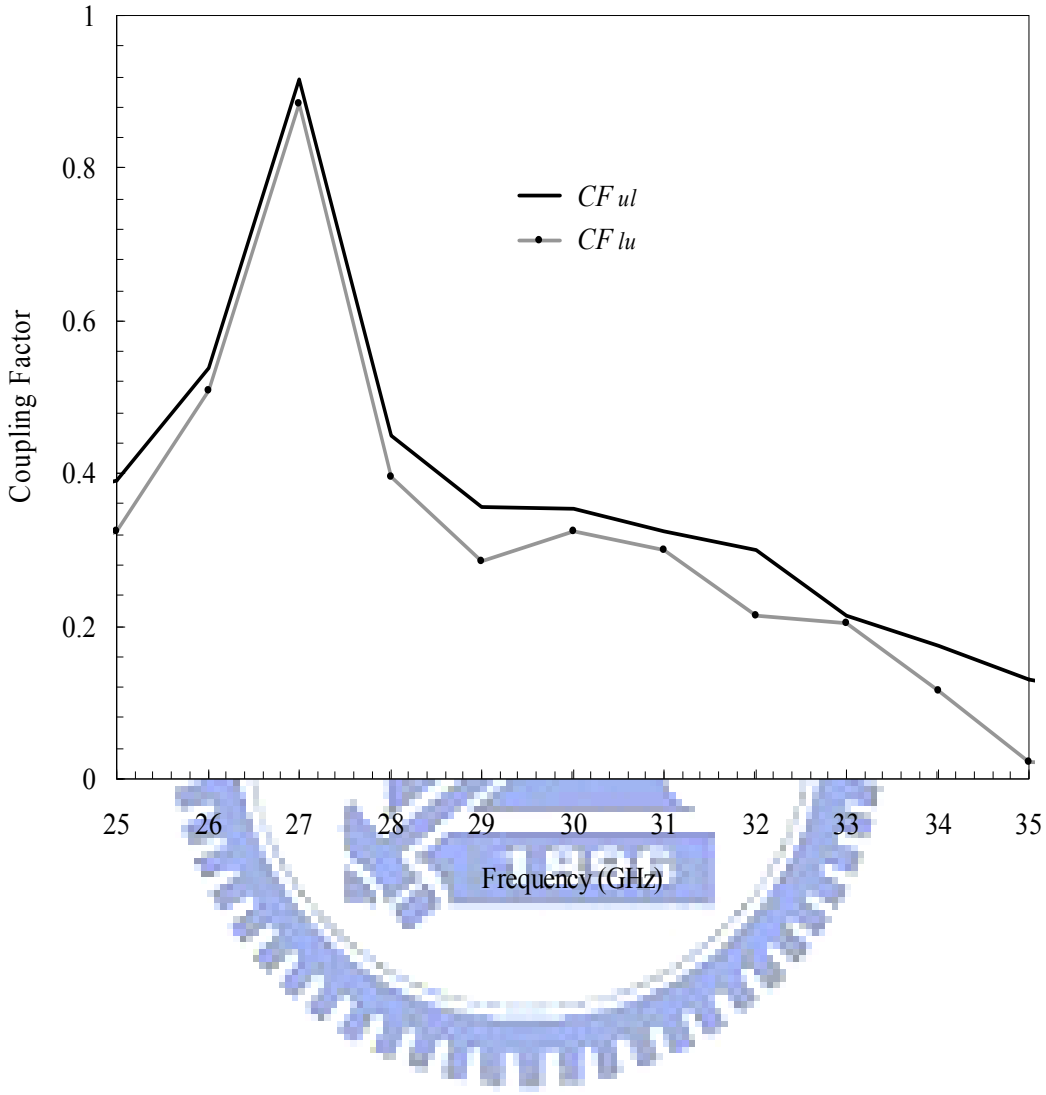

Figure 5.4 Coupling factors as a function of frequency for the configuration shown in Figure 5.2 (l=3.61 *mm*. Periodicity= 4.5 *mm*).

(a)

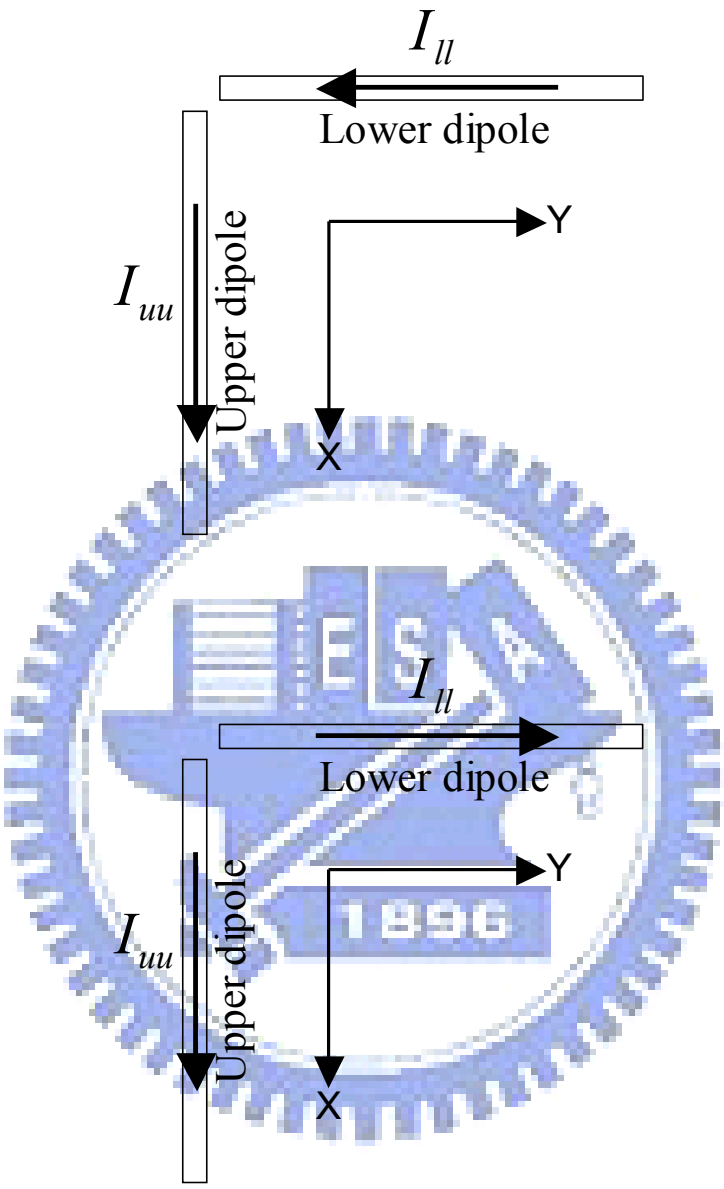

Figure 5.5 The current directions on the upper and the lower dipoles excited by (a) LHCP incidence, and (b) RHCP incidence, at 27 GHz.

(a)

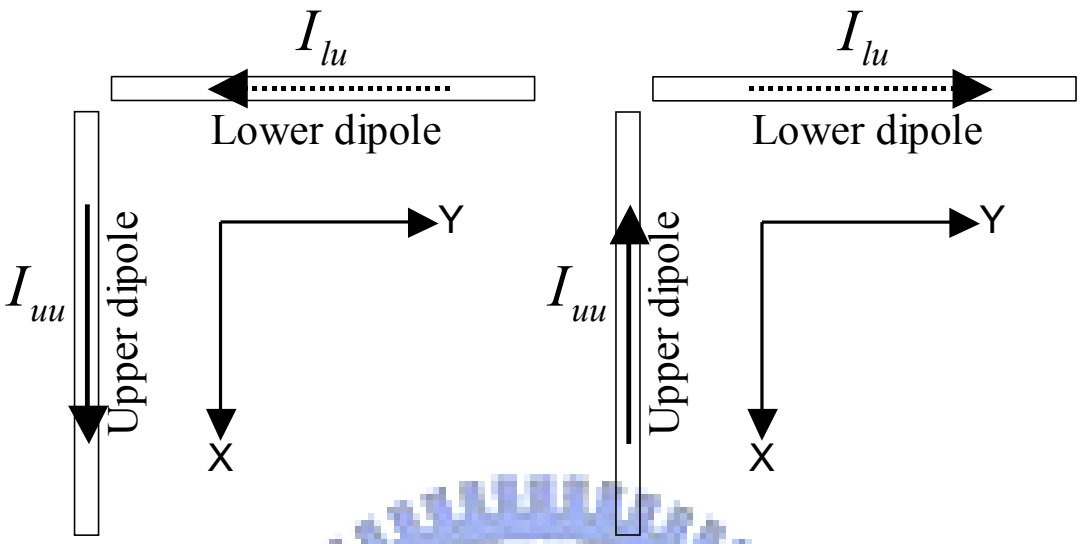

(b)

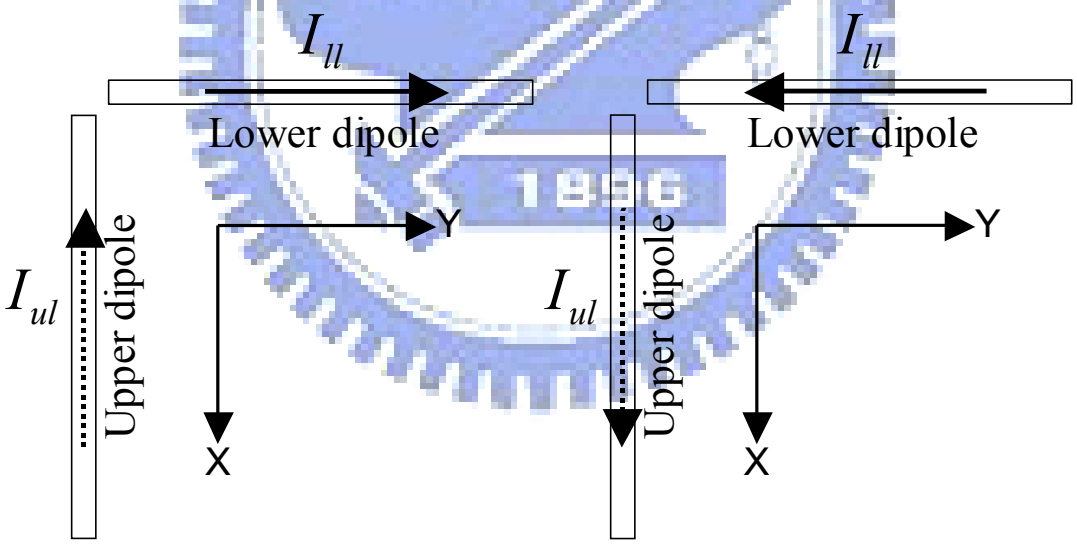

Figure 5.6 The current directions on the upper and the lower dipoles exited by (a) 27 GHz x-polarized plane waves, and (b) 27 GHz y-polarized plane waves. The dashed line indicates the couple currents.

The simulated isolations as a function of frequency for LHCP and RHCP incidences are shown in Figure 5.7. The results reveal that the isolation curves for LHCP and RHCP are no longer similar, as compared with Figure 5.3. At 27 GHz, a sudden rise in LHCP isolation curve can be seen, but the isolation slightly declines for RHCP incidence, as expected. Consequently, it is reasonable to conclude that the coupling effect generated by the presence of the L-shaped trace in between the upper and lower dipole markedly affects the circular polarization selectivity performance of a CPSS structure.

Further investigations on the L-shaped trace were performed to better understand its property. Simulated results show that when the length of the L-shaped trace gets longer, the maximum coupling factor shifts towards lower frequency. Therefore, the lengths of the arms of the L-shaped trace should be slightly shorter than the lengths of the dipoles in order to have a higher isolation for LHCP incidence and a lower transmission loss for RHCP incidence at the desired frequency.

5.3 Design

With the function of the L-shaped trace confirmed, we added two auxiliary L-shaped traces in order to enhance the coupling effect and increase degrees of freedom in designing. The additional L-shaped traces are also in the middle layer but placed on either side of the original L-shaped trace. The lengths of the two additional traces are variables, independent of the length of the central L-shaped trace. Being a three-layered structure, two 31-*mil* Duroid 5870 laminates are utilized to develop the LHCPSS, and the L-shaped traces are implemented on the bottom side of the upper laminate. A coat of agglutinate substance binds the laminates together, with a minimum achievable thickness of the agglutinate substance being 2 *mils*.

Initially, the agglutinate substance is assumed to be made of the same material as the substrates (Duroid 5870) above and below. The whole configuration is illustrated in Figure 5.8(a).

Preliminary simulations show that the two additional L-shaped traces, in contrast to the original one, have minor contribution in reducing the RHCP induced currents on the upper and the lower dipoles. Furthermore, no significant improvements were obtained by having unmatched endpoints, or end-edges of the two additional L-shaped traces which are not in same straight lines. Therefore, to decrease the calculation amount, all simulations will be performed with the two additional L-shaped traces having matching endpoints. The geometry variables used for optimization are indicated in Figure 5.8(b).

The performance of the circular polarization selectivity is extremely sensitive to the lengths of the traces; especially the lengths of the two dipoles. The lengths of the dipoles on the top and bottom layers primarily determine the LHCP isolation of a LHCPSS, while the well-tuned L-shaped traces in the middle layer would reduce the RHCP transmission loss. The periodicity of the array has an analogous effects on both the isolation and transmission loss; the larger the periodicity, the less the isolation and transmission loss.

The optimization process starts by first assuming that the lengths of the two dipoles are a half wavelength in the substrate, without any other metallic traces. With this design, excellent isolations (e.g. beyond 40 dB by simulation) can be achieved by varying the dipole lengths, however, high transmission losses accompanies. Next, the three L-shaped traces are taken into account, and lastly the periodicity of the array is included. With the combination of these, we have a total of four degrees of freedom available for optimization; they are the lengths of the

metallic traces (l, l_1 and l_3) as well as the periodicity of the array (p), provided that $l_2 = l_3 + 0.4$ *mm* (see Figure 5.8). All of the geometry variables affect the result, so for the optimum solution, all four variables must be adjusted simultaneously.

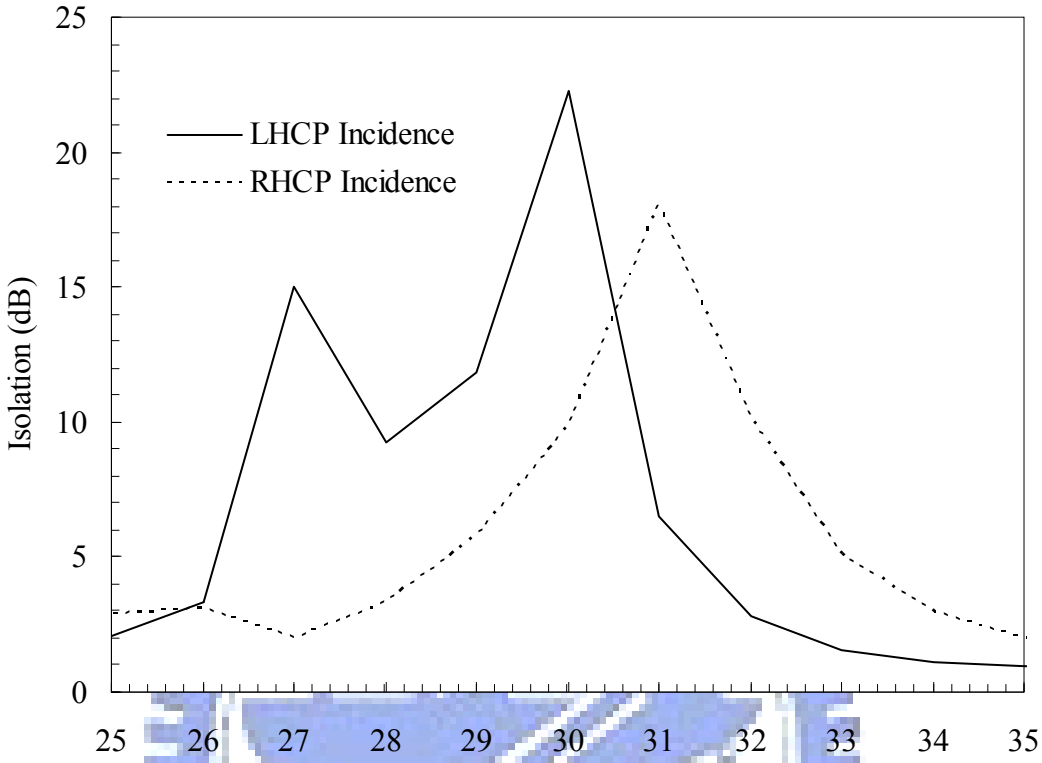

Figure 5.7 The simulated isolations as a function of frequency for the configuration shown in Figure 5.2 (l= 3.61 *mm*, periodicity= 4.5 *mm*).

(a)

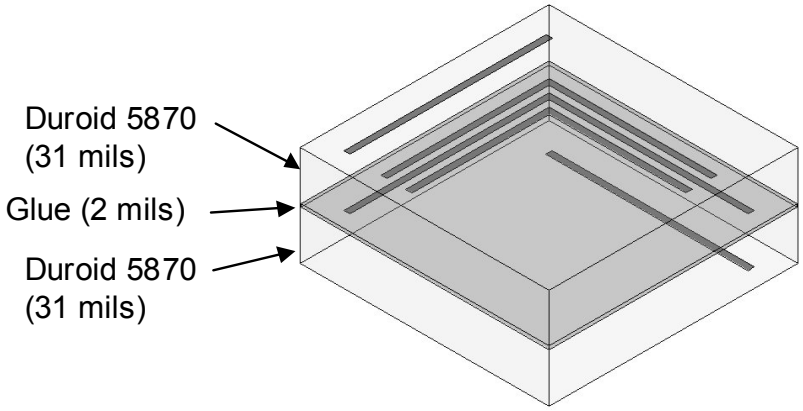

(b)

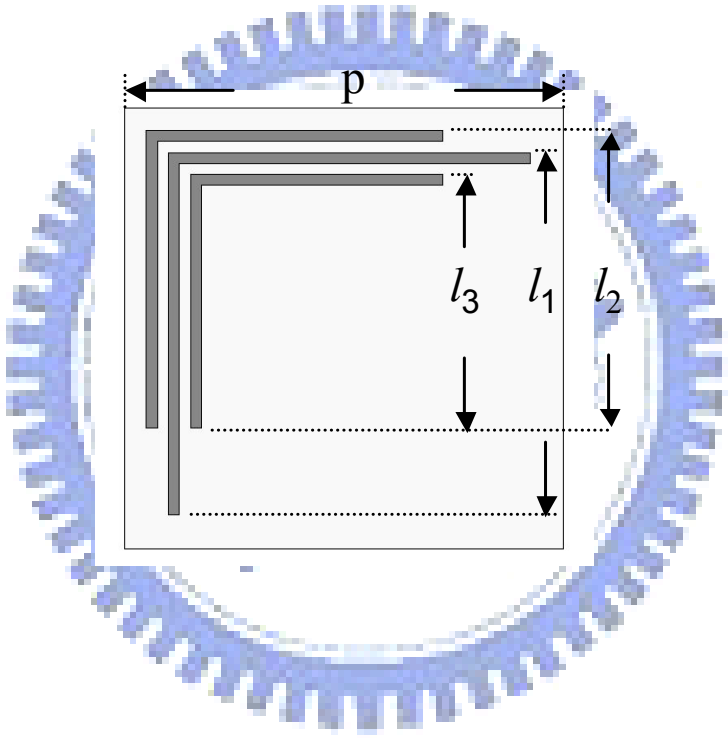

Figure 5.8 (a) The schema of the proposed LHCPSS configuration. (b) Top view of a unit cell of the LHCPSS, three L-shaped traces are implemented in the middle layer.

Then, find the geometry which gives good isolation and acceptable transmission loss. The geometry parameters obtained are: p = 4 *mm*, l = 3.25 *mm*, l_1 = 3.295 *mm*, l_2 = 2.7 *mm* and l_3= 2.3 *mm*. The resultant isolation is 19.83 dB and the transmission loss is about –2.55 dB. Note that l_1 is a little longer than l, which violates the inferences we drew in Section 5.2. The geometry does not have to be the perfect, because the glue is not made of Duroid 5870 material in reality, it is merely treated as an initial step to be followed up with optimizations.

For the purpose of examining the effects of the glue, simulations were done with the geometry unchanged, but replacing the glue layer with different materials. As Figure 5.9 and Figure 5.10 indicate, the isolation is a rapidly varying function of ε_r, while the transmission loss is a slowly varying one. ε_r = 2.33 is the special case where the agglutinate substance is of the same material as the substrates. The performance of the design is considerably susceptible to the agglutinate substance. Therefore the geometry should be redesigned to overcome the influence brought about by the glue.

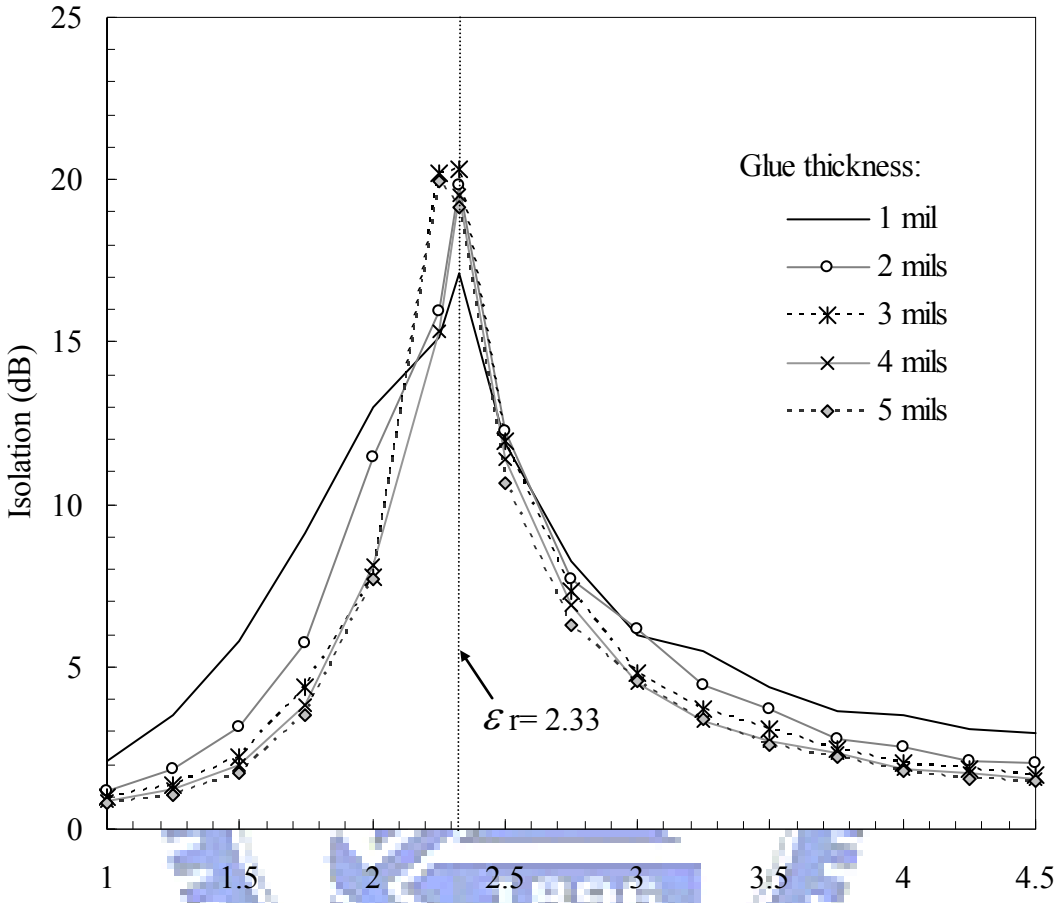

Figure 5.9 Isolations at 30 GHz for various ε_r and thicknesses of the glue layer (p = 4 *mm*, *l*= 3.25 *mm*, l_1= 3.295 *mm*, l_2= 2.7 *mm* and l_3= 2.3 *mm*).

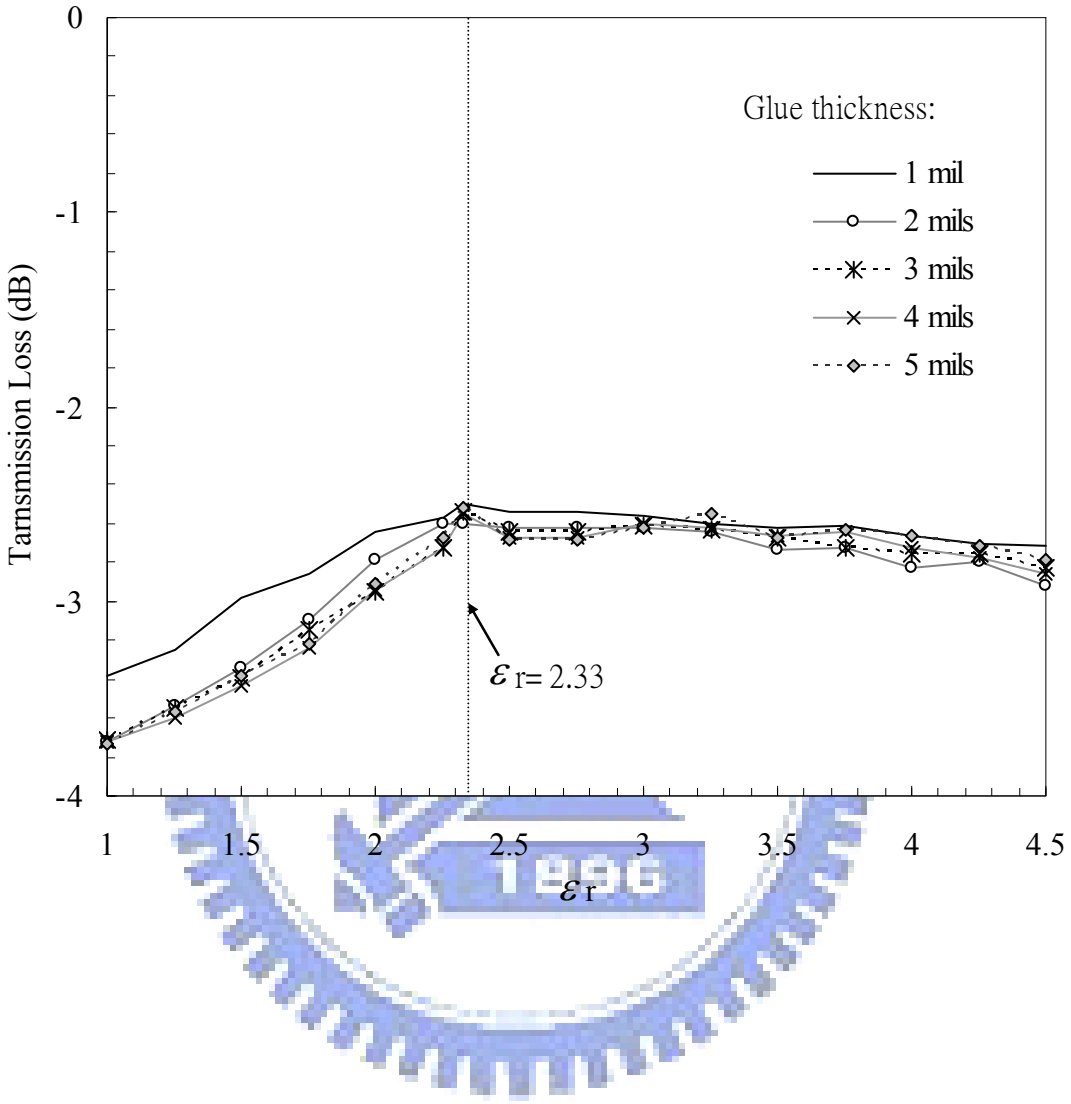

Figure 5.10 Transmission losses at 30 GHz for various ε_r and thicknesses of the glue layer (p = 4 *mm*, *l*= 3.25 *mm*, l_1= 3.295 *mm*, l_2= 2.7 *mm* and l_3= 2.3 *mm*).

Also of interests, is to vary the glue thicknesses to investigate its interaction, because the glue thickness is hard to control. In Figure 5.9 and Figure 5.10, isolations and transmission losses for different glue thicknesses shows little change. This signifies that the height of the configuration is less important as a factor; the spacing between the upper and the lower dipole do not affect the performance much with this design.

FR-4 (ε_r = 4.5) is the most commonly used agglutinate substance by manufacturers to glue printed circuit boards together. Under this condition, achieving optimal geometries are not convenient because the agglutinate substance is different from the substrates of the laminates. The discontinuities caused by different materials lead to additional reflections. Figure 5.9 shows the isolations for the initial design with ε_r = 4.5 glue, fall to less than 5 dB.

If there is no metal trace or dipole, i.e. only substrates and glue layer exist, the transmission losses for the same ranges of ε_r and glue thicknesses as in Figure 5.10 are between –0.64 dB and –0.95 dB. The transmission loss for a 2-*mil* FR-4 glue layer is about –0.86 dB, which can be explained as the loss caused by the substrates and glue layer.

The optimization procedure described above is resumed to find the proper geometry parameters of the present configuration with a 2-*mil* FR-4 glue layer. By iteratively adjusting l_1 and l_3 together with p for various dipole lengths (l), and then sifting out the cases with high isolation and low transmission loss, the appropriate solutions can be extracted. Some of the selected results are shown in Figure 5.11.

(a)

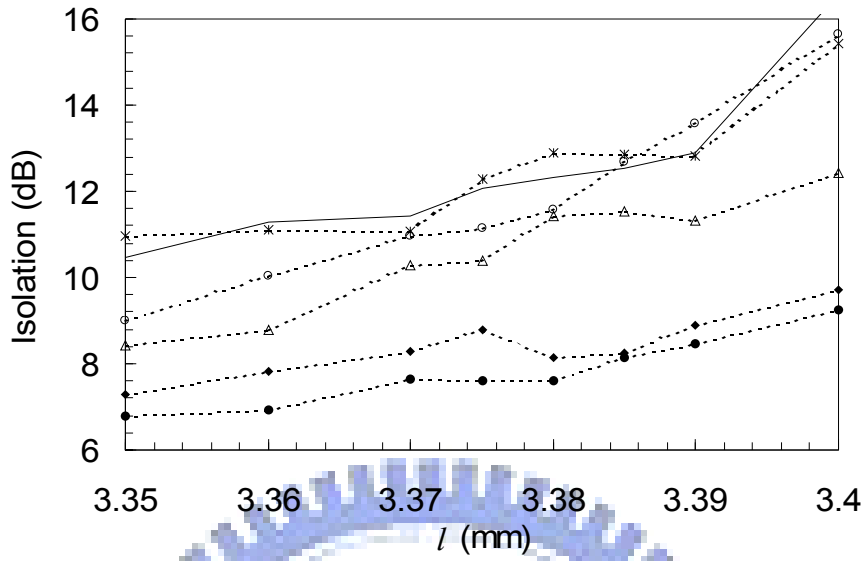

(b)

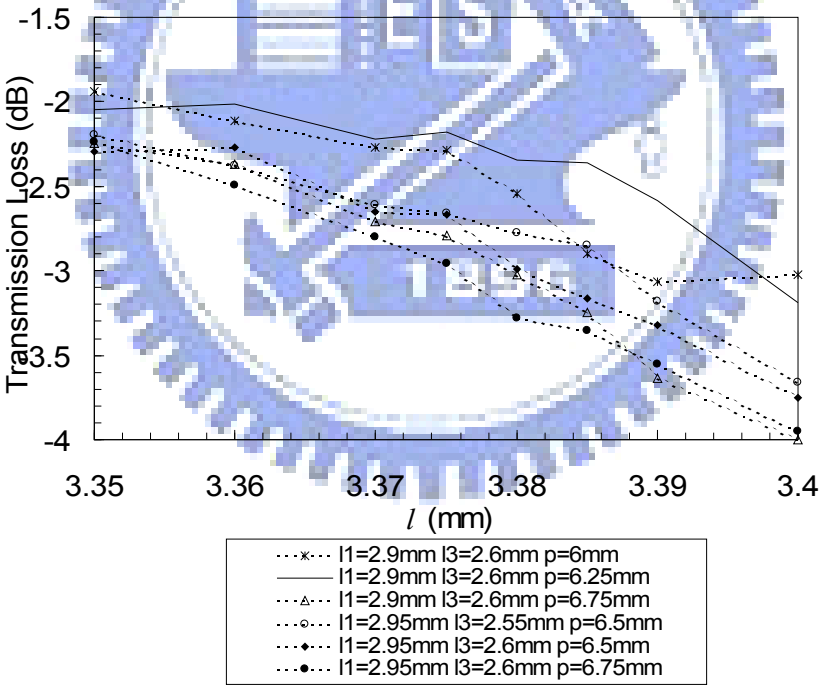

Figure 5.11 (a) Simulated isolations for several geometrical variables (l_1, l_3, p) with respect to l. (b) Simulated transmission losses for several geometrical variables (l_1, l_3, p) with respect to l.

Trade-offs will have to be made, to give consideration to both, low transmission loss and high isolation. The criterion used to judge the optimized geometry is for a case that has the highest isolation with a transmission loss of no worse than –2.5 dB. The final parameters are determined as follows: p = 6.25 *mm*, l = 3.385 *mm*, l_1 = 2.9 *mm*, l_2 = 3.0 *mm* and l_3 = 2.6 *mm*. Consequently, LHCP isolation and RHCP transmission loss for the proposed structure at 30 GHz are 12.52 dB and –2.36 dB respectively.

Figure 5.12 illustrates the normalized induced current distributions, on the optimized LHCPSS for LHCP and RHCP emanations respectively. As can be seen, the current for the LHCP wave is much higher and appears as a resonant distribution, while the RHCP wave exhibits much less current and very little resonance.

5.4 Measurement

Figure 5.13 is the finished LHCPSS with 185 unit elements, made on a disk-shape substrate, with a radius of about 55 *mm*.

Measurements are performed with an Agilent 8510C vector network analyzer. Due to the lack of standard CP horn antenna, two standard LP horn antennas are installed on the two ends of the network analyzer. The cross-polarization levels of the LP horns are less than –40 dB, whose effects are neglected in the following analysis. These two horns are collimated and aligned with each other, as sketched in Figure 5.14. For shielding, a metal plate with a hole having the same radius as the CPSS is placed in between the two horns. The LHCPSS under test is installed in place of the hole. Phase compensation was not taken into consideration in designing, so the distances between the LHCPSS and the two horns must be large enough to ensure the phase of the wave to be uniformly distributed over the aperture of the

LHCPSS. In the measurement setup of this work, the distances are set to 60 cm. Figure 5.15 is the picture taken during measurements.

(a)

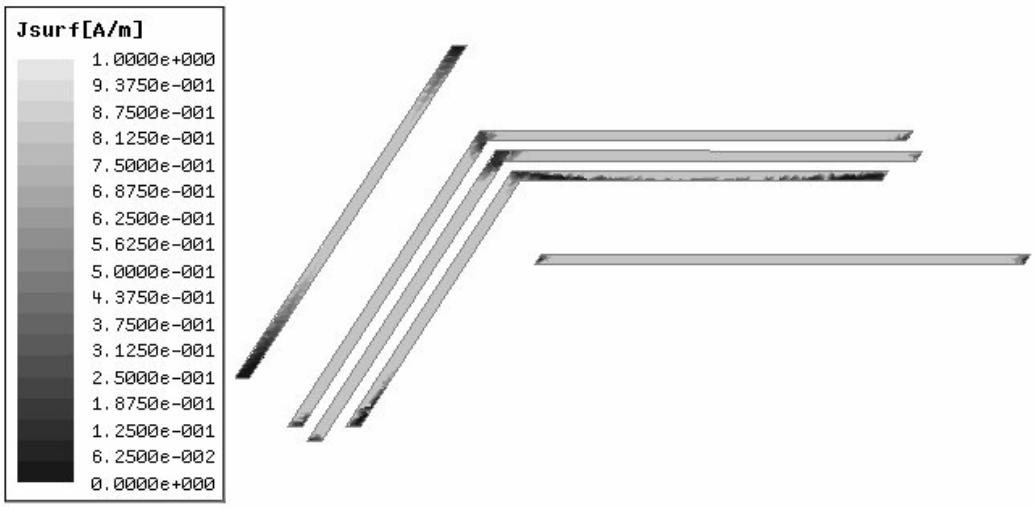

(b)

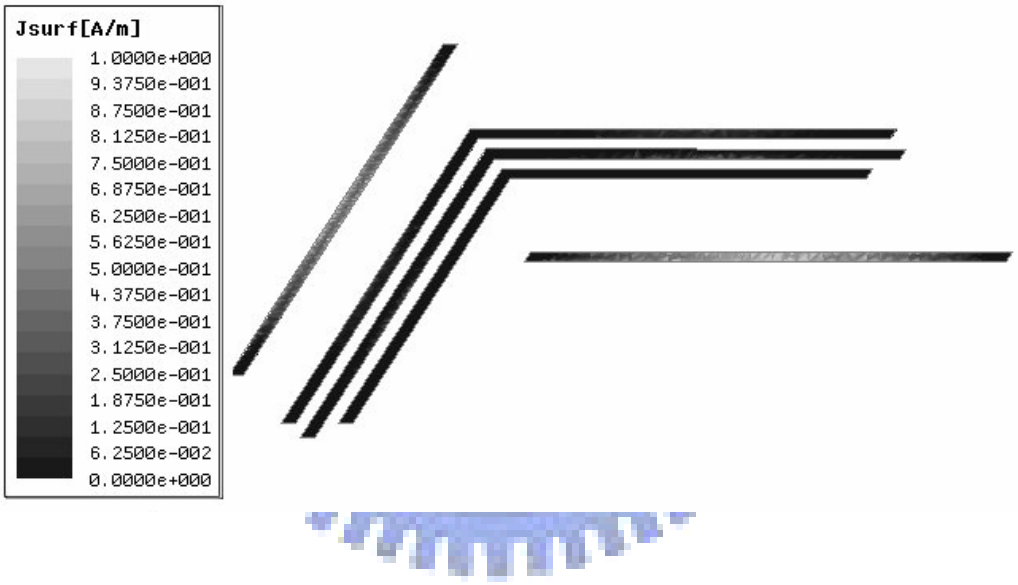

Figure 5.12 (a) Normalized induced current on the metallic traces of the optimized LHCPSS illuminated with (a) LHCP wave, (b) RHCP wave.

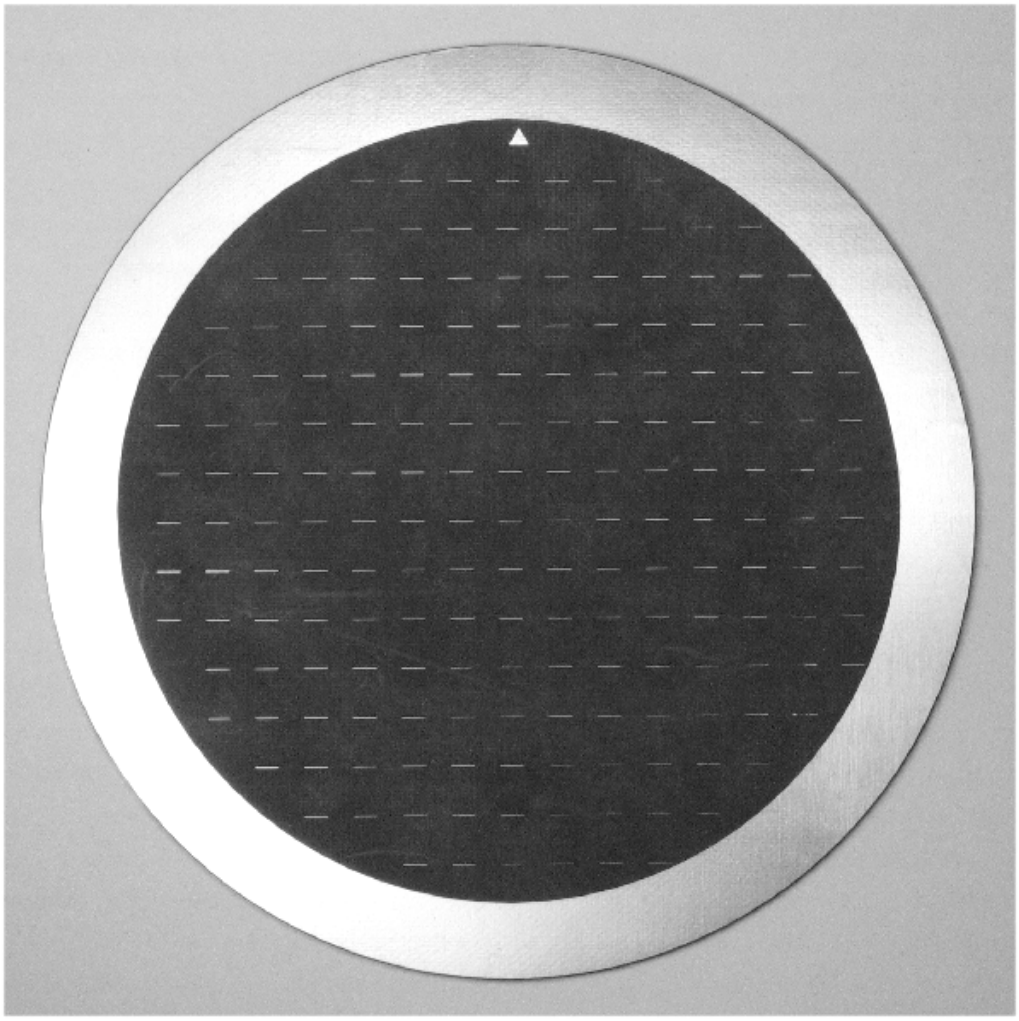

Figure 5.13 Photograph of the finished LHCPSS, with 185 elements on a disk-shape substrate. The radius of the disk is about 55 *mm*.

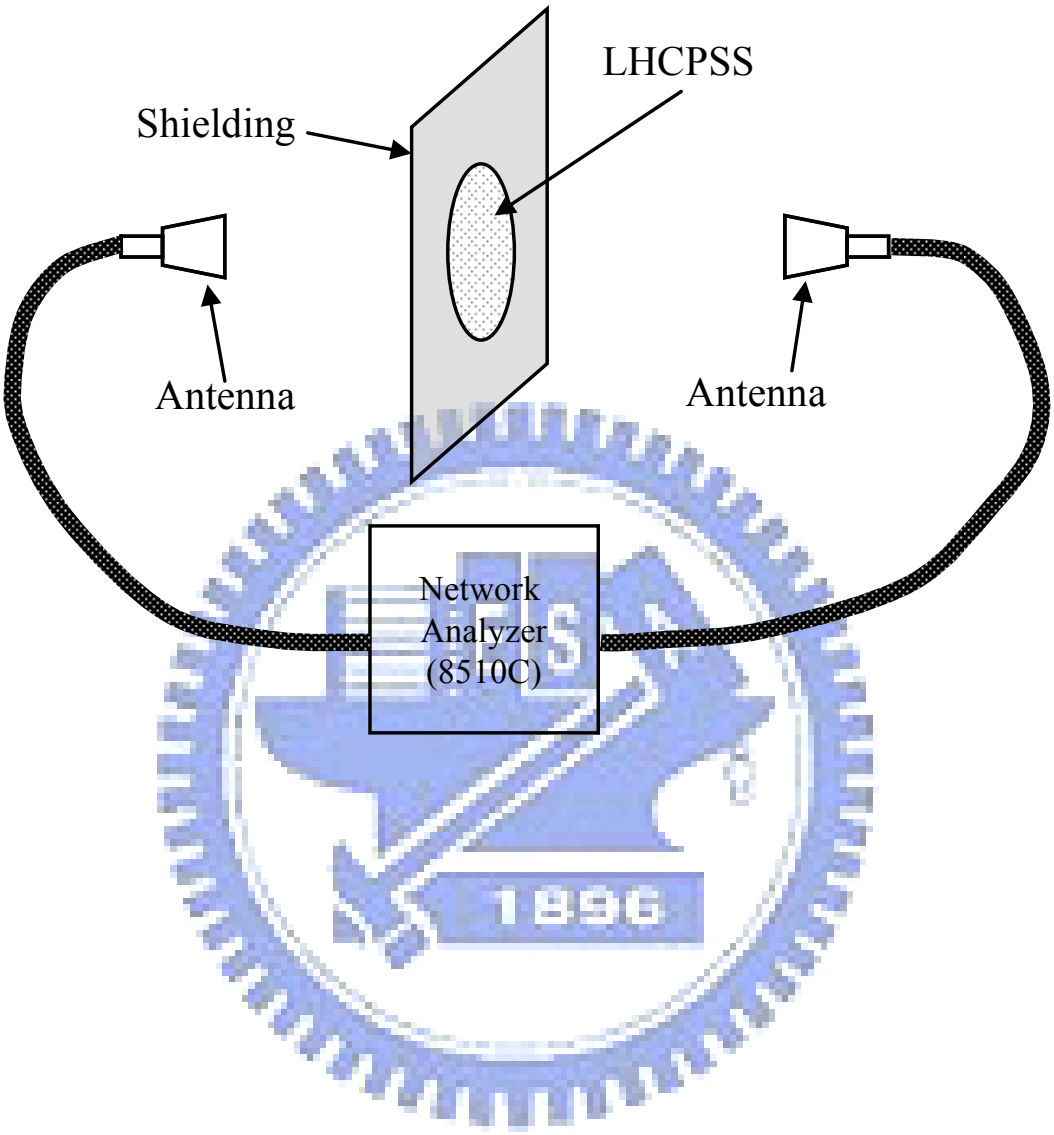

Figure 5.14 Schematic of the measurement setup.

Let E_{Major} and E_{Minor} be the electric field magnitudes in respective major and minor axis of the polarization ellipse of a CP wave:

$$E_{Major} = \frac{E_{R0} + E_{L0}}{2} \tag{5.3}$$

$$E_{Minor} = \frac{E_{R0} - E_{L0}}{2} \tag{5.4}$$

where E_{L0} and E_{R0} denote the intensities of left- and right-hand components respectively.

By definition, the axial ratio (AR) of a CP wave is:

$$|AR| = \frac{E_{Major}}{E_{Minor}} = \frac{E_{R0} + E_{L0}}{E_{R0} - E_{L0}} = \frac{1 + (E_{L0} / E_{R0})}{1 - (E_{L0} / E_{R0})} \tag{5.5}$$

Rotate the receiving horn and the LHCPSS under test until maximum and minimum S_{21} appear, the axial ratio can be calculated from (5.5) and E_{L0}/E_{R0} can be derived from:

$$\frac{E_{L0}}{E_{R0}} = \frac{|AR| - 1}{|AR| + 1} \tag{5.6}$$

Suppose that the transmission loss of the RHCP component compared to the reduction in the LHCP component, caused by the LHCPSS, is negligible, i.e., $E_{R0} > E_{L0}$ at the receiving side, E_{L0} and E_{R0} can be deduced from the measured maximum and minimum S_{21}.

Remove the LHCPSS, while keeping the shielding plate in place, re-perform the S_{21} measurement to figure out the referenced LHCP and RHCP components of the incident wave, and then follow the definitions described in Section 5.2, the isolation and transmission loss can be obtained.

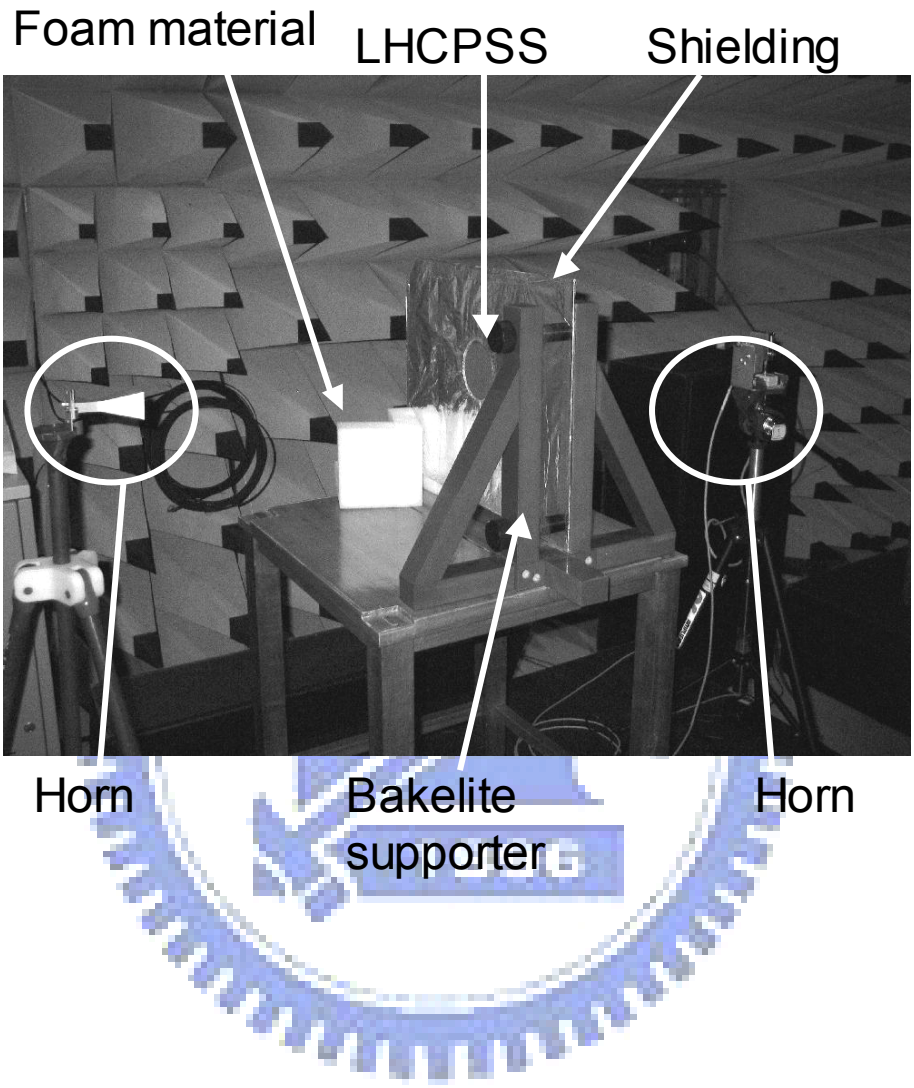

Figure 5.15 Picture taken during measurements. Two LP horn antennas are placed about 60 *cm* apart, and the LHCPSS under test is put in the midst of them.

Figure 5.16 shows the frequency response of the measured isolation for the realized LHCPSS. The simulated response is also shown for comparison. The figure indicates that the measured data is very similar to the simulated one. The maximum measured isolation of 13.78 dB was obtained at 30.2 GHz, and the maximum simulated isolation of about 16 dB occurred at 30.25 GHz. The isolation measured at 30 GHz is 13.12 dB, while the simulated one is 12.52 dB.

Figure 5.17 illustrates the corresponding transmission losses for the measurements and simulations. The transmission loss of the realized LHCPSS also closely resembles that of the simulated one. Transmission loss of about –2.28 dB was measured at 30 GHz, while the simulated one is –2.36 dB. It is reminded that the loss caused by the substrates and glue layer of about –0.86 dB has been included in the transmission loss, as was mentioned in Section 5.3.

The designing of a LHCPSS with better transmission loss would be possible at the target frequency of 30 GHz, but it would have come at the expense of a better isolation.

Compared Figure 5.9 with Figure 5.16, it is obvious that the isolation at 30 GHz for 2-*mil* FR-4 glue has been enhanced, although less when compared to the isolation with Duroid 5870 as the agglutinate substance. In summary, it clearly demonstrates that improvements with the degradation in isolation caused by the material and thickness of the agglutinate substance can be overcome with optimization in this design.

5.5 Conclusions

In this study, a left-hand circular-polarization-selective surface with simple concept is simulated and fabricated. The measured data of the finished LHCPSS and

the simulated results show good consistency, having isolation of larger than 13 dB for an incident LHCP wave at 30 GHz, with transmission loss of –2.28 dB for the RHCP wave.

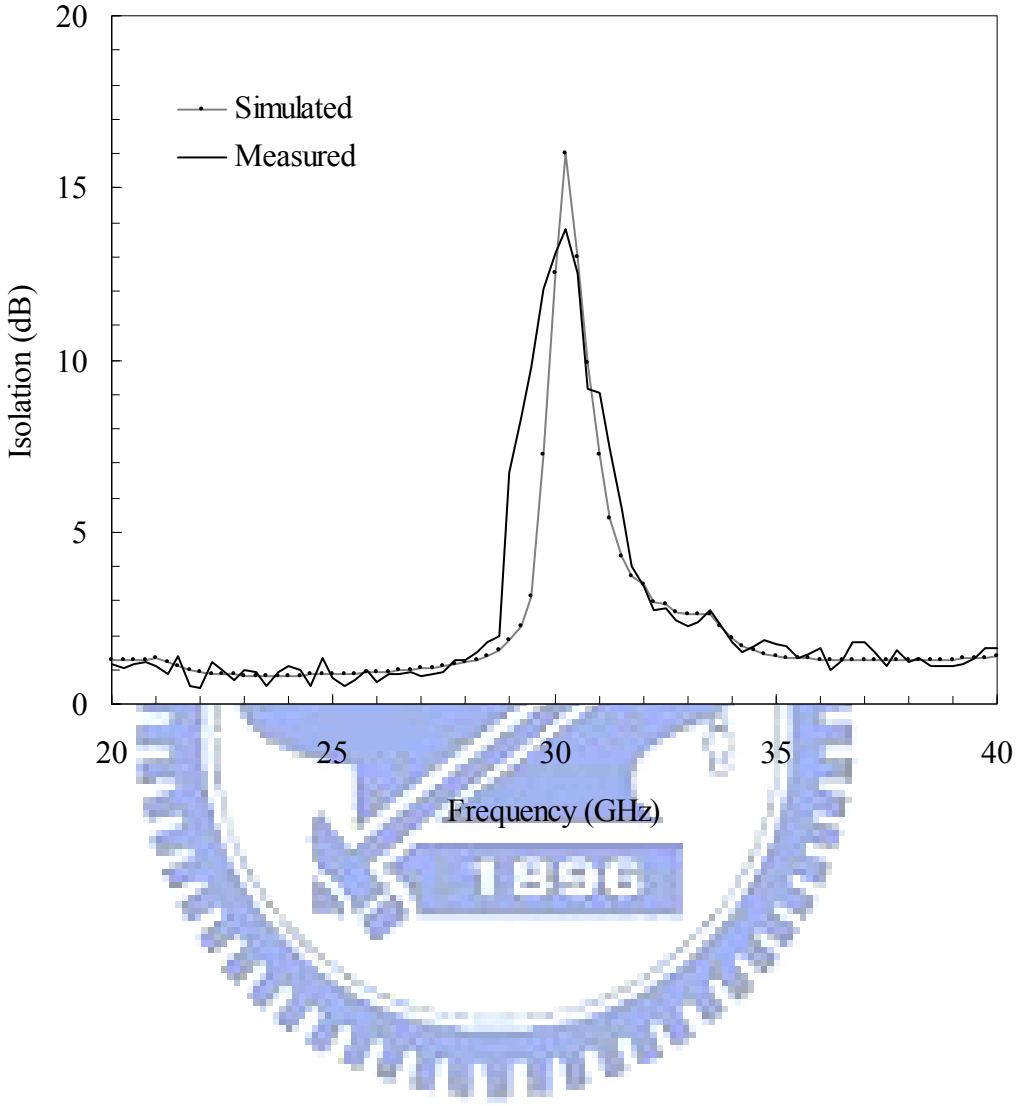

Figure 5.16 The simulated and measured isolations for the LHCPSS of p = 6.25 *mm*, *l*= 3.385 *mm*, l_1= 2.9 *mm*, l_2 = 3.0 *mm* and l_3= 2.6 *mm*.

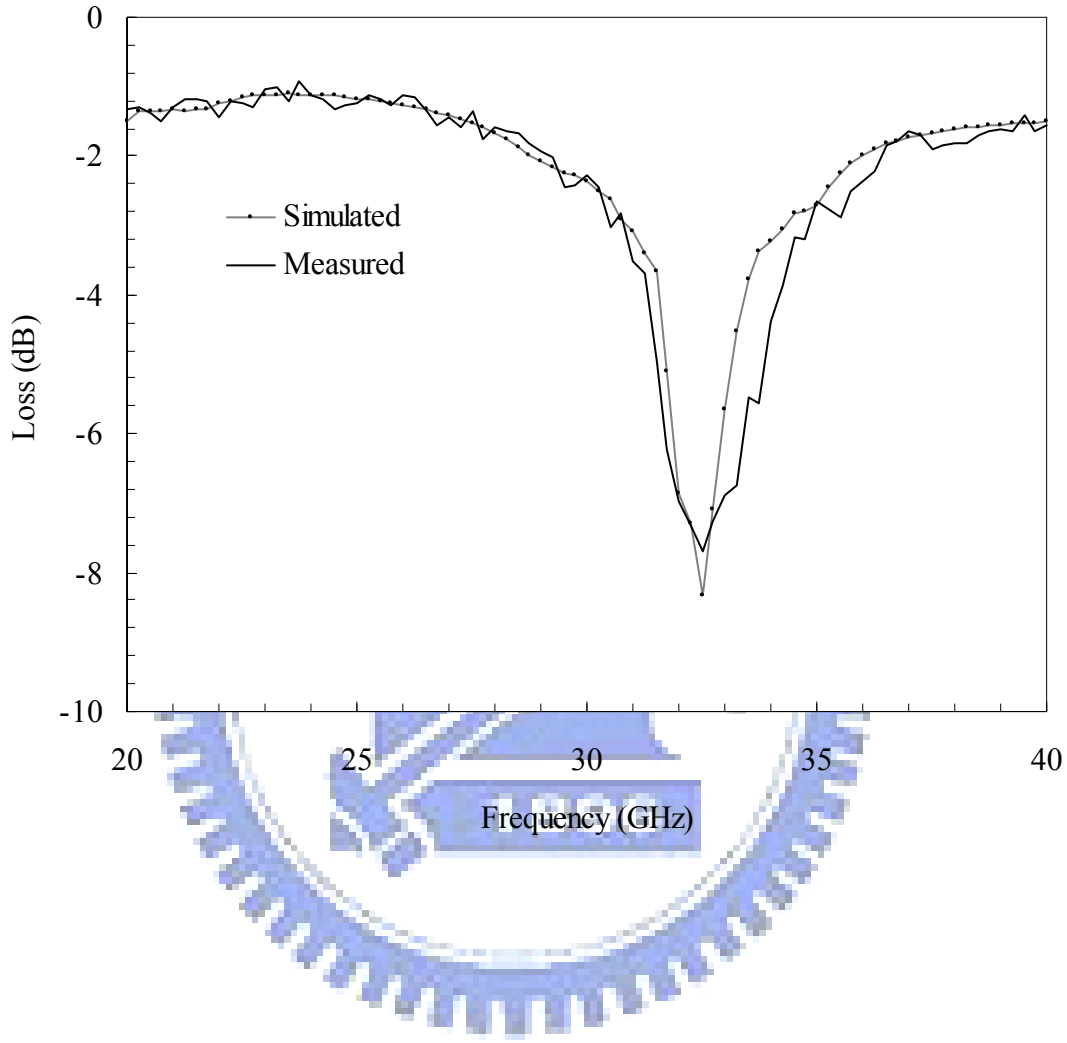

Figure 5.17 The simulated and measured transmission losses for the LHCPSS of p = 6.25 *mm*, *l*= 3.385 *mm*, l_1= 2.9 *mm*, l_2 = 3.0 *mm* and l_3= 2.6 *mm*.

The LHCPSS presented is a thoroughly stratified configuration with transverse planar elements implemented on different layers. The L-shaped traces accomplish the function that formerly had to be performed by vertical conductive segments. Avoiding the uses of vertical conductive segments makes this design well suited for PCB manufacturing process. By dint of the L-shaped traces, the frequency responses of blocking effect for different CP illuminations are diverse. At 30 GHz, LHCP incidence is blocked because of strong geometry resonance on dipoles, whereas RHCP incidence passes because of little or weak geometry resonance. Thus the CPSS is selective to the sense of CP waves.

More noteworthy, is that this new concept provides more flexibility in developing CPSSs. This CPSS design is more tolerable to the thickness and the material of the substrate. The height of the whole configuration is no longer strictly required to be a quarter wavelength, because the connection between each pair of dipoles in a unit cell, no longer relies on the vertical conductive segment, but the couplings caused by the L-shaped traces between dipoles. Laminates with various substrates and different thicknesses rather than one-quarter wavelength can be used to realize a CPSS with satisfactory performance by the method presented in this work. The completion of this work demonstrates the feasibility of this new type of CPSSs. Structures with superior performance may be created from the basis of this study.

Successful development of such surfaces will have several applications. For example, a good CPSS can be used as the sub-reflector of a Cassegrain antenna. The manufacturing of a planar CPSS is much easier than a curved sub-reflector. In addition, this type of Cassegrain antenna will have a minimal aperture blockage, because the CP waves reflected by the main reflector would pass through the CPSS almost without loss.

As a second example, the linear polarizer in the original LP folded reflectarray antenna would be replaced by a CPSS. The main reflector design would no longer be applicable, as it would be a simple flat conducting plate in this CP version. With the emergency of excellent CPSSs, folded reflectarray could be extended to circular polarization applications.

References

1. D. G. Berry, R. G. Malech, and W. A. Kennedy, “The reflectarray antenna,” *IEEE Trans. Antennas Propagat.*, vol. 11, pp. 645 - 651, Nov. 1963.

2. D. Pilz, and W. Menzel, “Folded reflectarray antenna,” *Electronics Lett..*, vol. 34, pp. 832 - 833, Apr. 1998.

3. J. Huang, and R. J. Pogorzelski, “Microstrip reflectarray with elements having variable rotation angles,” *IEEE AP-S Int. Symp.Digest*, vol. 2, pp. 1280 - 1283, July 1997.

4. C-P Chiu; and S-J Chung, “A new millimeter-wave folded microstrip reflectarray antenna with beam steering,” *IEEE AP-S Int. Symp.Digest*, vol. 3, pp. 140 - 143, June 2002.

5. D. Pilz and, W. Menzel, “A novel linear-circular polarization converter,” in *28th Europ. Microw. Conf.*, Amsterdam, 1998, pp. 18–23.

6. W. V. Tilson, T. Tralman, and S. M. Khanna, “A polarization selective surface for circular polarization,” *IEEE AP-S Int. Symp.Digest*, vol. 2, pp. 762 - 765, June 1988.

7. G. A. Morin, “A simple circular polarization selective surface,” *IEEE AP-S Int. Symp.Digest*, vol. 1, pp. 100 - 103, May 1990.

8. http://www.ansoft.com/products/hf/hfss/

6 A Novel Pattern Diversity Reflector Antenna Using Reconfigurable Frequency Selective Surfaces

6.1 Introduction

Wireless communications have attracted increasing attention in the recent years. Among the various wireless communication standards, IEEE 802.11 a/b/g, which operate in unlicensed spectrums, are the most widely used. Their frequency bands are not licensed by the FCC or other organizations exclusively for 802.11 traffic. Instead, the spectrum is shared with many other types of devices, such as cordless phones and Bluetooth devices. Many solutions in the relative fields were actively proposed and are still under development. For utilizing the limited spectrum efficiently, the technology of radiation pattern reconfigurable antennas [1]-[10] is often applied. The radiation pattern diversity operation offers optimized coverage by producing stronger gains in specific directions to increase the power intensity of the signal and an omni-directional pattern when communication in all directions is required. This type of antennas is an excellent candidate to reduce the multi-path interference and to enhance the communication link performance because of the adaptive patterns it provides.

Many pattern reconfigurable antennas stem from Yagi-Uda antenna design [4]-[10]. In [4], the conventional dipoles are replaced by monopoles. Whereas in [5]-[7], the antennas maintain the basic Yagi-Uda antennas but the parasitic monopole elements around the active monopole antennas are loaded alternatively, either short or open. Since the loads attached to the parasitic monopoles alter the

effective lengths of monopoles, the electromagnetic interactions between monopoles result in beam-formed patterns. Cylindrical rod monopoles are used in [5] and [7], while cylindrical rod monopoles with disc plates which help reducing the height of antenna are disclosed in [6]. Pattern reconfigurable antennas by using switched printed parasitic elements were also reported. Printed strips on the substrate [8]-[10] are adopted for use as the active and parasitic monopoles instead of the cylindrical rod monopoles to reduce the complexity substantially. The printed parasitic monopoles are length-tunable by directly changing the length of short-ended parasitic monopoles with switches [10]. In a Yagi-Uda antenna, if the length of the parasitic element is shorter than that of the active element, it will have a pulling pattern. Oppositely, if the length of the parasitic element is longer than that of the active element, it will have a pushing pattern. Therefore, different combinations of switching states form multiple radiation patterns; the directivity and orientation of the radiation pattern is under control. This provides a simple and flexible way for pattern beam-forming.

In this chapter, a new pattern reconfigurable antenna based on a different principle is proposed. This antenna, which evolved from the corner reflector antenna, has four rectangular plates standing erect on the ground plane and enclosing the substrate backed strip monopole in the center. Each rectangular plate is a Frequency Selective Surface (FSS) with two loop elements, whose transmission/reflection characteristic is designed to be controlled by one switching device. That is, only four switches are enough for configuring the reflection states of the four side walls of the proposed 90^{o} corner reflector antenna, so as to adaptively form the radiation patterns. The switching circuitry, bias lines, and impedance matching networks of this antenna are hidden beneath the ground plane,

which can avoid the undesired electromagnetic interactions. In addition, this antenna features beam tilting property, which can reduce the co-channel interference. Thus it is highly suitable for modern base station antenna applications.

The proposed antenna innovatively combines an inventive reconfigurable FSS design concept and the idea of realizing the pattern diversity function by corner reflector antenna. Moreover, these two individual methodologies developed can be extended for future reconfigurable electromagnetic structure designs and radiation pattern reconfigurable antennas respectively, so they are worth paying more attention to and making further investigations.

6.2 Design

The pattern reconfigurable reflector antenna, as shown in Figure 6.1, comprises a feeding monopole antenna in the center, four rectangular plates on the sidewalls of the square corner reflector antenna, and a finite square ground plane on which the former elements are mounted. Planar reconfigurable FSS is applied to implement the rectangular plates on the sidewalls. The transmission and reflection property of the FSS can be controlled by changing the switch state. For one state the FSS plate acts as a reflector, while for the other state it is transparent to the waves from/to the feed antenna. Four switches (A, B, C and D) connecting the FSS elements and the ground plane are located on the four sides respectively. The pattern of a corner reflector antenna varies with the number and the arrangement of the reflectors. With various combinations of the switch states, multiple patterns can thus be formed. The ground plane was made on the top surface of an FR4 substrate. The matching circuit was printed on the other side of the substrate, and prior to that, the impedance of the fabricated antenna had been measured. In the proposed antenna configuration, the

switches and their associated circuitry, e.g. the bias lines, are designed to be placed behind the ground plane but not within the region where electromagnetic waves propagate. This arrangement minimizes the adverse influence caused by the undesired yet necessary presence of those elements.

6.2.1 Feed Antenna

The center frequency of the pattern diversity reflector antenna is designed at 2.45 GHz. A quarter-wavelength monopole serves as the driving element, which is a 29.8 *mm* × 2.4 *mm* metal strip printed on a 1.6-*mm* thick, 4-*mm* wide and 30.5-*mm* long FR4 substrate with dielectric constant of 4.4. The ground plane is printed on top of another FR4 substrate that measures 140 *mm* × 140 *mm* and is perpendicular to the monopole. It is also the reference ground for the impedance matching microstrip line on the backside of the same substrate.

6.2.2 Conner Reflector

A conventional corner reflector is a directional antenna consists of two intersecting flat plates, which reflects electromagnetic waves back towards the source. The pattern shape, gain and feed point impedance are all functions of the feed-to-corner spacing and corner angle. As a rule of thumb, a good directivity for a right-angular corner reflector can be obtained if the spacing is between 0.25 and 0.75 wavelengths when the conducting plates are of infinite extent. The finite extent of the plates will result in a pattern broader than that for infinite plates. In practice, the height of the plate is usually chosen to be from 1.2 to 1.5 times the length of the feed so as to minimize the direct radiation by the monopole feed into the back region [12]-[14].

In order to obtain multiple symmetric patterns, reconfigurable FSSs with

identical dimensions are used construct the reflector plates in this work. Initially, the vertical reflector surfaces and the horizontal ground plane were assumed to be perfectly conductive. The vertical feed monopole was in the center of the reflectors. Corner reflector antennas with the reflector surfaces forming an equilateral triangle, a square, a pentagon, a hexagon and an octagon in various sizes were analyzed. Among these, the square one was selected because it has the best directivity with any two adjacent reflector surfaces being perfect conductors and the other two surfaces being void. The reflector plates were then determined to be 120 *mm* wide and 40 *mm* long. In this configuration, the maximum gain is 7.30 dBi. Enlarging the heights and widths of the reflector plates will improve the directivity but at the cost of the increased antenna volume.

6.2.3 Novel Reconfigurable FSS Design

A frequency selective surface is usually an assembly of identical elements periodically arranged in a one or two dimensional array that can provide frequency filtering to incoming electromagnetic waves. Similar to the frequency filters in traditional RF circuits, the FSS may have band-pass or band-stop spectral behavior. The frequency response of the reflection (or transmission) coefficient for a FSS depends on the geometry of its constituent elements and the arrangement of the array.

Researches on both the underlying theories and practices of many FSS element geometries have been well established [15]-[17]. Square loop FSS element is the one having simple and effective structure. It has a relatively wide frequency bandwidth, and its resonant frequency is fairly stable with respect to changes in incident angle and polarization. Besides, the reflection phase curves of the square loop structures are less sensitive to oblique incidence [18]-[20].

In virtue of its symmetric geometry, the FSS with square loop elements works

well for circular polarization waves. Nonetheless, the feed monopole is a linear polarization antenna. That means the width and length of the loop have not to be the same; there are more degrees of freedom in design to fit the FSS structures into the reflector plates of the corner reflector antenna at the same time maintain good performance. Therefore this type of element, more exactly the rectangular loop, was adopted for this work.

As shown in Figure 6.1, two shunt rectangular loop FSS elements are printed on a 120 *mm* × 40 *mm* FR4 substrate with thickness of 0.8 *mm*. A printed metallic line with a total length of about a half wavelength is created to connect these two rectangular loops. The FSS elements are designed such that whose current distributions change significantly with the switching state and hence there would be a conspicuously difference in the frequency response.

When the incident waves impinge on them, two equal amplitude and in-phase voltages are produced at the two ends of the metallic line. By symmetry, the line appears open circuited at its midpoint. This open circuit then causes short circuits at the two ends of the line when transformed back through the quarter-wavelength line segment. The rectangular loops are thus out of resonance because the induced current distributions are altered by the connection of the line and the rectangular loops, so that the input waves will pass through the surface almost uninhibitedly. On the other hand, if the midpoint of the metallic line is shorted to the ground, both ends of the metallic line appear to be open circuited due to quarter-wavelength transformations, i.e., the presence of the metallic line does not disturb the geometrical resonances of the rectangular loops, and the incident waves will be reflected back.

The equivalent circuit models of the reconfigurable FSS for both on- and off-states are illustrated in Figure 6.2. The rectangular loop element having a

band-pass characteristic acts as a series LCR circuit. The corresponding equivalent inductor, capacitor and resistor represented by L_{FSS}, C_{FSS} and R_{FSS} respectively show negligibly low series impedance at resonance. Terminating the middle of the metallic line to ground makes both ends of the line open, as shown in Figure 6.2(a). Therefore, a source at the resonant frequency of the FSS element drives currents across the series L_{FSS}, C_{FSS} and R_{FSS} circuit to the ground but not the output port. On the contrary, if the middle of the metallic line is left open, both ends of the line appear short circuited, as shown in Figure 6.2(b). The change in current distribution on the rectangular loop leads to another equivalent series circuit composed of L'_{FSS}, C'_{FSS} and R'_{FSS} that exhibits high impedance at the prescribed frequency. The source in this situation will not drive a current and will reach the output port.

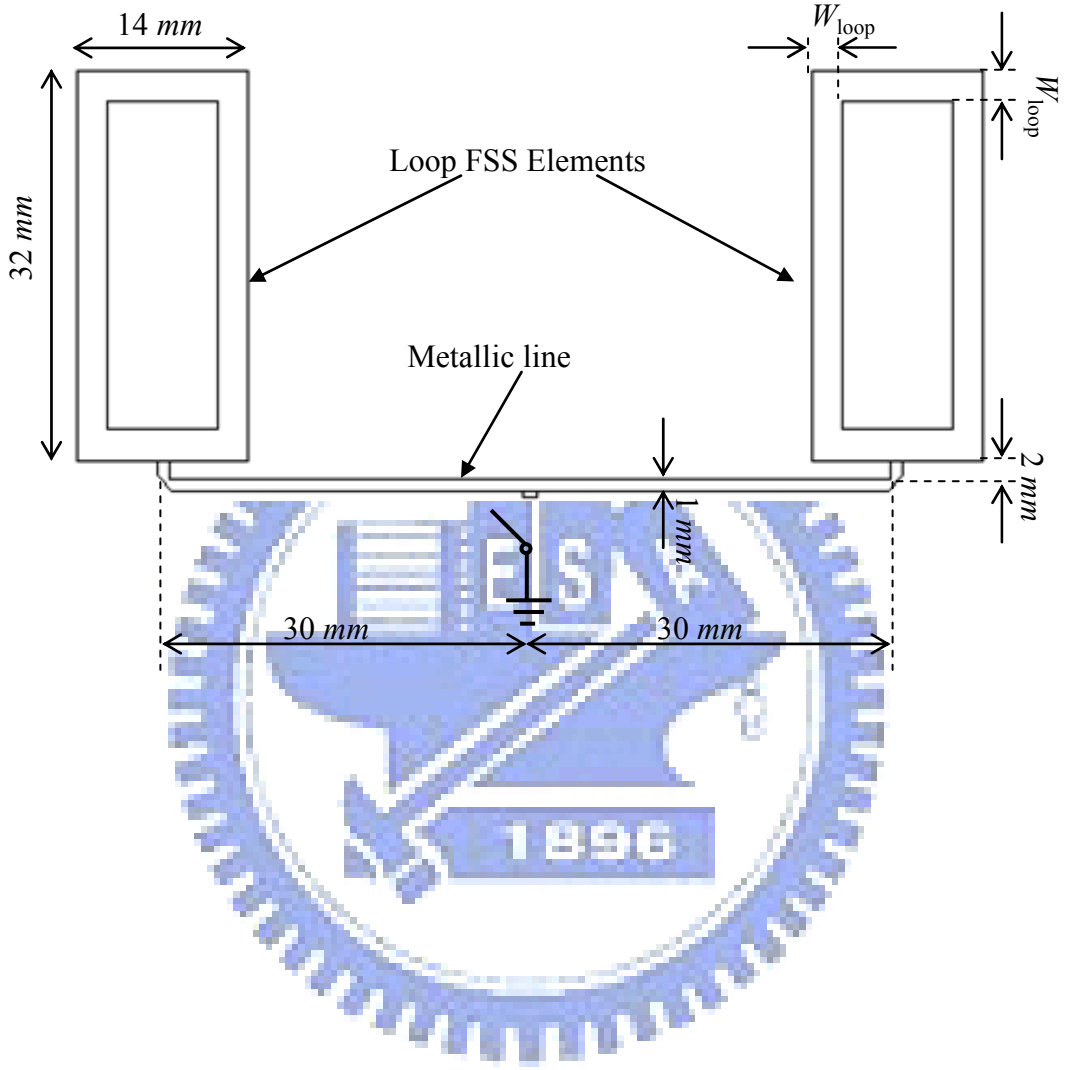

Figure 6.1 The geometry and parameters of the reconfigurable FSS.

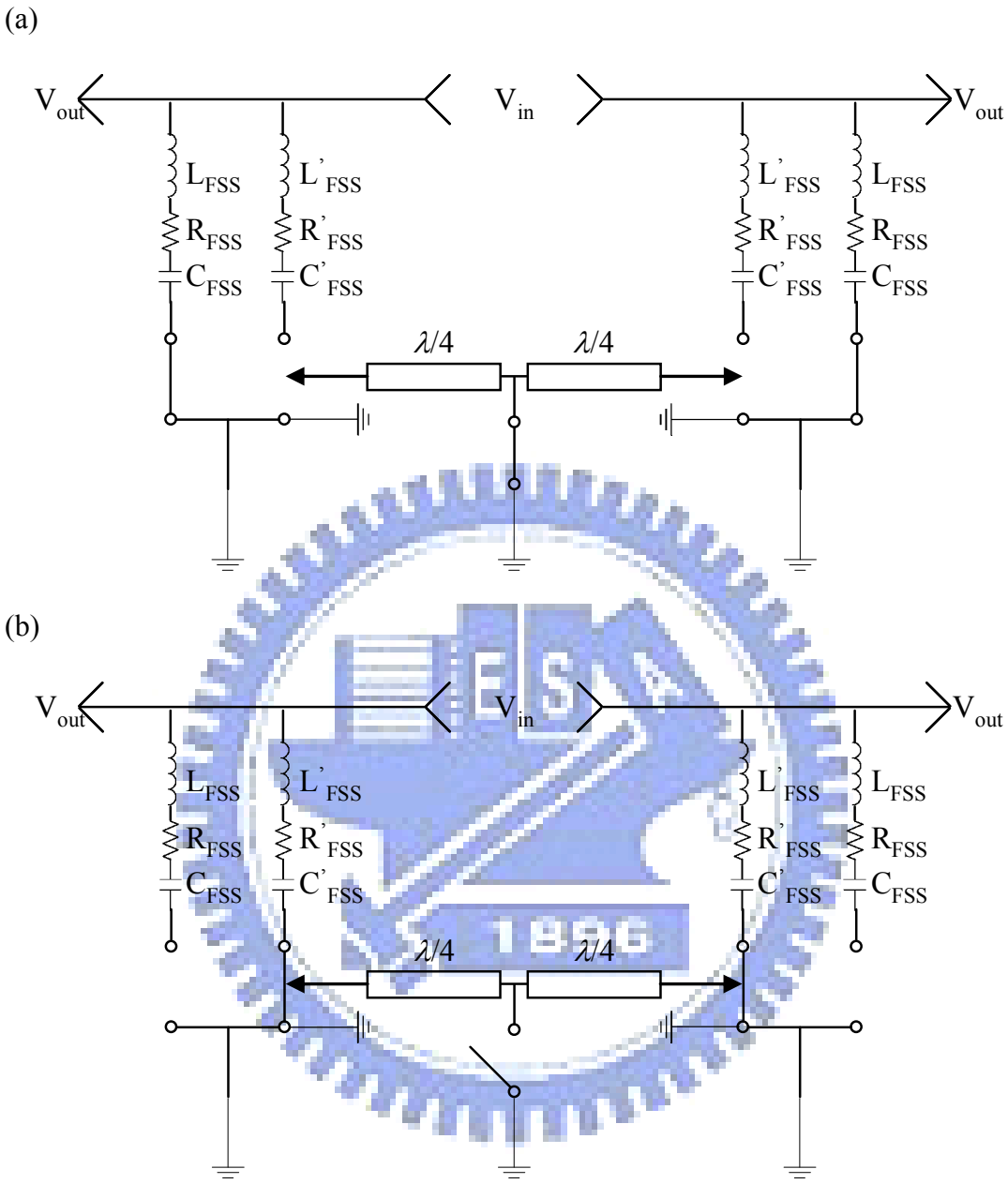

Figure 6.2 The equivalent circuit models of the reconfigurable FSS for (a) on-, and (b) off-state respectively.

The commercial software Ansoft HFSS [11] was employed to simulate the FSS structure. The FSS rectangular loop element is designed to resonate at 2.45 GHz for vertically polarized plane waves, with the lengths of the outer edges of the rectangular loop to be 14 *mm* and 32 *mm* respectively. The total length of the printed metallic line is 64 *mm*, and the width of the line which yields no significant effect on the electrical length is 1 *mm*. The gap between the metallic line and the ground plane is 0.5 *mm*. However, the width of the loop (W_{loop}) is an important parameter. A greater W_{loop} results in a wider transmission bandwidth and tends to resonate at higher frequency for the on-state, while the reflection curves scarcely vary with W_{loop} for the off-state, as shown in Figure 6.3. W_{loop} is determined to be 2.5 *mm* such that this design is opaque (transmission coefficient= –16.4 dB) in the on-state and transparent (reflection coefficient= –23.9 dB) in the off-state at 2.45 GHz.

Ideally, the proposed method can be extended to simultaneously control the switching states of a group of microwave elements with one switch, especially for periodic structures like FSSs, by properly arranging the positions of the elements and the electrical lengths of the transmission lines between them. Figure 6.4 diagrams an example that can switch all the FSS elements to the same state synchronously.

(a)

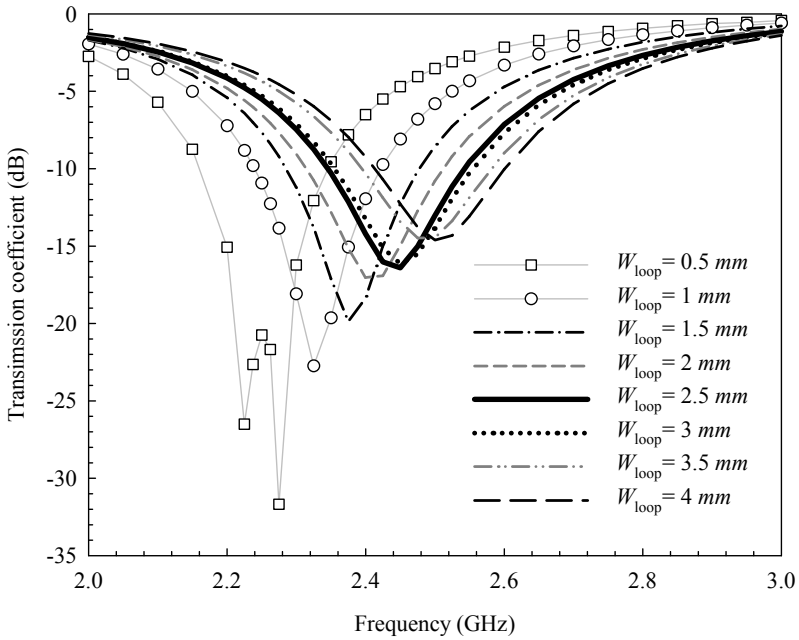

(b)

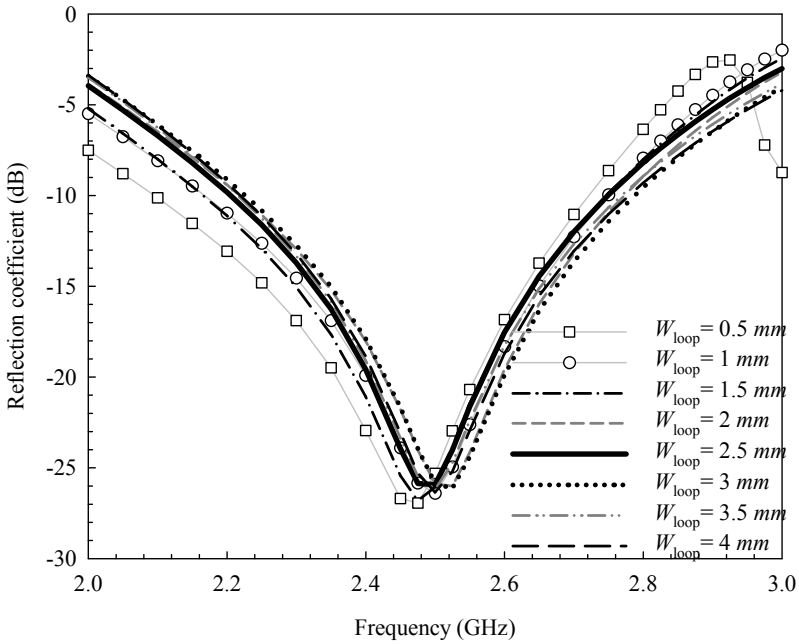

Figure 6.3 (a) The transmission coefficient curves for various widths of the loop in the on-state. (b) The reflection coefficient curves for various widths of the loop in the off-state.

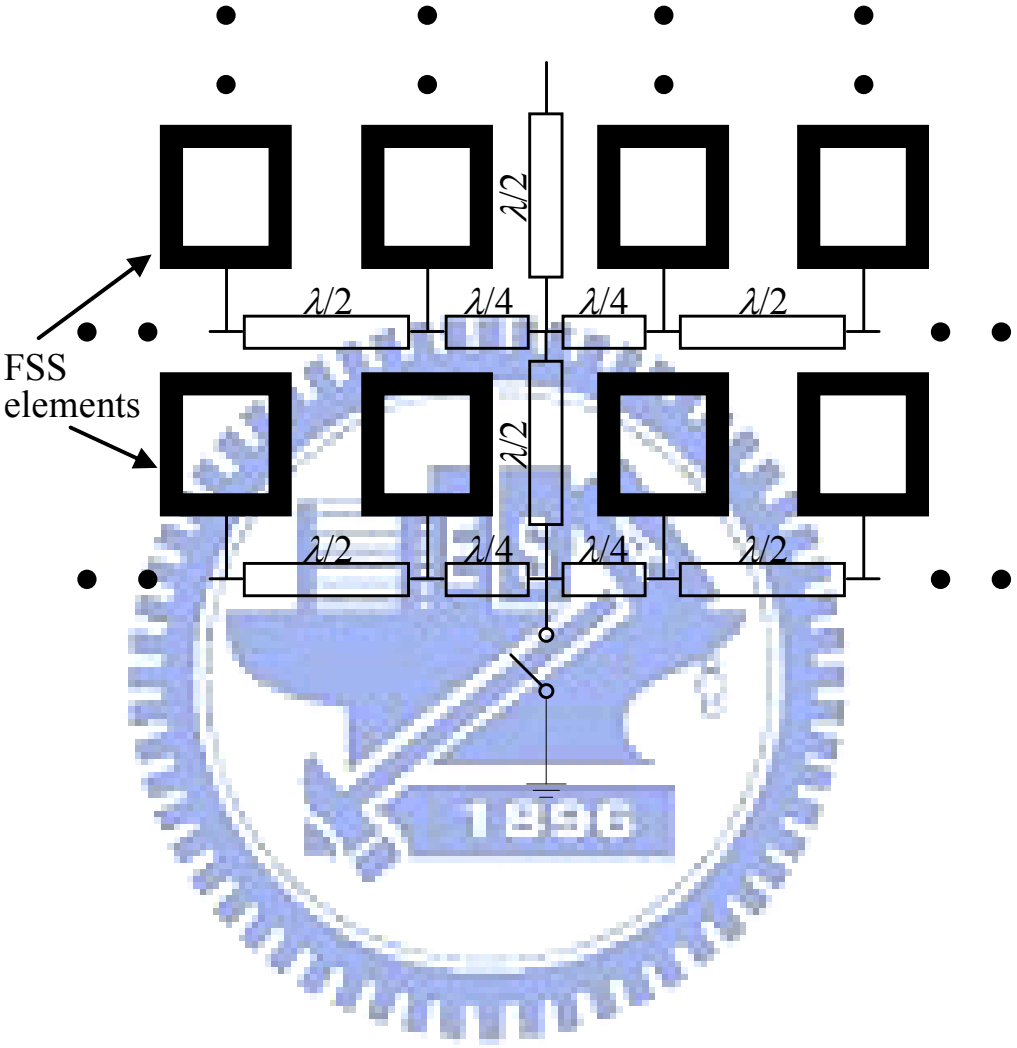

Figure 6.4 An illustrative method of configuring a group of periodically distributed microwave elements to the same state synchronously.

6.3 Results

The photograph of the finished antenna is shown in Figure 6.5. Patterns with different shapes and orientations can be achieved by various combinations of the switch states. Due to the symmetry of the antenna architecture, there are six fundamental cases. The definitions and their corresponding antenna parameters are listed in TABLE II, where 0 stands for switch off and 1 for switch on. The on and off states are realized by directly soldering the middle point of the metallic line to the ground plane and de-soldering respectively. Since Case 3 provides the maximum peak gain, the impedance of Case 3 was measured, and then the matching circuit was designed and implemented. Figure 6.6 shows the measured return losses for the six cases against frequency. It can be seen that the –10 dB bandwidth for Case 3 is from 2.09 GHz to 2.57 GHz (about 19.6%). The narrowest bandwidth occurs for Case 1, which is 0.2 GHz. The bandwidths of the other cases cover at least 2.19-2.50 GHz.

Figure 6.7 to Figure 6.12 display the measured co-polarization patterns for different cases at the 2.45 GHz. Obviously, the patterns are apt to be directional with their main lobes pointed toward the orientation where the switch states are off. When the switches are all on or all off, the pattern is basically omni-directional. The pattern of Case 4 is bidirectional because two of the switches on the opposite sides are in the same state and vice versa. Case 2, 3 and 5 have directional patterns while Case 3 produces the maximum gain, as can be expected from the simulations. For Case 3, the measured patterns agree well with the simulated ones in the main beam region, whereas with dissimilar side-lobes. The peak gain of 5.99 dBi was measured at (θ=45^o, ϕ= 225^o). The measured side-lobe level and half power beam width in ϕ= 225^o plane are 12.17 dB and 52^o respectively.

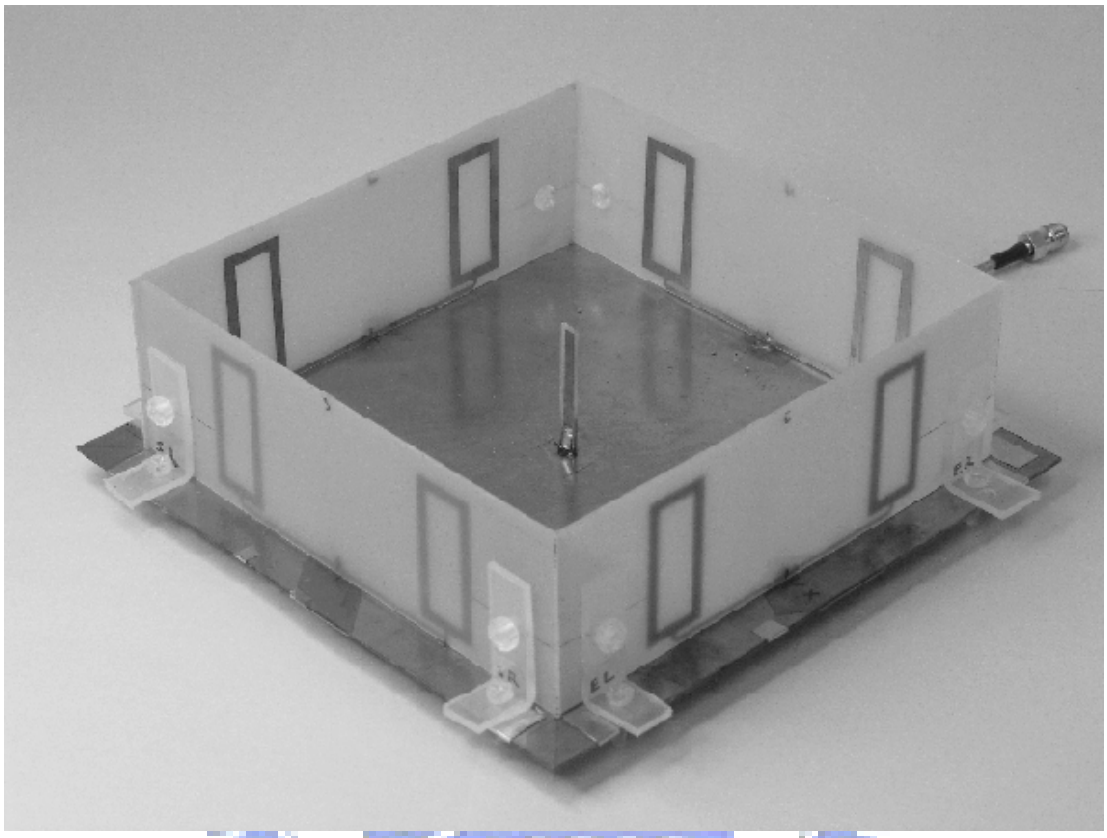

Figure 6.5 The photograph of the finished pattern reconfigurable reflector antenna.

TABLE II The definitions of the six fundamental cases and their corresponding parameters of the pattern reconfigurable reflector antenna.

		Case 1	Case 2	Case 3	Case 4	Case 5	Case 6
Switch states	A	0	0	1	0	1	1
	B	0	1	1	1	1	1
	C	0	0	0	0	0	1
	D	0	0	0	1	1	1
Simulated peak gain direction		Omni	θ= 39°, ϕ= 270°	θ= 39°, ϕ= 225°	θ= 39°, ϕ= 0°	θ= 36°, ϕ= 180°	Omni
Simulated peak gain (dBi)		2.71	5.24	6.77	4.66	6.19	3.26
Measured peak gain (dBi)		1.42	3.05	5.99	3.21	3.80	1.47
Measured Bandwidth (GHz)		2.22~2.42	2.19~2.50	2.09~2.57	2.12~2.56	2.08~2.56	2.08~2.57

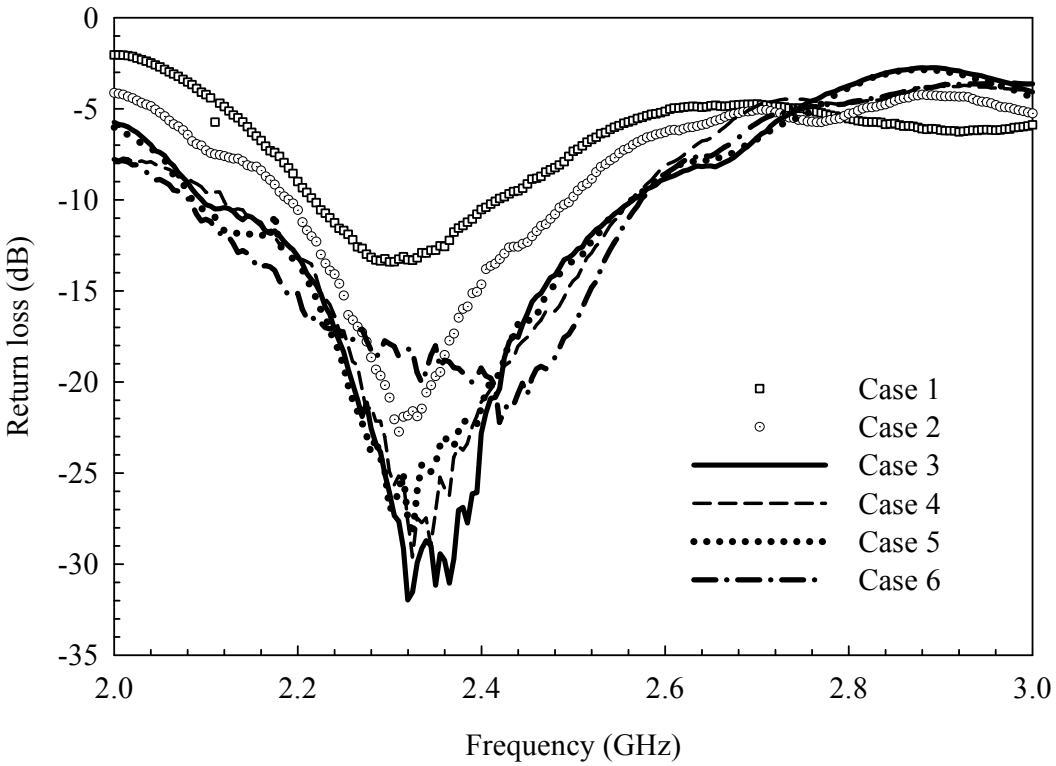

Figure 6.6 The measured input return losses for the six cases of the pattern reconfigurable reflector antenna as a function of frequency.

(a)

(b)

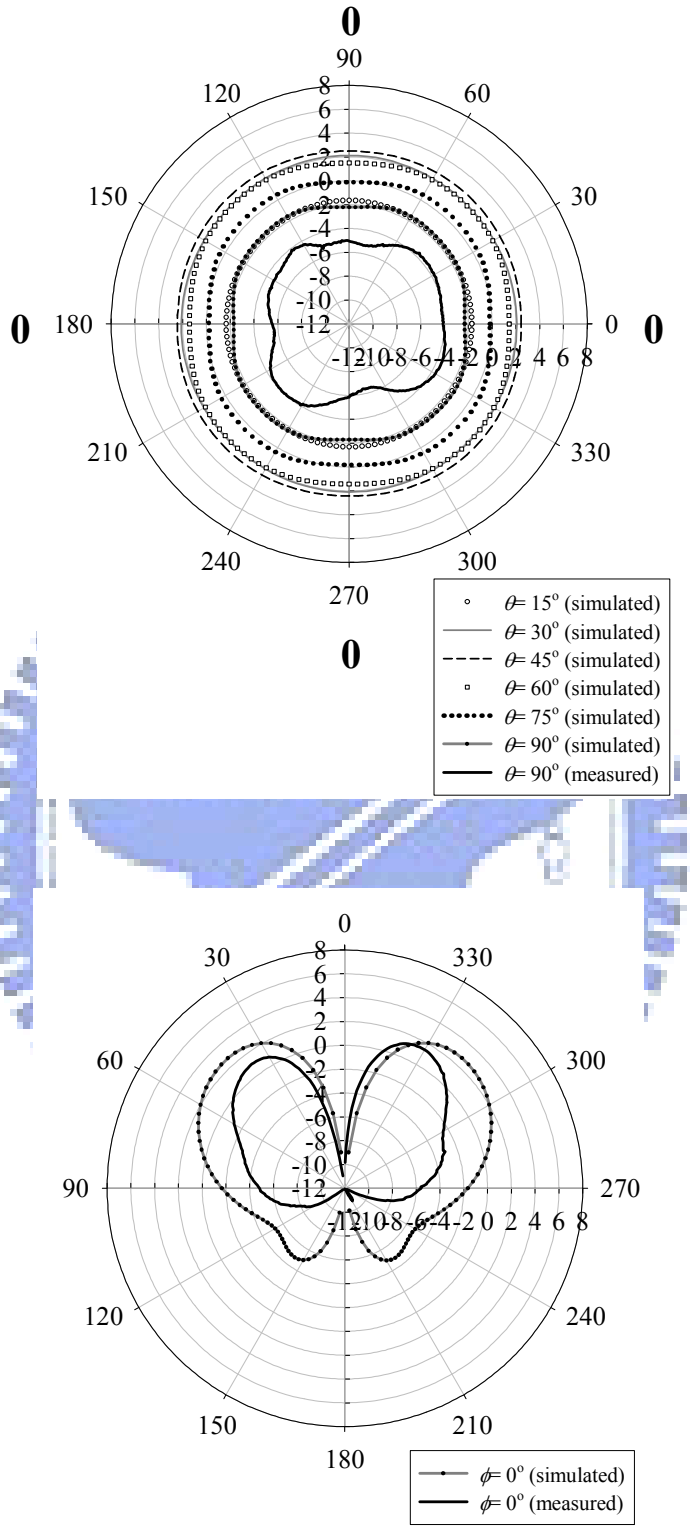

Figure 6.7 The simulated and measured patterns of Case 1 at 2.45 GHz (a) for various azimuth cuts, and (b) in $\phi = 0^{o}$ plane.

(a)

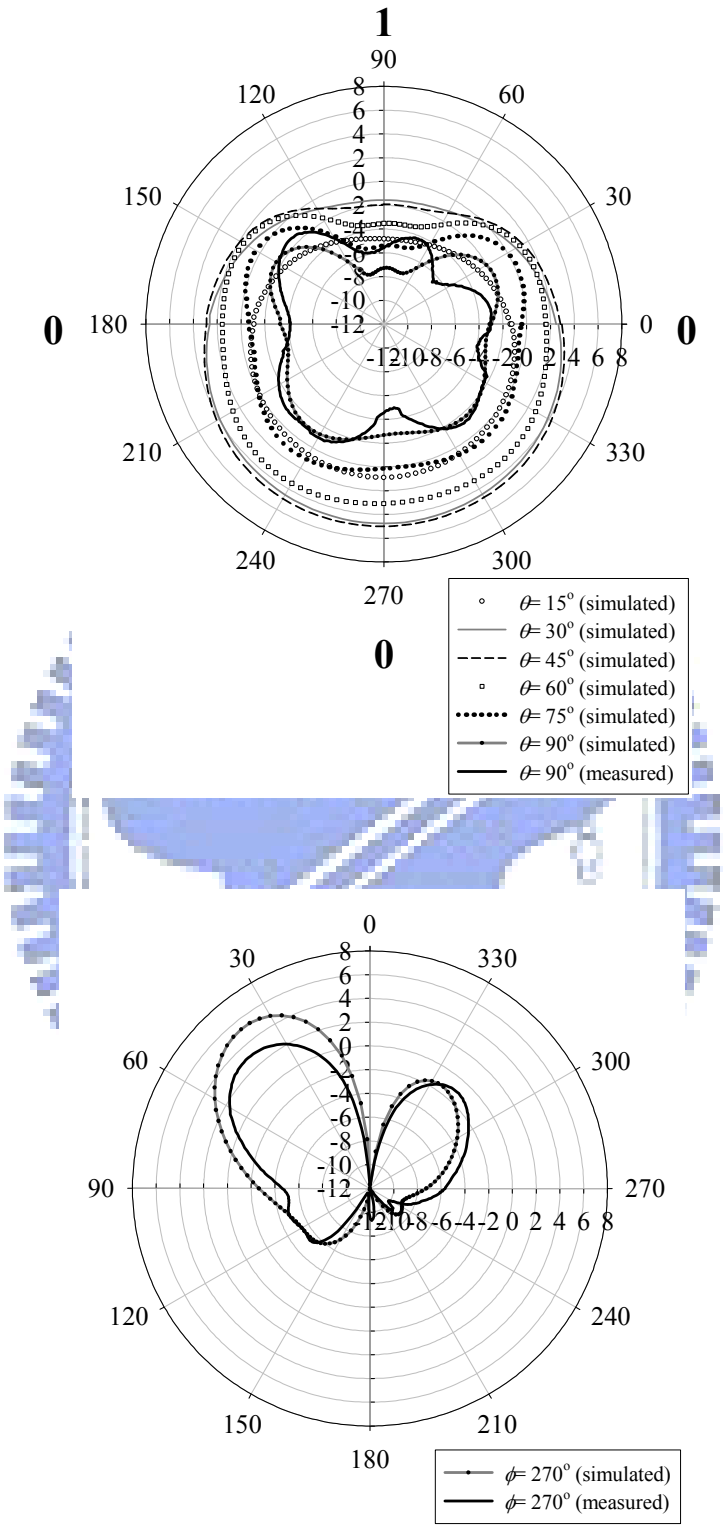

Figure 6.8 The simulated and measured patterns of Case 2 at 2.45 GHz (a) for various azimuth cuts, and (b) in $\phi = 270^{o}$ plane.

(a)

(b)

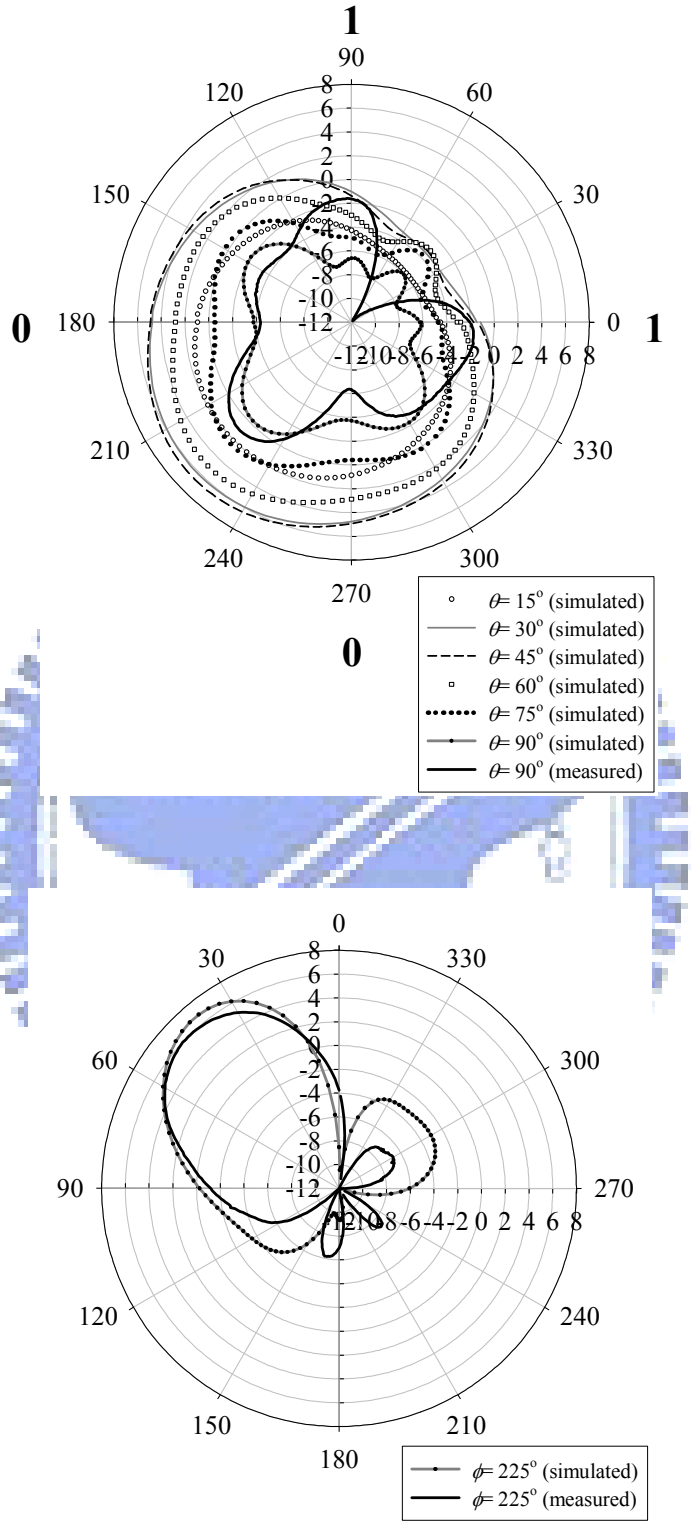

Figure 6.9 The simulated and measured patterns of Case 3 at 2.45 GHz (a) for various azimuth cuts, and (b) in $\phi = 225^{o}$ plane.

(a)

(b)

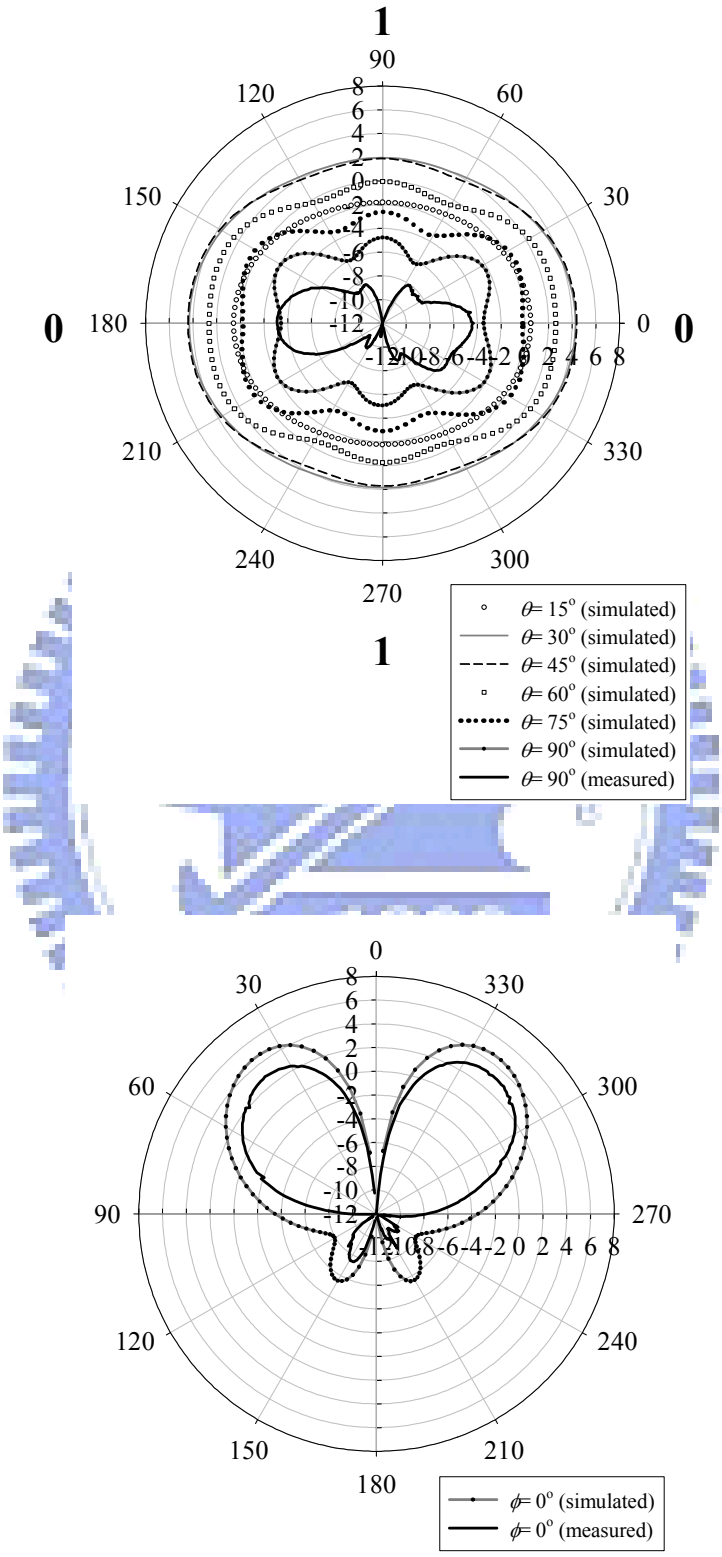

Figure 6.10 The simulated and measured patterns of Case 4 at 2.45 GHz (a) for various azimuth cuts, and (b) in $\phi = 0^{o}$ plane.

(a)

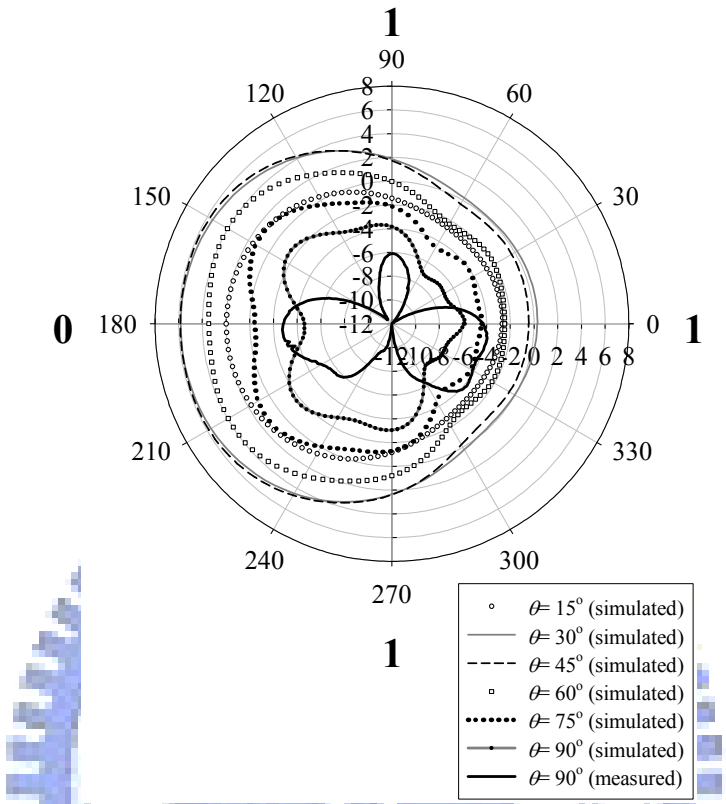

(b)

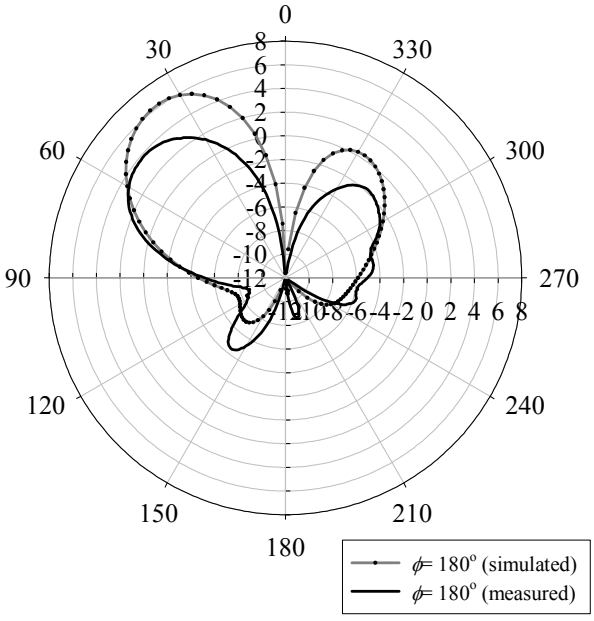

Figure 6.11 The simulated and measured patterns of Case 5 at 2.45 GHz (a) for various azimuth cuts, and (b) in ϕ= 180° plane.

(a)

(b)

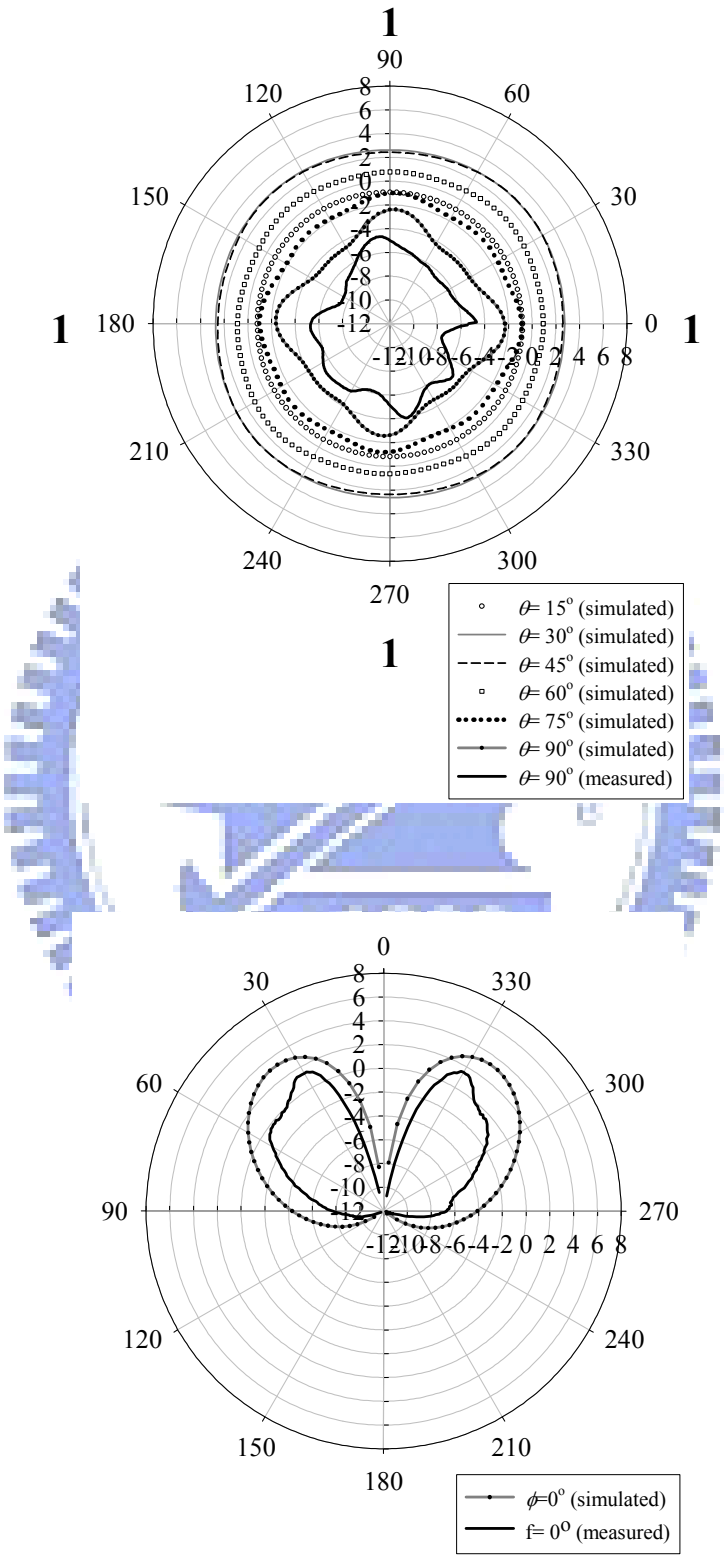

Figure 6.12 The simulated and measured patterns of Case 6 at 2.45 GHz (a) for various azimuth cuts, and (b) in $\phi = 0^{o}$ plane.

6.4 Conclusions

In this chapter, a radiation pattern reconfigurable antenna has been presented. It evolved from the corner reflector antenna. A novel concept has been proposed to control a FSS to be transmissive or reflective to waves at designated frequency with only one switching device. The reconfigurable FSS plates were used on the side walls of the corner reflector antenna. This antenna provides six fundamental patterns by various combinations of the switch states. The pattern can also be steered to rotate in azimuth plane electronically. By comparison, the maximum measured peak gain of the finished antenna is 5.99 dBi, and the maximum simulated peak gain of 6.77 dBi is close to the maximum achievable gain of 7.30 dBi that assumes the side walls of the corner reflector antenna to be perfect conductors instead of FSSs in the same configuration. This fact shows the reconfigurable FSS plates in this antenna are nearly perfectly conductive when acting as reflectors and almost transparent when in the other state. A better gain and improved back-lobes could be accomplished by increasing the dimensions of the reflectors.

The successful development of the antenna demonstrates the feasibility and performances of using the concept of corner reflector to realize the radiation pattern diversity. It is possible to extend this type of antenna to circular polarization version and for multi-band operation on the basis of investigations in this work.

References

1. A. Mehta and D. M. Syahkal, “Spiral antenna with adaptive radiation pattern under electronic control,” in *Proc. IEEE Int. Symp. Antennas Propagat.*, vol. 1, pp. 843–846, June 2004.

2. A. Mehta, H. Nakano and D. M. Syahkal, “A switched beam single arm rectangular spiral antenna with hybrid switch network,” in *Proc. IEEE Int. Symp. Antennas Propagat.*, vol. 2B, pp. 589–592, July 2005.

3. S. S. L. Yang and L. M. Luk, “A wideband l-probe fed patch antenna for pattern reconfigurable,” in *Proc. IEEE Int. Symp. Antennas Propagat.*, vol. 2B, pp. 581–584, July 2005.

4. M. D. Migliore, D. Pinchera, and F. Schettino, “A simple and robust adaptive parasitic antenna,” *IEEE Trans. Antennas Propagat.*, vol. 53, no. 10, pp. 3262–3272, Oct. 2005.

5. Y. Nakane, T. Noguchi, and Y. Kuwahara, “Trial casel of equipped with switched loads on parasitic elements,” *IEEE Trans. Antennas Propagat.*, vol. 53, no. 10, pp. 3398–3402, Oct. 2005.

6. M. R. Kamarudin and P. S. Hall, “Disc-loaded monopole antenna array for switched beam control,” *Electronics Lett.*, vol. 42, iss. 2, pp. 66–67, Jan. 2006.

7. R. Vaughan, “Switched parasitic elements for antenna diversity,” *IEEE Trans. Antennas Propagat.*, vol. 47, iss. 2, pp. 399–405, Feb. 1999.

8. H. S. M. Elkamchouchi and H. E. -D. M. Hafez, “Switchable beam diversity antenna,” in *Proc. 3rd Int. Conf. Microwave and Millimeter Wave Tech.*, pp. 377–380, Aug. 17–19, 2002.

9. C. Laohapensaeng, C. Free, and K. M. Lum, “Printed strip monopole antenna with the parasitic elements on the circular ground plane,” in *Proc. IEEE Int. Workshop in Antenna Tech.: Small Antennas and Novel Metamaterials*, pp. 371–374, March 7–9, 2005.

10. S. Zhang, G. H. Huff, J. Feng, and J. T. Bernhard, “A pattern reconfigurable microstrip parasitic array,” *IEEE Trans. Antennas Propagat.*, vol. 52, iss. 10, pp. 2773–2776, Oct. 2004.

11. http://www.ansoft.com/products/hf/hfss/

12. W. L. Stutzman, G. A. Thiele, *Antenna Theory and Design*. New York: Wiley & Sons Inc., 1997.

13. N. Inagaki, ”Three-dimensional corner reflector antenna,” *IEEE Trans. Antennas Propagat.*, vol. 22, iss. 4, pp. 580–582, July 1974.

14. N. Inagaki, K. Uchikawa, Y. Hashimoto, N. Kukuma, ”3-D corner reflector antenna and its analysis using UTD,” in *Proc. IEEE Int. Symp. Antennas Propagat.*, vol. 1, pp. 598–601, June 20–24, 1994.

15. B. A. Munk, *Frequency Selective Surfaces: Theory and Design*. New York: Wiley & Sons Inc., 2000.

16. G. H-H Sung, K. W. Sowerby, and A. G. Williamson, “Equivalent circuit modelling of a frequency selective plasterboard wall,” in *Proc. IEEE Int. Symp. Antennas Propagat.*, vol. 4A, pp. 400–403, July 2005.

17. D-G Youn, K-H Kim, Y-C Rhee, S-T Kim, and C-C Shin, “Experimental development of 2.45GHz rectenna using FSS and dual-polarization,” in *Proc. 30th European Microwave Conf.*, pp. 1–4, Oct. 2000.

18. A. Pirhadi, M. Hakkak, F. Keshmiri, and R. K. Baee, ” Design of compact dual

band high directive electromagnetic bandgap (EBG) resonator antenna using artificial magnetic conductor," *IEEE Trans. Antennas Propagat.*, vol. 55, no. 6, pp. 1682–1690, June 2007.

19. T. K. Wu, "Double-square-loop FSS for multiplexing four (S/X/Ku/Ka) bands," in *Proc. IEEE Int. Symp. Antennas Propagat.*, vol. 3, pp. 1885–1888, June 24–28, 1991.

20. Y-Y Gu, W-X Zhang, Z-C Ge, and Z-G Liu, "Research on reflection phase characterizations of artificial magnetic conductors," in *Proc. 2005. Asia-Pacific Microwave Conf.*, vol. 3, Dec. 4–7, 2005.

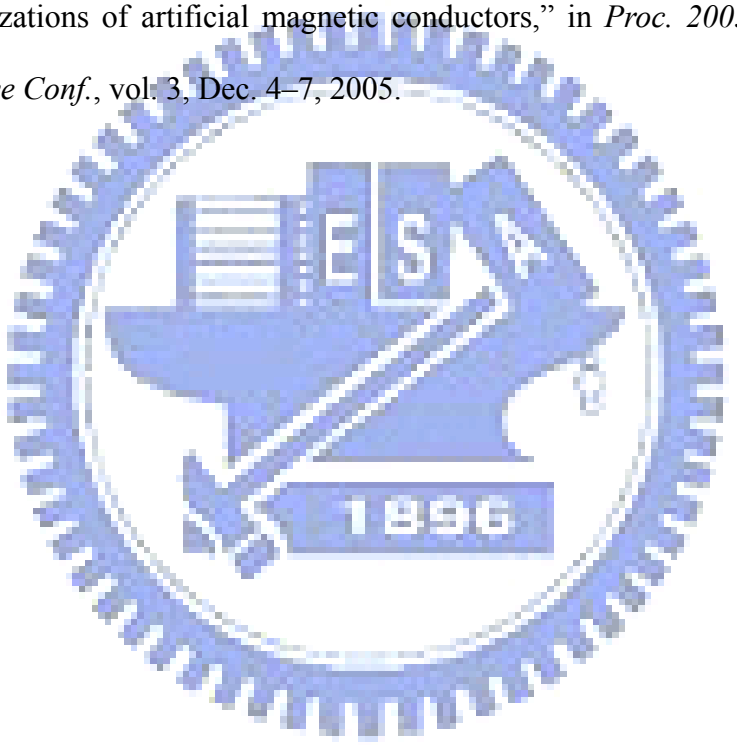

7 Conclusions and Future Works

In this dissertation, a 38 GHz waveguide-fed microstrip antenna array using a novel beam-steering technique was first proposed. The array is composed of 15 sub-arrays fed by a rectangular waveguide through apertures on the waveguide's top wall. Each sub-array contains two parallel series-fed microstrip antenna arrays. The array has a fixed beam in the E plane and a variable beam in the H plane. The phase difference between adjacent sub-arrays is controlled by changing the waveguide width so as to steering the array beam. The measured gain of the array is about 22 dBi. The main beam scanning angle is 5.4^{o}.

Next, a dual-mode folded microstrip reflectarray antenna was developed and demonstrated in this paper. The proposed folded reflectarray antenna contains three parts: a planar main reflector, a planar sub-reflector, and printed feed antennas. The main reflector is used to produce twisted re-radiated fields and to provide phase compensation for focusing. The sub-reflector parallel with the main reflector is made of a substrate printed with high-density metal grid lines, which is transparent to perpendicularly polarized fields, but would reflect the parallel ones. Three fixed-position patch antennas with polarization parallel to the grid lines are created for the radar mode, so that the radiation beam is switchable. Another patch with perpendicular polarization is designed for communication. A simple approach was proposed for simulating and designing the folded reflectarray. In the radar mode, the total beam switching angle is 29.5^{o}. At 38.5 GHz, the finished folded reflectarray antenna possesses an antenna gain of larger than 20 dBi within the beam switching range. A maximum gain of 27.4 dBi and the corresponding aperture efficiency of 33.9% were achieved. While in the communication mode, the ripple in the pattern

was improved by enclosing the feed patch with a square metal frame, the beamwidth is much broader, and thus provides communications over a wide angular range.

Then, a 60 GHz RHCPSS was investigated. The structure of the CPSS presented is very simple, so that printed circuit technology could be used to realize it. Method of moments was utilized to extract the currents on a single circular polarization selective structure. Using periodic Green's function together with the currents, a 2 dimensional infinite CPSS can be simulated. From which, scattered field for different circularly polarized incident waves were obtained. The optimal design parameters were found in this study. The respective simulated isolation and transmission loss at 60 GHz are 26.4 dB and -0.43 dB. While for the finished RHCPSS, the maximum measured isolation of 23.89 dB and the minimum measured transmission loss of -2.25 dB occur at 58.4 GHz,

Investigations into a new type of CPSSs were also carried out. It is of simple planar structure without any vertical conductive segments. Couplings, through the use of L-shaped traces, were produced to replace the vias. Operational principle and design procedure are developed, thus the optimal design parameters are found. The measured data of the finished LHCPSS have an isolation of larger than 13 dB for an incident LHCP wave at 30 GHz, with transmission loss of -2.28 dB for the RHCP wave. This example demonstrates the performances of the design and the attractiveness the new type of CPSSs.

Lastly, a corner reflector antenna with pattern diversity was developed. It supports multiple patterns with the maximum measured gain of 6.77 dBi. By controlling the switch states, the pattern can be steered in 45^{o} increment to cover the whole H plane. This design provides a simple and flexible way for pattern beam-forming.

The proposed CPSSs and FSS can be modified or integrated to contribute to more advanced planar reflector antennas, such as corner reflector antenna, reflectarray antenna, folded reflectarray and so on. For example, the method of simultaneously control the switching states of a group of microwave elements with one switch can be utilized to design a multi-band reconfigurable FSS. It is also feasible to be applied to handle the characteristics of a CPSS.

Besides, a good CPSS could raise many new applications, especially the reflectarray antenna. For a conventional folded microstrip reflectarray antenna, the main-reflector provides the 90^{o} polarization twisting of the re-radiation and phase compensation for the in-phase array. The sub-reflector parallel to the main-reflector is transparent to one linear polarization but would reflect the other one. The electromagnetic wave radiated from the feed antenna located at the center of the main reflector is linearly polarized. Hence the wave would be reflected when it confronts the sub-reflector. The main reflector then receives the field and re-transmits it. The re-transmitted field could penetrate the sub-reflector and focus in the far field region.

With the emergence of excellent CPSSs, the concept of the folded reflectarray antennas could be extended to circular polarization applications. Figure 7.1 illustrates the concept of the circular polarization folded reflectarray antenna. The linear polarizor in the original linear polarization folded reflectarray antenna is replaced by the CPSS. Nevertheless, the main reflector design is not applicable to the circular polarization case; we use just a simple flat conducting plate instead. Phase compensating is no longer carried out by tuning the elements on the main reflector of the linear polarization folded reflectarray antenna, but by adjusting adequate amounts of rotation on the elements of the CPSS around the z-axis. With reference to Figure 7.1(b), a simple trigonometric relation is used to compensate the

additional path lengths across the array's surface.

Assume a LHCP wave emitted from the feed on the conducting plate, it undergoes various path length to each element of the LHCPSS and makes different phase shifts among the elements. Take the distance from the feed to the centermost element as reference, element with lager path length should be rotated clockwise to offset the phase delay. Thus the elements of the LHCPSS re-radiate in-phase and the reflection wave resulted. When the reflected LHCP wave impinges the conducting plate and get reflected again, the sense of polarization changes. Then the consequent RHCP wave will pass through the LHCPSS with an enhanced gain in the boresight (+z) direction.

(a)

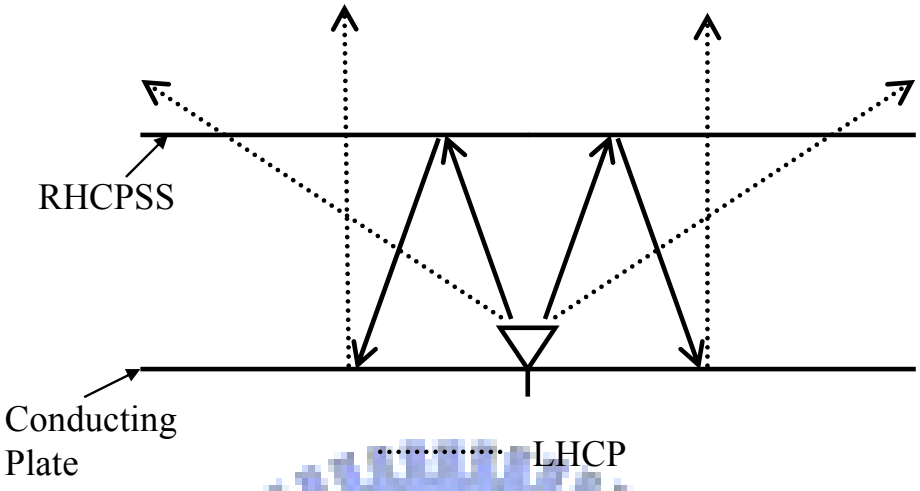

(b)

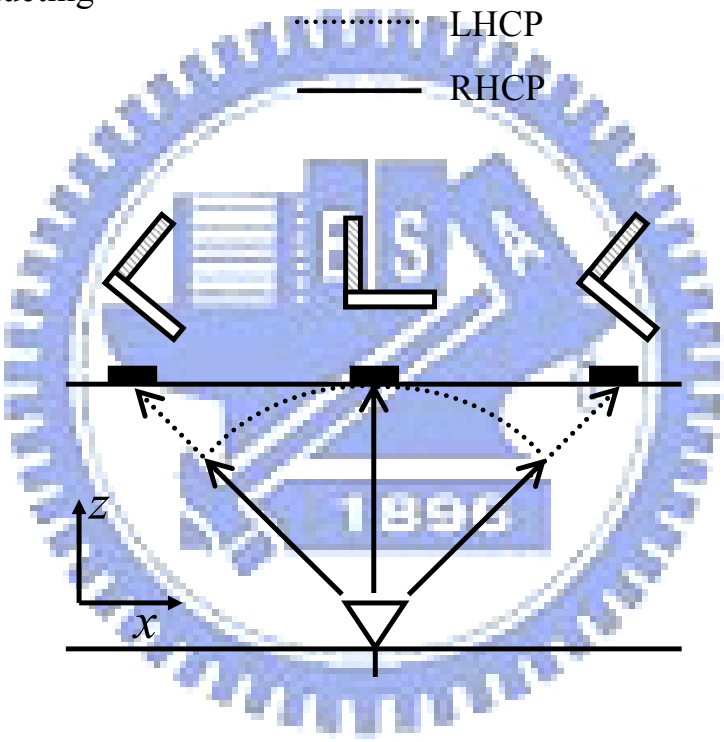

Figure 7.1 Schematic diagram of circular polarization folded reflectarray antenna. (a) Topology, (b) Phase compensation method.

Vita

I-Young Tarn was born in Taipei in 1970. He received the B.S. and M.S. degrees in electrical engineering from Yuan-Ze University, Tao-Yuan, Taiwan, R.O.C., in 1993 and 1995, respectively. From 1995 to 1999, he was an Assistant Researcher in Systems Engineering Project, National Space Program Office, Hsinchu, Taiwan, R.O.C.. Since 2000, he has been with the Electrical Engineering Division of the National Space Program Office, where he has been involved in satellite communications and antenna design. In the same year, he entered the Ph.D. program in Department of Communication Engineering at National Chiao Tung University, Hsinchu, Taiwan, R.O.C.. His research interests include microwave/mm-wave microstrip antennas, reflectarray antennas, frequency selective surfaces and circular polarization selective structures.

Publication List

Journal Papers

I-Young Tarn, and Shyh-Jong Chung, “A New Advance in Circular Polarization Selective Surface – A Three Layered CPSS without Vertical Conductive Segments,” *IEEE Trans. Antennas Propagat.*, vol. 55, no. 2, pp. 460 - 467, Feb. 2007.

Chong-Yu Hong, Ching-Wei Ling, I-Young Tarn, and Shyh-Jong Chung, “Design of a Planar Ultra-Wideband Antenna with a New Band-Notch Structure,” *IEEE Trans. Antennas Propagat.*, vol. 55, iss. 12, pp. 3391 - 3397, Dec. 2007.

I-Young Tarn, and Shyh-Jong Chung, “A Dual-Mode Millimeter-Wave Folded Microstrip Reflectarray Antenna,” *IEEE Trans. Antennas Propagat.*, vol. 56, iss. 6, pp. 1510 - 1517, Jun. 2008.

I-Young Tarn , and Shyh-Jong Chung, “A Novel Pattern Diversity Reflector Antenna Using Reconfigurable Frequency Selective Surfaces”, submitted to *IEEE Trans. Antennas Propagat.*, 2008

Conference Papers

I-Young Tarn, and Shyh-Jong Chung, "A Beam-steering Waveguide-fed Microstrip Antenna Array", *TSMMW2002*.

I-Young Tarn, and Shyh-Jong Chung, "A Dual-modes Folded Microstrip Reflectarray Antenna ", *PIERS2003*.

I-Young Tarn, and Shyh-Jong Chung, "A 60 GHz Circular Polarization Selective Surface by Printed Circuit Technology", *MINT-MIS2005*/*TSMMW2005*.